Spring 5-2018

FINITE ELEMENT MODELING AND UPDATING OF A FIVE-TIERED PAGODA STYLE TEMPLE

Linh Maytham Abdulrahman
University of Nebraska - Lincoln, linh.abdulrahman@huskers.unl.edu

Abdulrahman, Linh Maytham, "FINITE ELEMENT MODELING AND UPDATING OF A FIVE-TIERED PAGODA STYLE TEMPLE" (2018). *Civil Engineering Theses, Dissertations, and Student Research*. 118.
https://digitalcommons.unl.edu/civilengdiss/118

FINITE ELEMENT MODELING AND UPDATING OF A FIVE-TIERED PAGODA STYLE TEMPLE

by

Linh Maytham Abdulrahman

A THESIS

Presented to the Faculty of
The Graduate College at the University of Nebraska
In Partial Fulfillment of Requirements
For the Degree of Master of Science

Major: Civil Engineering

Under the Supervision of Professor Richard L. Wood

Lincoln, Nebraska

May, 2018

FINITE ELEMENT MODELING AND UPDATING OF A FIVE-TIERED PAGODA STYLE TEMPLE

Linh M. Abdulrahman, M.S.

University of Nebraska, 2018

Advisor: Richard L. Wood

Historical pagoda style temples demonstrate different dynamic behavior than traditional unreinforced masonry (URM) structures due to the unique construction practices and ornate architecture detailing. Recently, the 2015 Gorkha M_w 7.8 earthquake resulted in widespread structural damage and collapse of similar historic temples in Nepal. However, one temple did not collapse. This is the five-tiered pagoda style Nyatapola temple built in 1702 and located in Bhaktapur, Nepal. Understanding the seismic vulnerability and structural behavior of these pagoda-style temples can lead to more efficient retrofit solutions and conservation practices for similar heritage structures.

This study developed and calibrated the pre- and post-earthquake finite element (FE) models of the Nyatapola temple that are based on post-earthquake reconnaissance efforts. This includes lidar data, visual damage assessment, and ambient vibration test results. A detailed linear time history analysis is conducted to simulate the seismic demands during the 2015 event, and give insight into the performance of pagoda style temples for future seismic events.

The pre-earthquake fundamental frequency of 1.68 Hz is higher than similar Nepali temples, indicating the usually stiff behavior of this temple. The eigenvalue analyses on the calibrated finite element models demonstrated an 11% reduction in fundamental frequency between the pre- and post-earthquake states. This frequency shift indicates a significant reduction of structural stiffness, as evident in the observed post-

earthquake shear cracking. Linear time history analysis results demonstrated maximum displacement and acceleration demands of 67 mm and 0.6 g respectively, under the bi-directional aftershock record pair (M_w 7.3). For this structure, this aftershock record produced the largest seismic demands on the structure.

Significant damage to the earthen URM walls of the Nyatapola temple was observed and is likely a result of induced torsion and poor structural detailing between the wall wythes or layers. Accordingly, this study recommends that strength-based retrofit schemes may be able to increase the connectivity between the wall layers and subsequently reduce future damage to pagoda style structures. These retrofit schemes are anticipated to enhance the resilience of these heritage structures.

DEDICATION

This thesis is dedicated to my parents, my husband “Ali” and my kids “Lana, Zaid, and Leen”. Their constant love and caring are every reason for where I am and what I am.

ACKNOWLEDGEMENTS

Indeed, the patient will be given their reward without account, I am beholden to the highly benevolent and merciful almighty ALLAH whose grace and blessings helped me to reach this far in my academic pursuits.

First and foremost, I express my special appreciation and thanks to my academic advisor, Professor Richard Wood, for accepting me into his group and organizing my academic journey. It has been an honor to be his student. He has taught me, both consciously and unconsciously how good engineering and research is done. Also, I would like to thank the advisory committee members, Dr. Chung R. Song and Dr. Christine E. Wittich for simultaneously encouraging, guiding, and supporting my research ideas and my work.

I would like to thank my husband Ali for being the best husband in the world. Thank you for your love and all your support. Thank you for standing beside me throughout my study and writing this thesis. He has been my inspiration and motivation for continuing to improve my knowledge and move my academic journey forward. He is my rock. I also thank my wonderful children: Lana, Zaid, and our new addition Leen, for always making me smile and for understanding on those weekend mornings when I was studying and writing instead of playing games. I hope that one day they can read this book and understand why I spent so much time in front of my computer.

I also want to thank my parents. I have been extremely fortunate in my life to have parents who have shown me unconditional love and support. The relationships and bonds that I have with my parents hold an enormous amount of meaning to me.

I would like to thank the fellow students who contributed in some way to the work described in this thesis, special thanks to Fayaz Sofi, Mohammad E. Mohammadi, and Elizabeth Moderow. Also my classmates, thank you for listening, offering me advice, and supporting me through this entire process, special thanks to Francys Lopez, Ahmed Rageh, Hani Alanazi, Yijun Liao, Chandana Balakrishna, and Garrett Martindale. I would particularly like to thank Dr. Andre R. Barbosa and Dr. Rajendra Soti, from Oregon State University, who have contributed some ideas, points of view, and feedback related to this work. Special thanks to my friends and family members for all their well-wishes/prayers, phone calls, e-mails, texts, editing advice, and being there whenever I needed a friend, including Zina Maytham, Zahraa Maytham, Zahraa Waleed, and Shams Abdulrahman.

Lastly, I need to thank the HCED for kindly sponsoring my study and created such a good opportunity for me which contributed dramatically in develop and succeed my future endeavors. They have played an important role in the development of my identity and shaping the individual that I am today.

Table of Contents

List of Tables

List of Figures

NOMENCLATURE

Symbol	**Description**	**Units**
D	Dimension [Length]	L
E	Young's Modulus of Elasticity	F/L^2
EW	East-west	Unitless
FEA	Finite element analysis	Unitless
FEM	Finite element model	Unitless
GBL	Ground-based lidar	Unitless
h_i	Height of level i	L
I	Moment of inertia	L^4
Lidar	Light detection and ranging	Unitless
LTHA	Linear time history analysis	Unitless
M	Meter	L
MAC	Modal assurance criterion	Unitless
MPD	Mass proportional damping	Unitless
M_w	Moment magnitude	Unitless
NS	North-south	Unitless
OMA	Operational model analysis	Unitless
OOP	Out of plan	Unitless
PGA	Peak ground acceleration	L/T^2
PP	Peak picking	Unitless
RC	Reinforced concrete building	Unitless
RD	Rayleigh damping	Unitless

Symbol	**Description**	**Units**
SI	System identification	Unitless
SSI	Stochastic subspace identification	Unitless
THR	Time history response	Unitless
URM	Unreinforced masonry	Unitless
P	Mass density	F/L^3
ν	Poisson’s ratio	Unitless
γ_{is}	Interstory drift	Unitless
$\{\Phi_n\}^T$	Complex conjugate and transpose of the nth mode shape	Unitless
Δ_i	Displacement at level i	L
$\lvert\ddot{u}\rvert_{max}$	Maximum absolute floor acceleration	L/T^2
Ω_i	Uncorrelated acceleration amplification ratio	Unitless
Θ	Rotational Angle	Varies

CHAPTER 1: INTRODUCTION

1.1 Motivation

On 25 April 2015, a devastating earthquake struck Nepal of moment magnitude of 7.8. This main shock was followed by an aftershock series, with the largest measuring a M_w 7.3 on 12 May 2015, near the border of Nepal and China at Mt. Everest. This seismic event is commonly known as the 2015 Gorkha Earthquake and resulted in widespread damage to many districts and thousands of houses throughout the country. Given the construction and building inventory of Nepal, numerous cultural heritage sites suffered irreplaceable damage as well as large economic losses to the Nepali economy. Figure 1.1 illustrates an example of damage as a result of the 2015 Gorkha earthquake in Kathmandu and Bhaktapur Durbar Squares. This figure was one of the most-prominent damage photos of an UNESCO world heritage site.

In this work, the structural behavior of historical unreinforced masonry structures are explored using modern finite-element based methods in order to have a better understanding of the structure. The example structure is the Nyatapola temple, a five-story pagoda style temple located in Bhaktapur, Nepal. This is considered as the tallest temple in Nepal. The structural details consist of heavy timber elements with unreinforced brick masonry with the mud-mortar walls that was constructed originally in 1702. This temple is characteristic of pagoda style temples given its tiered towers with multiple overhanging roofs, common throughout the Kathmandu Valley. The distinctive design of the traditional Nepalese pagoda style temples include two important elements: 1) a large roof of the building in several layers that reduce in size with increasing height and 2) a material selection of the dry-masonry core. In detail, four major structural components of these temples include: 1) sun-dried and fired masonry bricks comprising a wall assembled with mud mortar; 2) a roof system with large overhanging eaves at a steep pitch; 3) timber elements from Sal trees used in structural elements such as pillars, struts, and beams as well as for windows, doors, grates, and moldings (Bonapace et al. 2003); 4) foundations which may be built on older foundations or unknown in construction. In the Nyatapola temple, the temple sits on top of a five-level plinth.

Figure 1.1: Examples of the UNESCO world heritage sites in Kathmandu and Bhaktapur Durban squares destroyed by Gorkha earthquake, 2015 (Nepal Current News 2015).

During the Gorkha earthquake and its aftershock sequences, the Nyatapola temple remained standing but with extensive cracks up to 30 mm at the first floor, as illustrated in Figure 1.2. While this temple sustained extensive damage, other Nepali temples did not fare so well as evident through complete collapses. This further substantiates the interest to study the Nyatapola Temple under the ground motion sequence. Through understanding the response of this structure, engineering knowledge can be gathered into the response of Pagoda style temples for potential retrofit schemes, improve structural designs to minimize risk and losses, and preservation of cultural heritage. This last reason is in-line with the mission of UNESCO's report which aims to reduce the losses caused by earthquakes to heritage sites around the world (Brando et al. 2015). Figure 1.1 shows examples of the severe damage of the UNESCO world heritage sites in Kathmandu due to Gorkha earthquake, 2015.

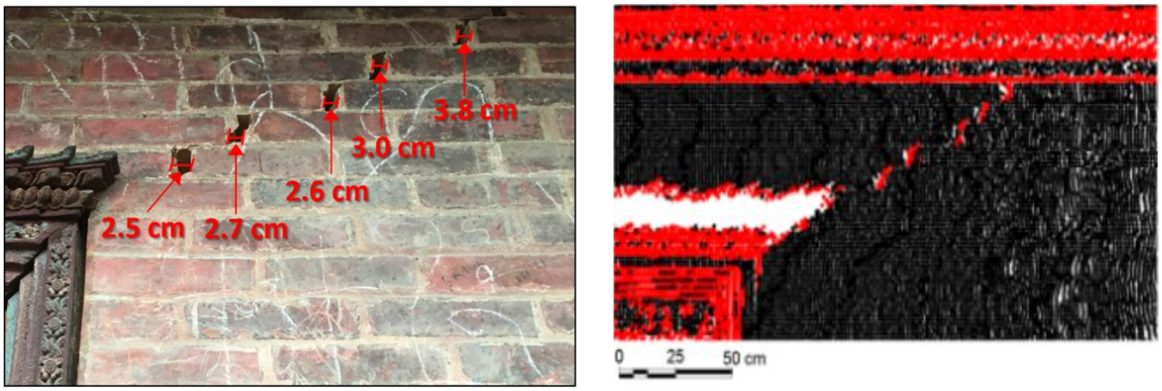

(a) (b)

Figure 1.2: North wall of Nyatapola temple at first floor: (a) dimensions of significant cracks and (b) red spots show the defects detected by lidar (Wood et al. 2017).

1.2 Overview of work

This study focuses on the five-tiered pagoda style Nyatapola temple, one of the most prominent temples in Nepal. A series of methods followed in this study assess the building damage and study the system's behavior by using a finite element technique and linear time history analysis to determine the fundamental frequency and mode shapes, as well as the torsional drift resulting from the 2015 Gorkha earthquake. The finite element model has been successfully calibrated using operational modal analysis results from others with additional optimized geometric details from a detailed lidar point cloud as well as material parameters as guided by a literature survey.

In this study, an initial FEM of the historical URM Nyatapola temple has been generated within SAP2000 based on the real structure dimensions which extracted from the data collection using a remote sensing method (lidar) in order to get accurate in-situ measurements. The pre-earthquake (initial) FEM was calibrated based on the material properties available in the literature and ambient vibration test data (Jaishi et al. 2003). Using the pre-earthquake initial FEM, an updated post-earthquake FEM was guided by the visual damage assessment, lidar data collected on site, and post-earthquake ambient vibration results conducted by (Wood et al. 2017b). The damage to the masonry walls was simulated through a reduction of Young’s modulus in the region where the significant cracks were identified. The shortening in the fundamental frequency of about 11% between pre- and post-earthquake calibrated models can provide a quantification for an extent of damage in terms of change in dynamic characteristics.

To evaluate the damage patterns and response of the structure, the linear time history analysis method was implemented using SAP2000. Rayleigh damping of

Nyatapola models was set at 5% of critical for the first and third modes. Linear time history was conducted using the mainshock on the pre-earthquake model and the significant aftershock on the post-earthquake model. Various responses were extracted for assessment including the floor displacement, interstory drift, absolute floor acceleration and uncorrelated acceleration amplification ratio for two-dimensional ground motion records. By synthesizing the results of the displacement demands, the torsional demand profiles were generated and compared the results with the estimated torsional permanent drift profiles from lidar by Wood et al. (2017b). Studying the impact of the in-structure spectral acceleration response is an essential step to provide a valuable insight into the force distribution and structure filtering that may guide future retrofit designs. Finally, two different damping models were applied for the post-earthquake FEM as a damping case study to provide an insight into the effect of the damping on the structural behavior. This damping case study was conducted to explore the influence of Rayleigh damping versus mass proportional damping, which is found in new modeling strategies of the applied element method.

1.3 Scope of Research

The scope of research focuses on the numerical modeling of the structure of the Nyatapola temple to study the structural response and evaluate the damage due to the Gorkha earthquake. These numerical models are developed and calibrated using knowledge gained from relevant literature, pre- and post-earthquake data collected from ambient vibration testing, lidar scans, and visual damage assessment. Additionally, careful selection and necessary iterations are required for a calibrated and represented model. The dynamic properties and damage detection of the Nyatapola structure are quantified through eigenvalue and linear time history analyses, in this work. The overarching scope was to examine the linearly elastic response of the structure as an initial step for detailed forensic analyses. This is a first step that needs to be successfully completed before nonlinear and inelastic characteristics of masonry structure can be incorporated into an FE analysis.

1.4 Organization of Thesis

This thesis consists of six chapters. Chapter 1 describes the introduction, motivation, and scope for the work. Chapter 2 presents a brief literature as relevant to the seismic vulnerability assessment of earthen URM structures, seismological overview to Nepal and the Himalayan region, the 2015 Gorkha earthquake and aftershock, finite element modeling, and linear time history. Chapter 3 describes the Pagoda style characteristics in general and the Nyatapola Temple features. Chapter 4 presents the modeling development which was performed in SAP2000 platform, as a detailed presentation to the modeling contribution in Wood et al. (2017). Chapter 5 presents the linear time history response of the temple and summarizes various response quantities. Chapter 5 is tentatively planned for a collaborative journal paper relating to the finite and applied element method modeling of this structure. Chapter 6 outlines the research conclusions and recommendations for future work. Appendix A includes detailed results of the maximum interstory drift distribution. Appendix B contains detailed results of the maximum floor acceleration distribution. Appendix C includes detailed results of the uncorrelated acceleration amplification ratio.

1.5 Acknowledgement

This data collected was partially supported by the University of Nebraska Foundation and the UNL College of Engineering. Other financial support was provided by the National Science Foundation through grants 1545632 and 1545595 provided to Oregon State University and the University at Buffalo, respectively. The collaborative work of this effort significantly improved the quality of this thesis. The 2015 Gorkha ground motions were processed and provided by Prof. Domniki Asimaki of Caltech. Guidance on the model was provided by Prof. Andre R. Barbosa of Oregon State University. Lastly, the original point cloud was registered and initially processed by Ph.D. student, Mohammad Ebrahim Mohammadi, within the same research group. The views and opinions of participators expressed in this thesis do not necessarily state or reflect those of the sponsors or the external collaborators.

CHAPTER 2: LITERATURE REVIEW

In this chapter, a selected literature review will outline the seismic vulnerability of earthen unreinforced masonry structures, the seismological overview of Nepal and the Himalayan region, and the 2015 Gorkha earthquake and its aftershock sequence. This chapter will also provide a brief overview of finite element modeling (FEM) and linear time history of FEM. The select sections will outline previous research to provide insight and a technical background for unreinforced masonry historical buildings under seismic loads, along with a background for modeling strategies used to evaluate structure seismic vulnerability. This literature review describes the approach and assessment of the five-story pagoda style temple presented in later chapters of this thesis.

2.1 Seismic Vulnerability Assessment of Earthen URM Structures

Earthen unreinforced masonry (URM) structures are common throughout southeast Asia and Nepal. However, these structures are vulnerable to lateral loads induced by seismic events, and can led to severe destruction through severe cracks (predominately shear) and life-safety hazards because of out-of-plane and in-plane wall collapses. This is primarily due to the design detail of the lateral-load resisting system and the connection between the walls and the confining structural elements (floor diaphragms in temples and beam and column elements in other structures). Following the 2015 Gorkha earthquake and its aftershock sequence, widespread damage was observed throughout Nepal. Figures 2.1 and 2.2 illustrate some damaged URM and reinforced concrete structures.

In a comprehensive study for a close collaboration between an architecture and an anthropologist of Nepali culture, Bonapace and Sestini (2003), conducted a study illustrating the traditional materials and construction techniques used throughout the Kathmandu Valley. Details of unreinforced masonry wall, roof system, beams, columns, pillars, and struts, as well as timber connection, have been discussed. Figure 2.3 illustrates the traditionally manual construction process of temple structure.

(a)

(b)

Figure 2.1: Example on URM buildings in Bungmati and Bhaktapur areas following the Gorkha earthquake: (a) complete collapse of URM buildings and (b) typical out- of-plane collapse of URM walls (Brando et al. 2015).

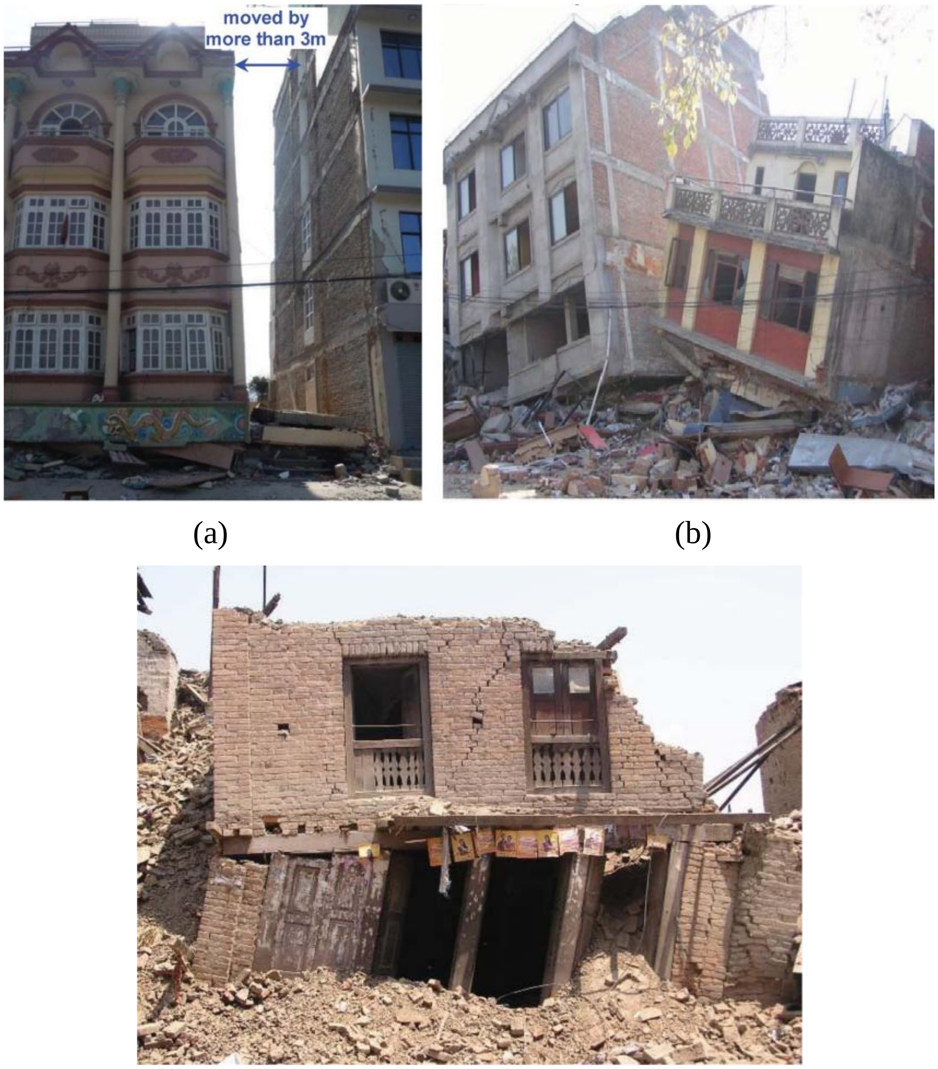

(a) (b)

(c)

Figure 2.2: Example damage following the 2015 Gorkha earthquake: (a) a four-story RC building moved approximately 3 m horizontally from an adjacent building in Sitapaila, Kathmandu, (b) soft story failure of two adjacent buildings in Sitapaila, Kathmandu, and (c) collapse of a three-story URM building in Nikosera, Bhaktapur (Rai et al. 2016).

(a) (b)

Figure 2.3: Traditional manual method used in brick fabrication in the Kathmandu Valley: (a) preparation of the clay and insertion into the mold and (b) surface finishing (Bonapace and Sestini 2003).

In one study by Shakya et al. (2012), the authors discussed the structural weakness features and the seismic performance of Nepali Pagoda temples by investigating three different pagoda temples, namely: Shiva, Lashmi Narayan, and Radha Krishna temples. In their study, the authors created a finite element model, which is complex in nature, and a parametric analysis study was conducted to understand the effect of damage and degradation in terms of period elongation and the seismic vulnerability of structural components. This study provides a methodology to construct FEM pagoda style temples through induced damages in terms of reducing the Young’s modulus.

In a follow-up study, Shakya et al. (2014), performed a seismic sensitivity analysis for common structural components found within Nepali Pagoda temples. Traditionally, Nepali pagoda temples have similar structural characteristics and the three previous pagoda-style temples were again chosen in this study. In this work, the authors focused on the weak connectivity between the layers of the brick masonry wall, as the most vulnerable structural component in the temple. Despite this study, further work is needed to understand the local behavior and structural vulnerability.

The poor construction methods used in the Kathmandu region made the infrastructure vulnerable to extreme levels of damage under the anticipated seismic hazard. Rai et al. (2016), surveyed damaged following the 2015 Gorkha earthquake. During the Gorkha earthquake and its aftershocks, numerous reinforced concrete (RC) buildings in the Katmandu valley were damaged due to the weak reinforcement columns, open ground level leading to soft stories, inadequate masonry infill walls, and geometric irregularities, as presented in Figures 2.2a and 2.2b. In addition, most URM buildings experienced severe cracks to complete collapse as shown in Figures 2.1 and 2.2c.

Another parallel set of researchers, Wood et al. (2017b) predating most of this thesis work, outlined a methodology to combine ambient vibration-based operation model analysis with 3D ground-based lidar in order to study and assess the damage of the Nyatapola temple. The operational modal results provided estimates of the first four frequencies, respectively as 1.507, 1.524, 2.554, and 3.262 Hz. Results and data collected in this study have been used to calibrate and update FE models in this work, as described in Chapter 4.

2.2 Seismological Overview to Nepal and the Himalayan Region

The region south of the Himalayas is seismically active due to the collision of the Indian and the Eurasian tectonic plates. This collision zone results in numerous earthquakes as well as the uplifting of the Himalaya mountains (Takai et al. 2016). In this region, specific to Nepal, three large earthquakes have been observed in modern times including ones in 1833, 1934, and 2015 with moment magnitudes of 7.7, 8.3, and 7.8 respectively. The seismic zone from Islamabad to Kathmandu which extends along the Himalayan seismic belt is still active where Lei et al. (2017), predicts that an additional earthquake with the moment magnitude (M_w 8.4 - 8.8) will occur in this seismic zone in the next 10 years. Figure 2.4 shows a geological map for the Nepal region and the movement of the Indian subplate underneath the Eurasia plate.

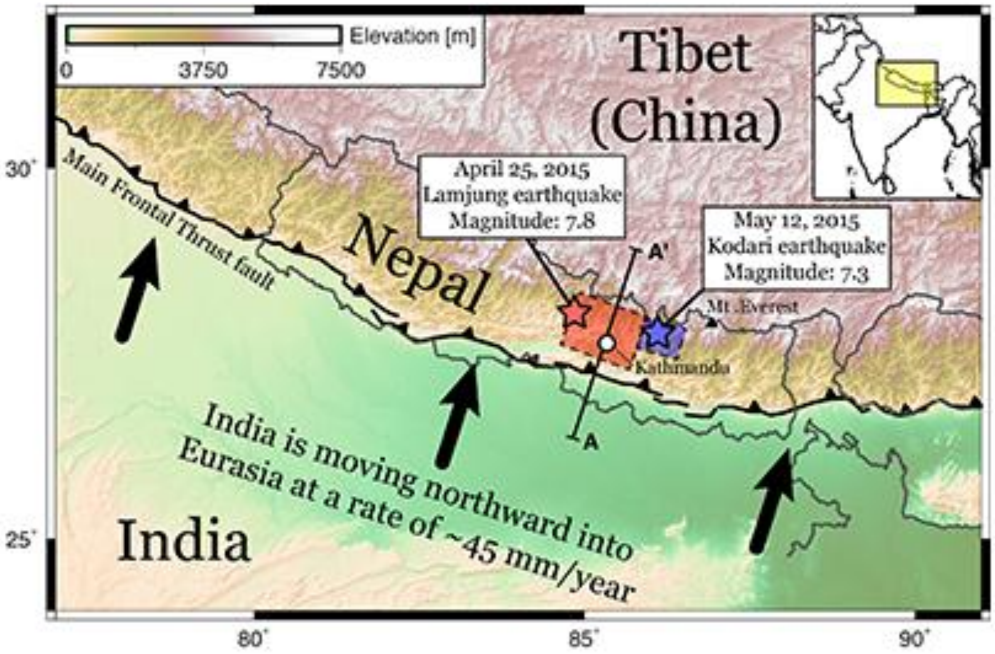

Figure 2.4: Geological map for tectonic plates boundaries of Nepal region (Faculty of Science 2015).

In the recent work by Paudyal and Panthi (2010), the authors summarized the larger events in the central Himalayan region. Figure 2.5 illustrates the chronological history of events that have occurred in or near Nepal from 1803 to 2006. As previously identified, a seismic gap was noted due to the absence of large events for more than 50 years. The authors highlight the continuous threat as moderate to high seismicity in the region given its history.

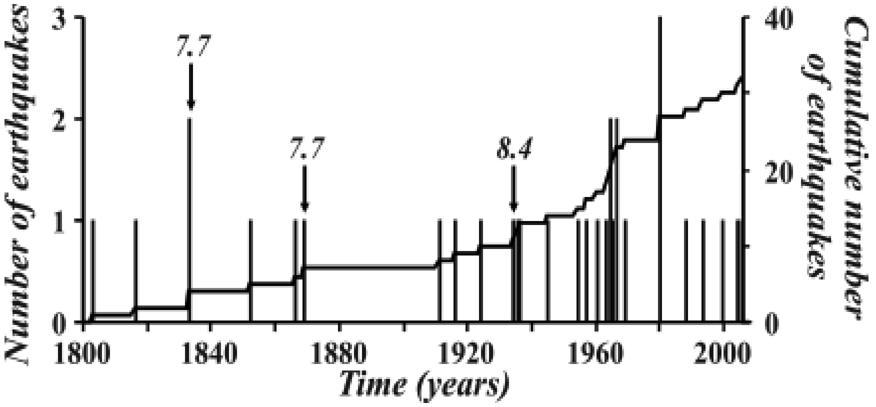

Figure 2.5: Large earthquakes occurred in Nepal and its adjoining regions in Central Himalaya in order of high- low-high-low phases of seismicity from 1803 to 2006 (Paudyal and Panthi 2010).

Dhital M. R. (2015), demonstrated a panorama study for Himalayan geology stretching from the west to the east. The author reported the essentially longitudinal geological zones in Nepal by classifying it into active Himalayan foreland basin, Siwaliks and Intermontane basins as well as Lesser Himalayan, Higher Himalayan, and Tethyan Himalayan which are distributed from the south to the north, respectively. The variation of sediment in the Kathmandu basin contributes to the observed ground motion amplification. The spectral ground accelerations due to fluvio-lacustrine sediments played a major role in intensifying the ground motion, leading to observed damage patterns in the Kathmandu Basin (Paudyal et al. 2013). In another study by Galetzka et al. (2015), the authors observed a basin-effect amplification of long-period energy between 1 and 9 seconds, with horizontal-direction energy amplified by six to seven times when compared to bedrock sites. The amplified energy was most pronounced at a period of 4 seconds in the Kathmandu basin.

2.3 2015 Gorkha Earthquake and its Aftershock Sequence

A large earthquake of M_w 7.8 occurred on April 25, 2015, at 11:56 am local time along of the main Himalayan thrust fault in central of Nepal. It struck the village of Barpak, Gorkha district of central Nepal. The epicenter was located at (28.15º N, 84.70º E) about 80 km NW of the capital Kathmandu and hypocenter at the depth of approximately 15 km (9.3 mi). Followed by 480 aftershocks of local magnitude equal to or greater than 4 where the largest noticeable aftershock on May 12, 2015 (M_w 7.3) occurred at the border between the Mt. Everest and the capital Kathmandu (Rai et al. 2016; Chaulagain et al. 2018).

In a study about the geodetic model of April 25, 2015, M_w 7.8 Gorkha Nepal Earthquake and M_w 7.3 aftershock estimated by Feng et al. (2015), the combined inversion data of InSAR and GPS showed that this event is a reverse fault motion, with a slight right-lateral strike-slip component. Figure 2.6 shows the major historical earthquakes through the Himalayan arc including the locations of the mainshock of Gorkha earthquake and its sequences. Figure 2.7 illustrates another Nepal map which highlights the locations and the magnitudes of the main and aftershocks of Gorkha earthquake series.

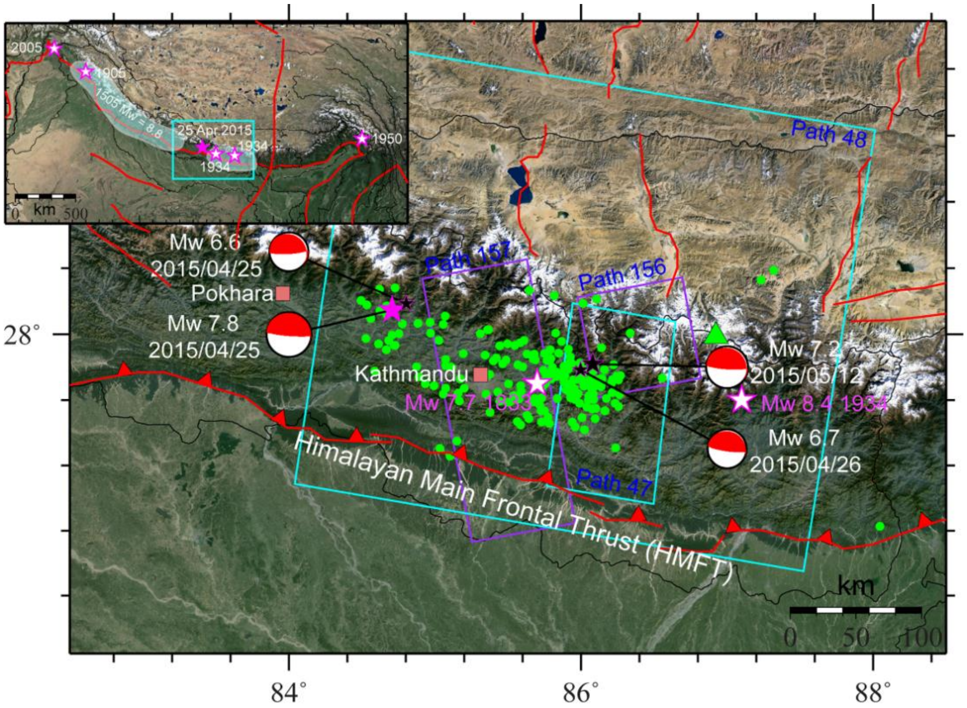

Figure 2.6: Location map presents the major historical earthquakes in the Himalayan region where the main shock is reported by magenta stars. Green dots show the locations of aftershocks $M_w > 3$ while the black stars represent the aftershocks $M_w > 6.5$. (Feng et al. 2015).

Figure 2.7: Map of Nepal showing the location of the main and aftershocks of Gorkha earthquake (Medecins sans frontiers 2015).

The ground motions of the 2015 Gorkha earthquake recorded throughout the Kathmandu Valley are available in Takai et al. (2016). Four station locations were reviewed throughout the Kathmandu Valley, namely: KTP (Kirtipur Municipality Office, Kirtipur), TVU (Central Department of Geology, Tribhuvan University, Kirtipur), PTN (Pulchowk Campus, Institute of Engineering, Tribhuvan University, Patan), and THM (University Grants Commission Office, Sanothimi, Bhaktapur), which are distributed from west to east. Kathmandu Valley is surrounded by mountains and filled with soft lake sediments. To understand Kathmandu basin effects to the strong ground motion, KTP-station was established on a rocky soil while the remaining three sites were established on the sedimentary sites. The authors concluded that the horizontal long-period oscillations on the sedimentary sites had more damage causing influence on high-rise buildings with natural periods of 3 to 5 seconds compared to rock sites. The Nyatapola temple site (Bhaktapur) with a lower natural period of 0.596 s (Jaishi et al. 2003), implies that this relatively stiff structure should experience seismic demands as compared to buildings within periods of 3 to 5 seconds.

2.4 Finite Element Modeling and Model Updating

In this section, a brief literature review for finite element modeling and model updating is provided for unreinforced masonry buildings (URM), particularly of Pagoda style temples. With the advances of modern computers, the finite element method has been extensively used in literature to idealize complex civil engineering structures for better understanding of system behavior and response predictions. URM structures provide diverse structural behavior, particularly dynamic characteristics, for their complexity in material composition, architectures and variability in construction of individual building component (e.g., joints, foundation, added mass on structures, layered walls, roof architecture etc.). This added complexity of URM buildings makes model calibration a challenging task for using the updated models in response predictions or understanding of system behavior. Previous efforts on model updating of URM structures are also briefly reviewed in this section.

2.4.1 Finite Element Modeling

In one study focused on the modeling of historical masonry structures, Lourenco (2002), used three numerical modeling strategies, including: detailed micro-modeling, simplified micro-modeling, and macro-modeling. The URM shear wall was modeled using a macro-modeling approach, which was adequate for structures consisting of solid or layered walls similar to those found in Pagoda style architecture. The author concluded that using finite element continue structural models (macro-elements approach) is more practice-oriented, owing to reduce time and memory requirement, where it is more valuable when a compromise between accuracy and efficiency is needed. Additionally, the accuracy of the results when using macro-modeling strategy highly depends on the element size (mesh discretization).

In a study about the experimental and numerical modal analyses of a historical masonry palace, Aras et al. (2011) presented the determination of model properties of a three-story historical Beylerbeyi masonry palace in Istanbul. In this study, the ambient vibration method was used to represent the experimental study and an accompanying FEM to perform a numerical investigation on structure. A 3D finite element model was generated using shell elements for masonry walls and frame elements for the column and timber slab members. The modulus of elasticity of masonry was used by the authors as a calibration parameter for model updating due to higher uncertainty associated with this parameter.

One of the most important problems in generating FE models of historic masonry buildings is the lack information for the material properties. Atamturktur et al. (2014) highlighted the validation and uncertainty quantification of numerical models of masonry monuments arising from input parameters (simplifications and assumptions in the modeling process) and lack of experimental measurements, leading to incorrect response predictions for the management of cultural heritage. The study highlighted best practices for developing finite element models for the masonry monuments including calibration procedures with quantified uncertainty bounds.

2.4.2 Model Updating

Model updating forms an important step in generating numerical models that provide responses calibrated to experimental measurements. Generally, the model parameters that show higher uncertainty or variability are fine-tuned within their prescribed ranges (complacent with the physical meaning of these parameters) to develop a validated numerical model for further investigations of interest. The preferred modeling updating parameter for URM and concrete structures can be seen as modulus of elasticity property for materials due to its higher uncertainty and variability in URM and concrete structures (Ventura et al. 2001; Aras et al. 2011; Oliveira et al. 2012, Wood et al. 2017).

Moreover, different procedures and methods can be seen in literature for model updating of URM structures, such as Ventura et al. (2001, 2005) using automatic updating technique based on ambient vibration test data on the heritage buildings. The modulus of elasticity for masonry was fine-tuned to establish a good correlation between experiment and analytical natural frequencies, and MAC values for mode shapes. Kodikara et al. (2016), also performed modal updating using ambient vibration data on a ten-story concrete building for updating elastic modulus property in the numerical models.

2.5 Linear Time History

Dynamic structural analysis enables a forensic investigation into the response of the structure to earthquake motions. This section will address one of the dynamic analysis methods and linear time history analysis (LTHA). The selection of the LTHA is simple and a less computationally intensive approach than more rigorous nonlinear time history analysis for characterization of dynamic response of URM structures.

Marjanishvili (2004) compared the three most effective analysis procedures (linear elastic static, linear elastic time history, and nonlinear time history) in evaluating the progressive collapse potential of existing buildings and in designing new buildings to resist this type of collapse. Among dynamic methods, LTHA was concluded by the author as less time consuming with moderate complexity, requiring relatively less extensive validation of findings than NLTHA. The latter can be unnecessarily complex and highly computational intensive on URM structures requiring extensive validation and verification of findings.

Oliveira et al. (2012) conducted a study of 11 minarets using linear dynamic analysis of these heritage buildings in Istanbul. These structures had previously suffered significant earthquake damage and linear time history analyses were performed as a successful method to access their earthquake risk level by developing an empirical formula for estimating the first frequency of vibration. This formula considers that the frequency is proportional to the square root of the second moment of area and almost inversely proportional to the square root of the height of the minaret. The proposed formula has the importance to offer an expedite tool for the structural engineer to have a first estimate of the minaret response to a given earthquake input.

2.6 Summary

A literature survey was provided in this chapter on linear time history analysis of unreinforced masonry structures, using finite element models calibrated to ambient vibration data. Model updating of numerical models was seen as a critical step for reliability of response predictions and risk assessment in earthquakes, more importantly for URM type constructions. Invariably, modulus of elasticity property for material was seen as the preferred updating parameter for model calibrations based on ambient vibration data.

Dynamic analysis of URM structures such as heritage buildings and temples for risk assessment to earthquake events is a challenging problem for their variability in typical construction practices, integrity of structural components (plinth, layered walls, roof system etc.), and material heterogeneity, besides complexity and diversity of architectures used. The main objective of this study is to build on the previous research efforts and perform a detailed dynamic analysis of pre- and post-earthquake finite element models of Pagoda style Nyatapola temple in Nepal for characterization dynamic properties, and structure response to 2015 Gorkha event.

CHAPTER 3: PAGODA STYLE CHARACTERISTICS

3.1 Introduction

Prior to the 1934 Bihar-Nepal earthquake with a magnitude of M_w 8.3, the vulnerability of Nepal structures was unknown in recent times. This 1943 event caused severe damage to buildings and temples throughout the Kathmandu Valley and entire country of Nepal (MoHA and DPNet 2009). This seismic event highlighted the need for structural retrofits to reduce their vulnerability. The historical structures continually have been unable to resist earthquake forces due to the basic construction materials. Construction techniques and building methods were focused on the environmental conditions rather than the earthquake loads (Beckh 2006). In this chapter, theoretical overview of the traditional construction and design details are presented, as well as discussing the characteristics of a five-tiered pagoda style temples in Kathmandu valley, Nepal.

3.2 Nepalese Temple Features

Bhaktapur Durbar square contains many traditional buildings and historical temples that are constructed of unreinforced masonry (URM). The historic temples are tiered with multiple overhanging roofs of the pagoda style as shown in Figure 3.1. Pagoda temples were constructed due to the religious and cultural beliefs. Although there are different construction styles of Pagoda temples, similar structural concepts contain the overall shape, construction technologies, and the materials. Pagoda style temples have distinct characteristics compared with other Nepalese temples that can be summarized as: (Shakya et al. 2014; Menon et al. 2017):

- Square vast plinth to limit shear forces at the foundation.
- Large wall thicknesses comprised of mud-masonry brick.
- Walls constructed of three layers with decreasing story heights.
- Heavy timber frame elements embedded in walls to support the roof dead weight.
- Multi-tiered roof levels with timber overhangs to protect the masonry walls from heavy rain and the sun.
- Inclined timber struts to support the roof and transfer the load from purlins to the masonry wall.
- Covering timber roofs by tiles or metal for protection.

Pagoda style temples consist of four essential components, namely: masonry walls, roof systems, timber members, and foundations. An example view of the Nyatapola Temple is provided in Figure 3.1.

Figure 3.1: View of Nyatapola Temple in Bhaktapur, Nepal (Chandra Niraula 2016).

3.2.1 Masonry Wall

The main gravity and lateral load-bearing system in pagoda temples is a brick masonry wall. These are constructed with three layers of sun-dried/fired bricks with mud mortar, as illustrated in Figure 3.2. The outer-face of the wall is made of fired clay brick to protect the temples from any external fire, while the inner face uses bricks that made of sun-dried bricks due to limited environmental exposure. Rubble, pieces of bricks, and mud mortar are used in the middle core wall as the connection layer – which is vulnerable to earthquake loads (Nienhuys 2003; Beckh 2006). These three layers comprise a total wall width that can vary between 50 to 75 cm. The thickness of the wall typically decrease with increasing floor level (Shakya et al. 2014). The outer wall bricks which differ from the inner materials, as shown in Figure 3.3a, can contribute to cracks as a result of environmental effects of humidity, dryness, and rain. During small frequent and regular vibrations, the grains of the filling layer fall into the cracks which restrain the outer layer from its original location (Figure 3.3b). This movement causes distention and weakness of the wall that can be reduced by tying these layers together using strips (Figure 3.3c), (Nienhuys 2003). The construction styles in Pagoda temple are not ideal to carry the heavy gravity loads due to the low strength and ductility of masonry materials. This is further exacerbated when considering seismic loads.

3.2.2 Roof System

Nepali architectural details are evident in the selected timber roof systems. Characteristics include a steep roof pitch with overhanging eaves. In respect to the roof system, Pagoda temples can be distinguished by one roof, two roofs, three roofs, or five roofs. These roofs were designed based on climate and weather to limit these detrimental effects from both monsoon rains and extreme sun exposure. Figure 3.4 displays the roof construction details of the Pagoda style temples. The symmetrical pitches of the temple roofs are made up of small rafters stemming from each corner in a radial configuration to the central point of the structure (Bonapace and Sestini 2003). The inner rafters are connected to the primary structural masonry walls via beams, while the outer rafters are banded with purlins which are supported by wooden struts. The inclined timber struts play an essential role in distributing the roof loads to the wall. All of the wooden elements are held together using wooden wedges (Shakya et al. 2012; Shakya et al. 2014). Figure 3.5 illustrates the typical roof details used in Pagoda style temples.

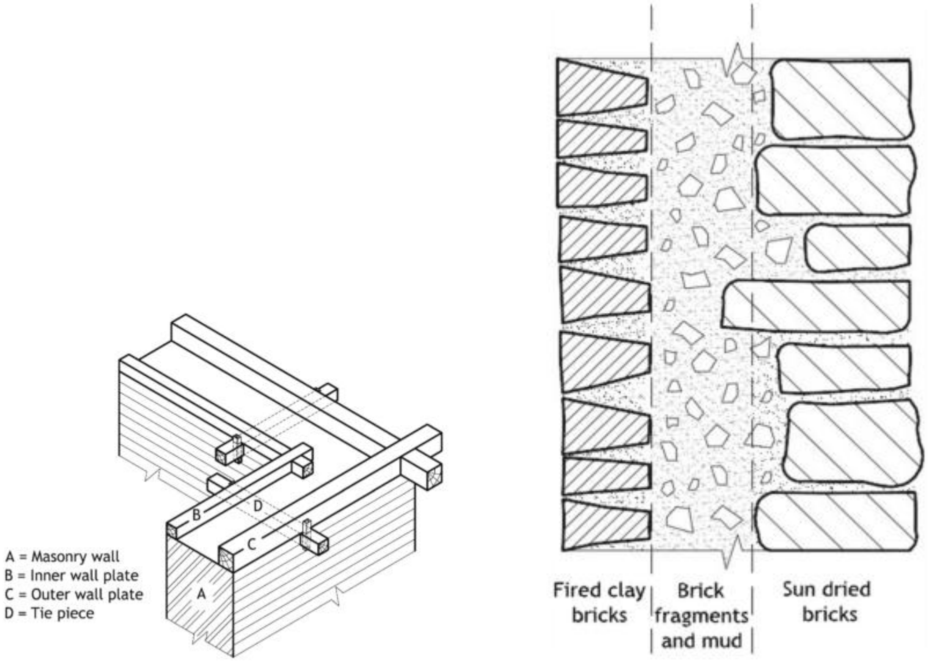

(a) (b)

Figure 3.2: Wall cross-sections: (a) wall connection and (b) wall layers (Shakya et al. 2014).

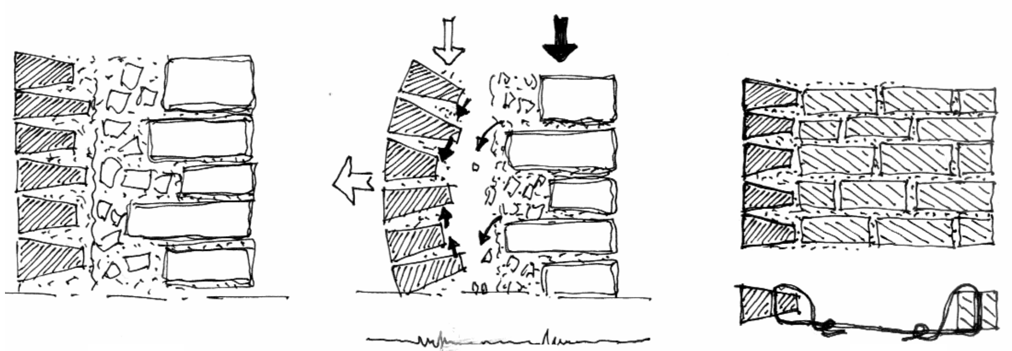

(a) (b) (c)

Figure 3.3: Traditional design of wall layers: (a) wall layers before loading, (b) bulge between wall layers, and (c) tying the wall layers using strips (Nienhuys 2003).

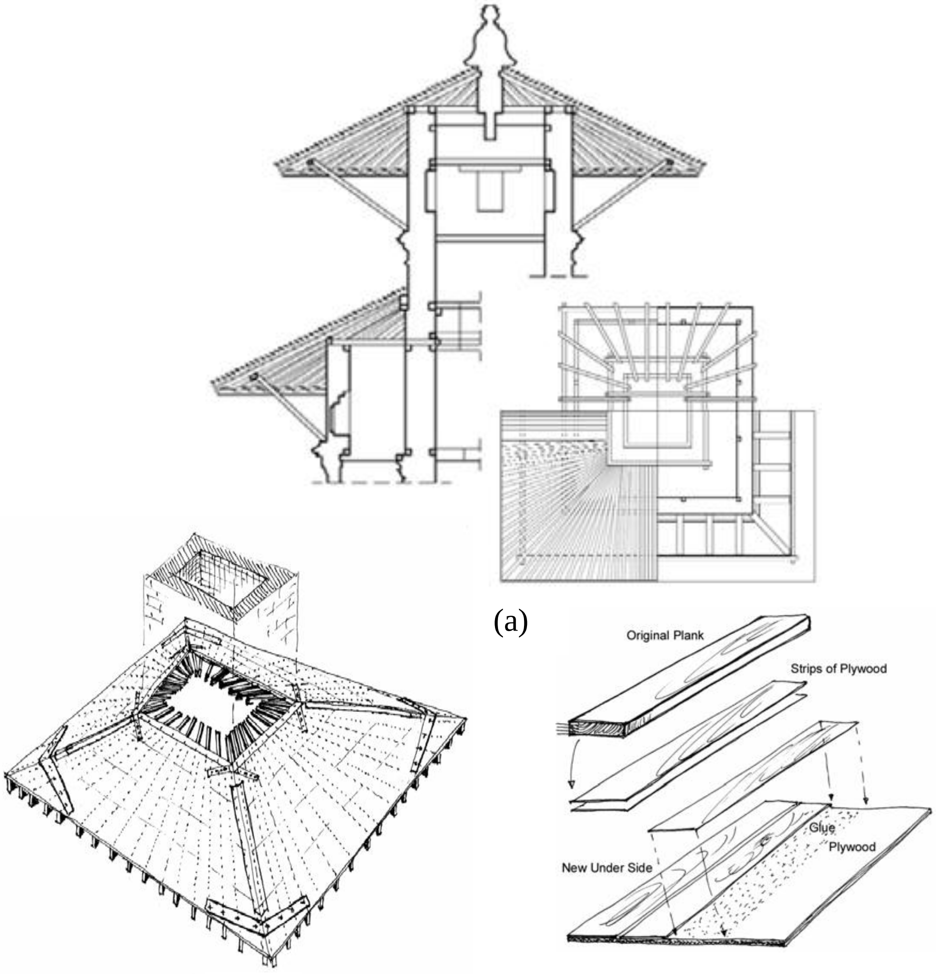

(a)

(b) (c)

Figure 3.4: Typical roof detailing: (a) timber pitches in a radial configuration, (b) roof connection using wood connectors at corners, and (c) plywood (Bonapace et al. 2003; Nienhuys 2003).

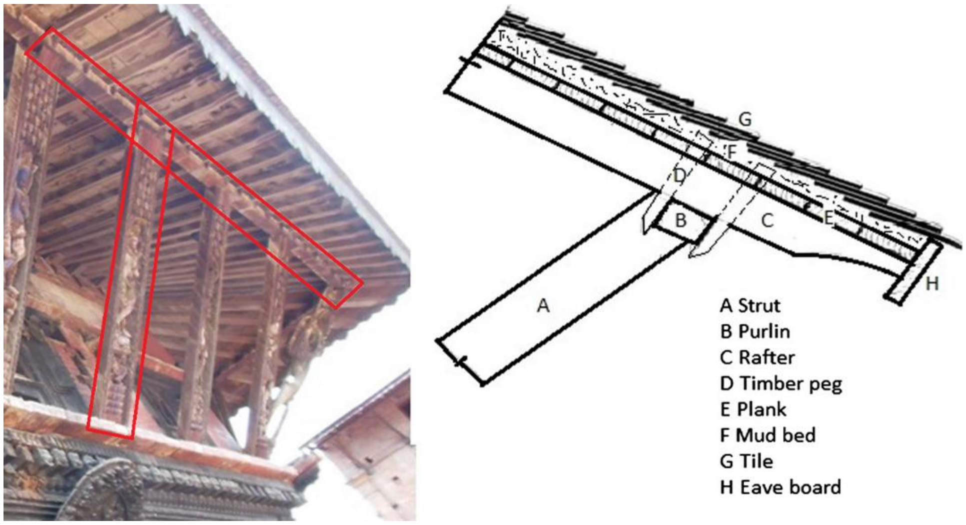

(a) (b)

Figure 3.5: Common traditional timber joinery in Pagoda temples: (a) roof-overhangs held by inclined timber struts and (b) timber peg joint (Shakya et al. 2014).

3.2.3 Timber Members

Nepal contains very abundant timber resources with an estimate of 5.8 million hectares or 39.6% of the total area of Nepal. (Kanel and Dahal 2008). The abundance of forests provides a variety of timber used in construction such as the Sal, Gwaisasi, Salla, Sati Sal, and Sisau trees. Within the Kathmandu Valley, the Sal tree is most commonly used due to its availability, wide cross-section, strength, and long lengths (up to 30 m). It is used in building structural elements such as beams, columns, pillars, and struts as well as for nonstructural elements like doors, windows, pinnacle, and decorations (Bonapace and Sestini 2003).

Although Sal wood is of high quality and strength, its resistance to the climate-changes like humidity, rain, and glowing sun during the summer is low. Exposed columns are subjected to water damage which may cause loss of stiffness and rot. This may influence both structural elements like columns and beams timber and nonstructural components such as wooden lintels over doors and windows. (Nienhuys 2003). Figure 3.6 illustrates a rotted column at its base due to poor drainage at a pagoda temple, reducing its fixity at the base as well as its ability to resist lateral forces.

Figure 3.6: Base column rotted due to rain (Nienhuys 2003).

Furthermore, timber plays a significant role in the connections. Connection and construction details include nails, anchorages and ring embedded in hardwood, and peg connections between wooden members. The vertical and horizontal structural elements are often tied together to provide additional bracing and stiffness accounting for increased connection rigidity (Nienhuys 2003; Bonapace and Sestini 2003). Figure 3.7 demonstrates the common timber connection techniques.

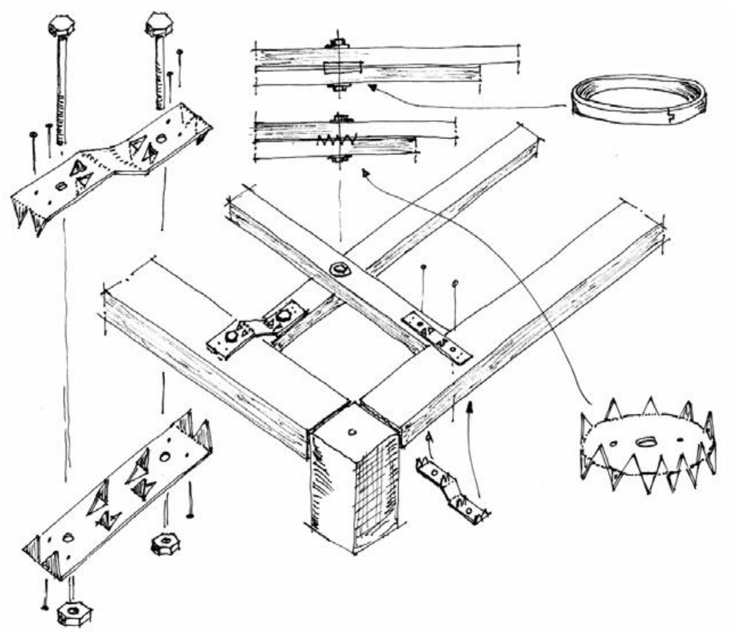

Figure 3.7: Connection timbers using special techniques (Nienhuys 2003).

3.2.4 Foundation

Common to pagaoda style temples are a square floor plan that are constructed on a vast multi-tier plinth as shown in Figure 3.8. However, there are no internal details about the foundation design. These massive square foundations stand on a pyramidal shape that range ranging from 1-5 meters. At the Nyatapola temple, the plinth extends up to 7 meters in height, the largest of all Nepali pagoda temples. No observed or general damage has been observed in the plinths. Following the 1934 Bihar earthquake, some collapsed temples were rebuilt on the same foundation since they were still identified to be adequate. Previous researchers have identified that the large foundation plinths may limit shear at the base of the temple (Nienhuys 2003; Shakya et al. 2012).

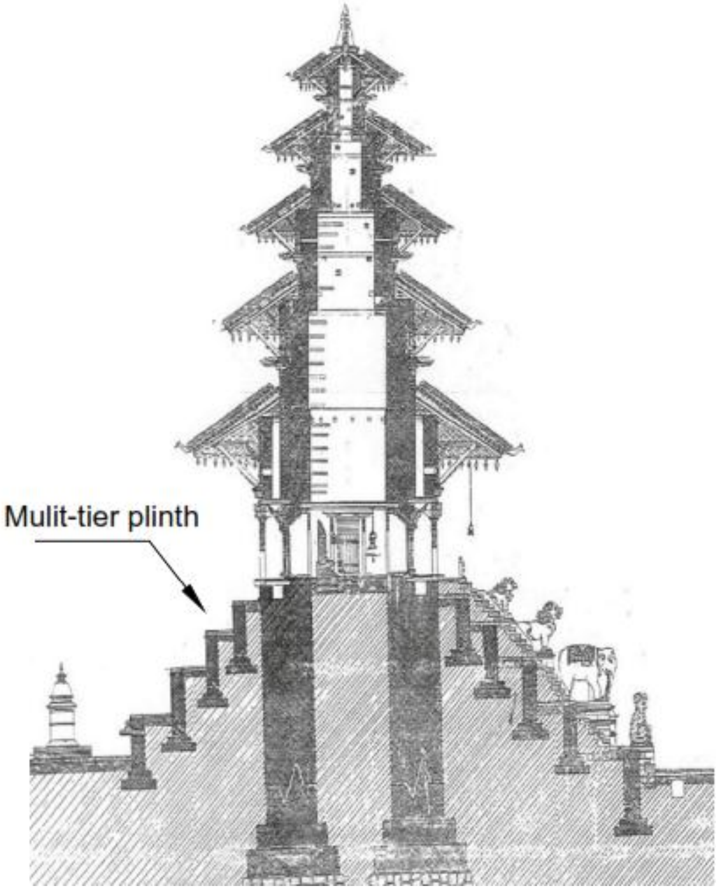

Figure 3.8: Nyatapola section highlights the multi-tier plinth at its foundation (Shakya et al. 2014).

3.3 Nyatapola Temple

Nyatapola temple is a five-story pagoda style temple which located in Bhaktapur in the east corner of the Kathmandu Valley, Nepal. It is the tallest temple in Nepal with a height of 22 m on top of a five-tiered plinth of 7 m. The structural details consist from unreinforced brick masonry walls with the mud-mortar and timber members. The five-tiered temple was built in 1702 A.D and still in existence today, as illustrated in Figure 3.11a. The distinctive roof systems surround all levels of the temple, where the wall thicknesses vary from 1.40 m at first level to a minimum value of 0.67 m at the uppermost level.

Given the cultural importance of this temple, numerous studies were completed following the 1934 Bihar earthquake and before the 2015 Gorkha earthquake to understand the structural weakness, seismic vulnerability, and likely damage to minimize the irreplaceable damage. One previous study, conducted by Jaishi et al. 2003, examined the dynamic properties. These authors utilized ambient vibrations to identify the modal parameters due to its economic deployment relying on naturally occurring excitation provided by wind and pedestrian traffic activities. Figure 3.9 represented an example instrumental to collect ambient vibration data. Jaishi et al. (2003) collected ambient vibrations during December 19 – 30, 2002. Their setup included 11 sensors on each of the temple levels. The operational modal analysis (OMA) was performed using the stochastic subspace identification (SSI) method, which provided more stable results in comparison to peak picking (PP) (Peeters et al. 2000). Table 3.1 presents the OMA dynamic properties results for the Nyatapola temple. The fundamental frequency of 1.68 Hz is much stiffer than other Nepali temples. The results indicate that the first and fourth modes are bending in the north-south direction, while the second and third modes are bending in the east-west direction. The higher modes, fifth and sixth, are represented as torsional modes about the Z-axis.

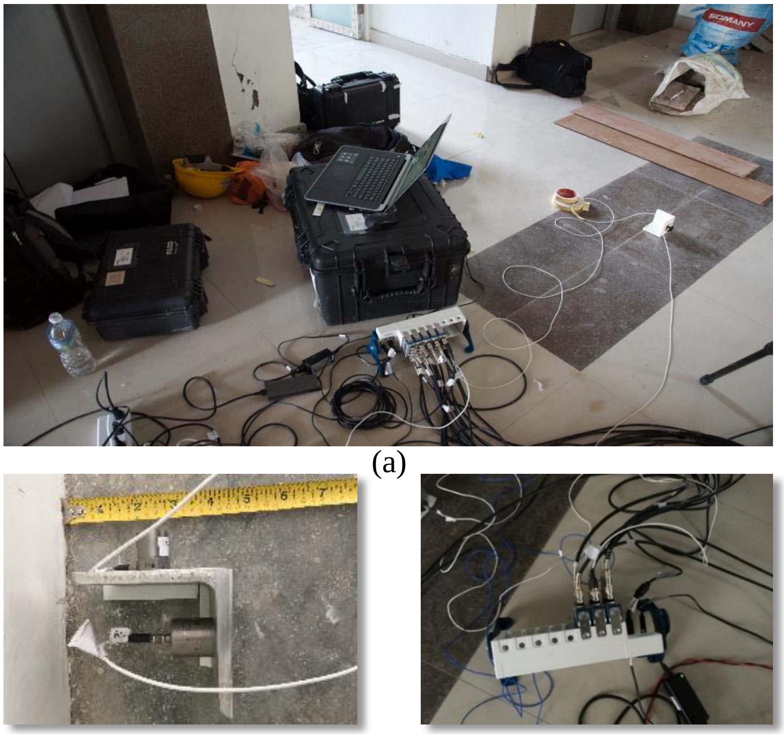

(a)

(b) (c)

Figure 3.9: Example of the instruments that used to collect the ambient vibration data: (a) laptop and cables, (b) data acquisition device or DAQ, and (c) accelerometer sensor.

Table 3.1: Identified pre-earthquake frequencies for Nyatapola temple using SSI method conducted by Jaishi et al. 2003.

Mode No.	SSI Frequencies (Hz)
First bending (N–S)	1.677
First bending (E–W)	1.739
Second bending (E–W)	3.872
Second bending (N–S)	3.890
Third bending (E–W) coupled with torsion	6.358
Third bending (N–S) coupled with torsion	6.194

3.4 Damage Characterization Following the 2015 Gorka Earthquake Sequence

During Gorkha earthquake and the aftershocks that followed, thousands of structures were devastated across numerous regions of the country. This is in addition to destroyed and heavily damaged cultural heritage sites creating both large economic and cultural losses. According to one report, the earthquake resulted in large-scale destruction in Nepal illustrated by 202,157 completely collapse structures, while 214,202 structures had moderate damage. Furthermore, this accounted for 10.95% of residential construction in the Kathmandu Valley (Nepal Disaster Risk Reduction Portal 2016). While the residential impacts of this earthquake were pronounced, various cultural heritages sites also suffered irreplaceable damage and collapse (Brando et al. 2015) as shown in Figure 3.10.

Despite numerous collapses in pagaoda temples, the Nyatapola temple remained upright, but with large observed cracks up to 20 mm wide. Example views of this temple are illustrated in Figure 3.11. One study by Wood et al. (2017b) utilized both ambient vibrations and 3D ground-based lidar for the damage assessment. The authors found that Nyatapola temple sustained a significant shear crack at the base level just above the plinth with maximum width of 3 cm above on the north wall as demonstrated in Figure 1.2. Another crack of 81 cm in length was found in the east wall. Using the identified crack patterns, the damage was the most intense in the north wall and in decreasing values in the east, west, and then the south.

Wood et al. (2017a) also collected ambient vibration data using 12 piezoelectric accelerometers in three different setups. The accelerometers were installed at the center of the overhanging roofs edge at each floor level by climbers, since the authors were unauthorized to enter the temple for historical and religious reasons. The first setup was placed at levels 6, 5, and the base, and the second setup was placed at levels 4, 3, and the base. Finally, the third setup was placed at levels 2, 1, and the base. The base level served as the reference and the data collection was approximately 72 minutes. Ten sensors are employed to estimate frequencies due to several faulty sensors which are a result of cable quality, sensor attachments, and faulty instrumentation. Table 3.2 summarized the first four modes of post-earthquake using stochastic subspace identification (SSI) method. The results showed that modes one and two are translational in N-S and E-W directions, respectively. Modes 3 and 4 are torsional about the Z-axis. From the pre-earthquake fundamental frequency of 1.677 Hz, a frequency shortening of nearly 11% was observed and exhibited on the structure as large shear cracks at the first level above the plinth (Wood et al. 2017b).

Table 3.2: Identified post-earthquake frequencies for Nyatapola temple using SSI method conducted by (Wood et al. 2017b).

Mode No.	Directions	SSI Frequencies (Hz)
Mode 1	Bending (N-S)	1.507
Mode 2	Bending (E-W)	1.524
Mode 3	Torsional around Z axis	2.554
Mode 4	Torsional around Z axis	3.262

Figure 3.10: Examples of the cultural heritage sites in Kathmandu and Patan Durbar Squares destroyed by Gorkha earthquake, 2015 (Nepal Current News 2015)

3.5 Summary

In this chapter, the characteristics of pagoda temples were summarized with the overview of the key structural elements. In pagoda style temples, construction commonly includes thick dual wythe masonry walls with mud mortar, heavy roof systems on each level, timber connecting elements, and a tiered plinth foundation. Due to the material and construction style, these structures are vulnerable to seismic loads. When reviewing the dynamic properties of the pre-earthquake (Jaishi et al. 2003) and the post-earthquake (Wood et al. 2017b) ambient vibration analysis, a frequency decrease of 11% was observed in the fundamental mode. Following the 2015 event, the substantial level of damage observed is evident through cracking in the mud-mortar masonry walls.

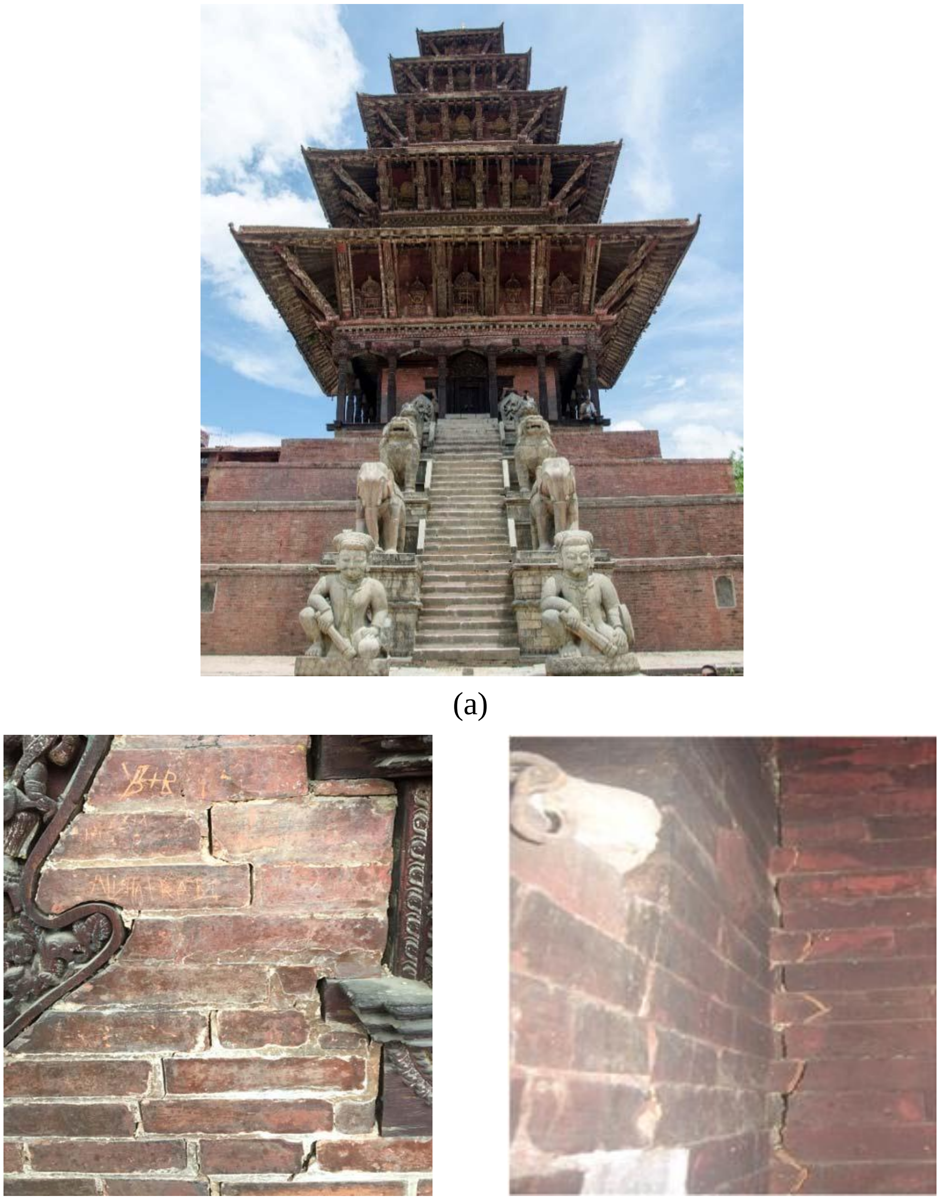

(a)

(b)

(c)

Figure 3.11: View of the Nytapola Temple: (a) the southern entrance of the temple, (b) north wall cracks from outside, and (c) shear wall cracks from inside (Wood et al. 2017a).

CHAPTER 4: MODEL DEVELOPMENT

4.1 Introduction

Structural investigation to explore the dynamic response, damage assessment, and potential retrofitting measures for unreinforced masonry (URM) structures is of interest in the engineering community to minimize losses. This is further exacerbated for UNESCO world heritage sites, which are sites of irreplaceable cultural, society, and religious value. These structures provide a unique challenge in understanding their dynamic behavior due to heterogeneous materials and construction styles, variety and complexities of architecture, lack of calibrated analytical model idealizations, and the difficulty in interpreting limited experimental data. In this work, the focus is on the complex architecture of Pagoda style temples in Nepal. The recent Gorkha earthquake has exposed the vulnerability and diverse dynamic behavior of these historical temples, which are constructed from unreinforced earthen masonry and heavy timber elements. Various numerical modeling techniques along with experimental data for model calibration are available in the literature to gain further insights into the complex behavior and dynamic response of the structures with Pagoda style unique architectures. Previous studies utilizing numerical models have further extended the investigations for the understanding of various parameters on the structural response under various loads, in particular the seismic loading for this work.

Among the available numerical modeling techniques, finite element modeling (FEM) is mostly preferred by research community for its versatility and ease in idealizing structures complexities using the modern day computational resources. Structural systems can be idealized in three-dimensions (3D), as they exist with simulation of every critical element in the model. This study investigated the dynamic behavior of the Nyatapola temple, a five-story pagoda style URM construction. Following the 2015 Gorkha earthquake, this temple was heavily damaged in terms of shear cracks, but did not collapse. Remote sensing data collection, using light detection and ranging (lidar), was collected and this data can mined for the geometry of this structure. The extracted geometry is used to construct finite element models in both the pre- and post-earthquake conditions. The numerical models are then updated and calibrated based on ambient vibration test results (Jaishi et al. 2003; Wood et al. 2017b), as well as confirmed through a visual damage assessment. This chapter outlines the FE model generation using lidar data in the SAP2000 platform (SAP2000, v19.1). Details include the selection of element types, material parameters (strength, elastic moduli, etc.), mass estimation, calibration for pre- and post-earthquake experimental data, and the eigenvalue analysis to extract dynamic characteristics (frequencies and mode shapes). Furthermore, values of the Modal Assurance Criteria (MAC) are used to assess any changes in the pre- and post-earthquake mode shapes to assess the severity of damage caused by earthquake loading.

4.2 Lidar Measurements for Structural Dimensions

Light Detection and Ranging (lidar), also known as laser scanning, is a remote sensing method that uses active light pulses or waveforms to collect accurate measurements of the object in interest. Lidar is an established method for collecting highly precise and geometric data, which is useful in engineering applications. Ground-based lidar (GBL) scanners measure distances and angles to points representing the surface of surrounding objects. The data obtained from a lidar scanner is a point cloud which is a set of data points in a three-dimensional space (x, y, and z). Lidar can be considered as a forensic investigation platform using to identify the accurate dimensions (of the current or as-built conditions), deformations and damage in the real-word structures. Lidar point clouds are known to be extremely high-resolution (sub-centimeter) and highly accurate (millimeter level) data sets. However, lidar does limitations due to the line-of-sight technology resulting in occlusion and gaps in the data as well as file sizes that can be very large that limit their interpretation and process (Chang et al. 2012; Geoservices Maritime Pvt Ltd 2013; Yu et al. 2017). In this work, the primary aim of using the point cloud data is to obtain precise dimensions with high-fidelity for the Nyatapola temple. This will allow for an enhancement of the structural geometry within the FEM, which has a significant impact on the dynamic structural behavior, particularly for torsion (Song et al. 2017). These measurements can be collected at a safe distance, since the authors did not have direct access to the structure (Wood et al. 2017a).

4.2.1 Lidar Data Collection

On June 26, 2015 a field survey was led by researchers from the University of Nebraska-Lincoln and Oregon State University at the Nyatapola temple site. The team utilized two lidar scanners to generate 38 ground-based lidar scans for Nyatapola temple namely; Faro Focus3D X130 and a Riegl VZ-400. Twenty-five scans were scanned by Faro platform (Faro 2014) to collect detailed data on the tiered support structure and at the ground level of the temple. In addition, 13 scans were conducted using the Riegl platform for the longer-range scans (Riegl 2014), to obtain the accurate details of the temple structure at higher floor levels. The collected GBL data had a sub-millimeter resolution as reported by Wood et al. (2017a). Figure 4.1 shows the two lidar scan installed at the Nyatapola site and its plaza south of the front entrance during the field survey of this temple.

(a) (b)

Figure 4.1: Lidar scanning at Nyatapola Temple: (a) Faro Focus^{3D} X 130 and (b) Riegl VZ-400 laser scanners (Wood et al. 2017a).

4.2.2 Lidar Data Processing

4.2.2.1 Point Cloud Segmentation

The point cloud was segmented as shown in Figure 4.2, using the point cloud as described in Wood et al. (2017b). Six horizontal (both internal and external) slices were taken in XY-plane with a thickness of 0.5 m at various intervals along Z-axis to determine the wall thickness for each floor. Likewise, two orthogonal slices at the middle of the temple with a thickness of 0.5 m were taken in the XZ and YZ planes to determine the level heights. For the roof overhangs, five horizontal segments were taken -in XY-plane with various thicknesses due to the variation of the roof height. The elevation view of Nyatapola temple displays the location of the point cloud segments shown in Figures 4.3 and 4.4. These horizontal and vertical point cloud segments have been imported into the AutoCAD software to determine accurate in-situ measurements for the finite element model. Figures 4.6, 4.7, and 4.8 demonstrate the Nyatapola's dimensions for the interior and exterior cross-sections as well side the view elevation section in the (YZ) direction, roof cross-section, and columns cross-section respectively. All dimensions were accurately estimated from point clouds with a relative error of sub-centimeter to the 1 cm level.

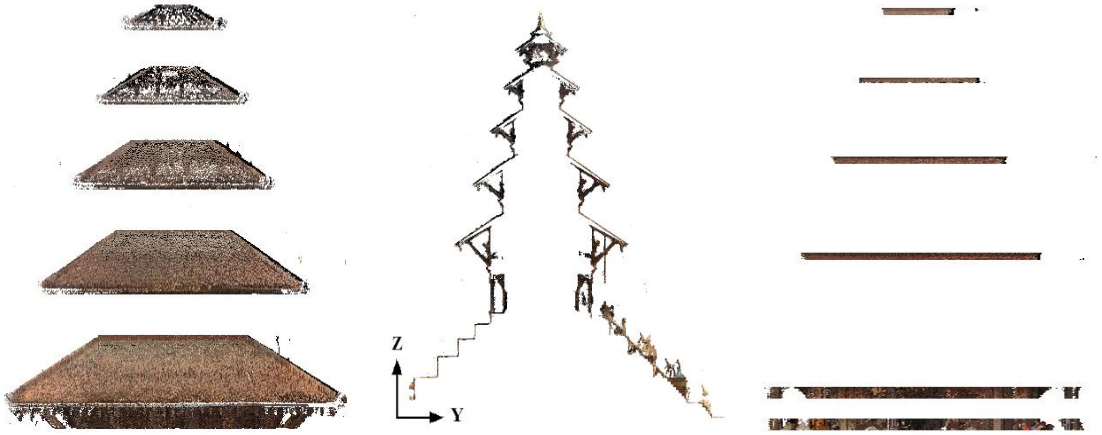

(a) (b) (c)

Figure 4.2: Point cloud segments: (a) roofs, (b) section cut in the (YZ) direction, and (c) floors.

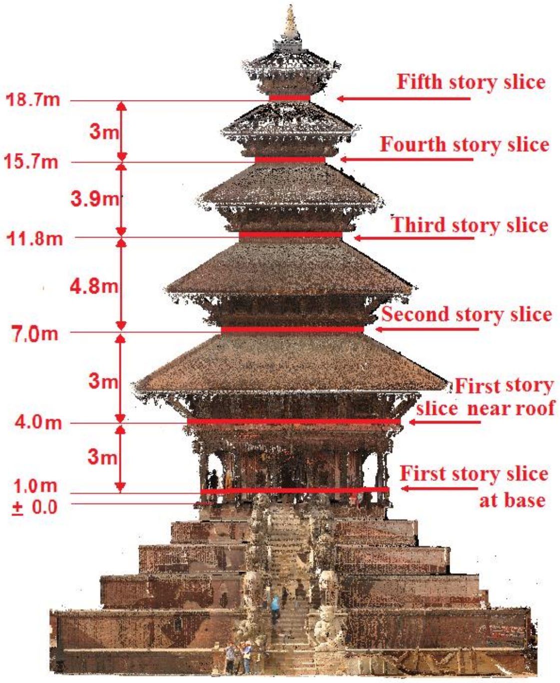

Figure 4.3: Elevation view highlight location of the point cloud slices for floor sections.

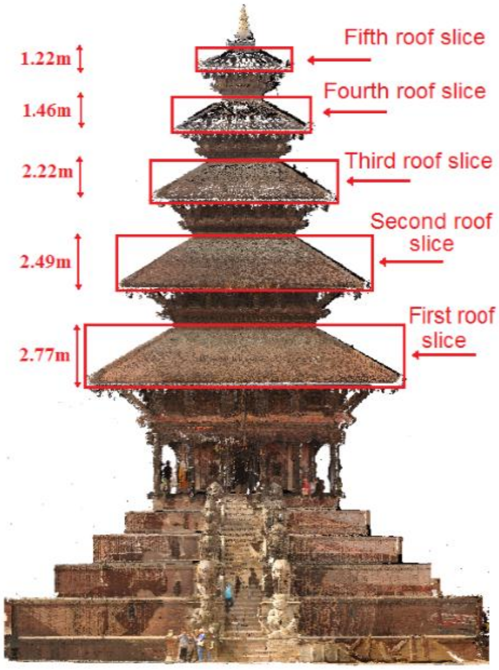

Figure 4.4: Elevation view highlight location and thickness of the point cloud slices for roof sections.

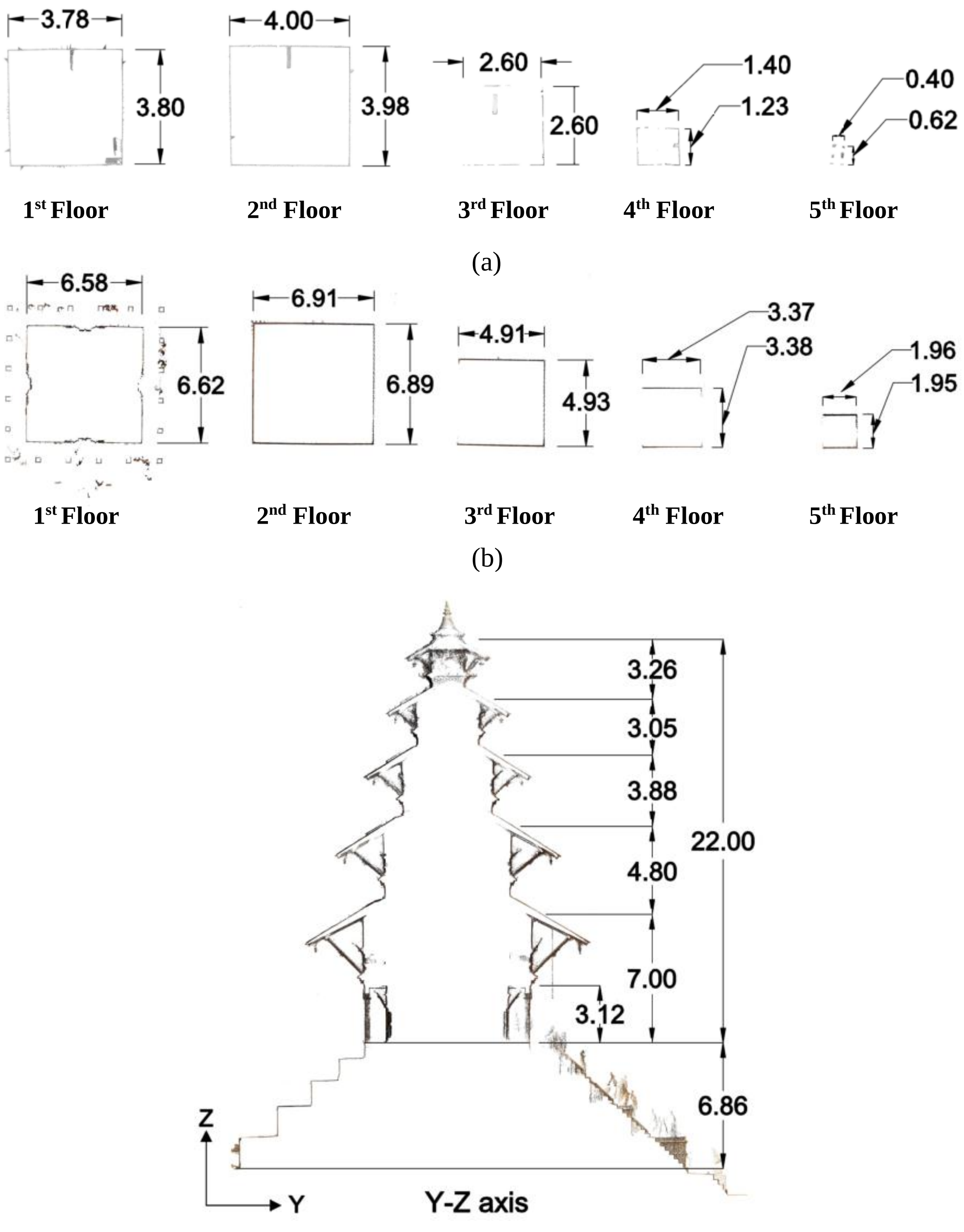

(c)

Figure 4.5: AutoCAD dimensions of Nyatapola Temple: (a) interior cross-sections in the XY plane, (b) exterior cross-sections in the XY plane, and (c) elevation view showing sections in the YZ plane. Note all dimensions are in meters.

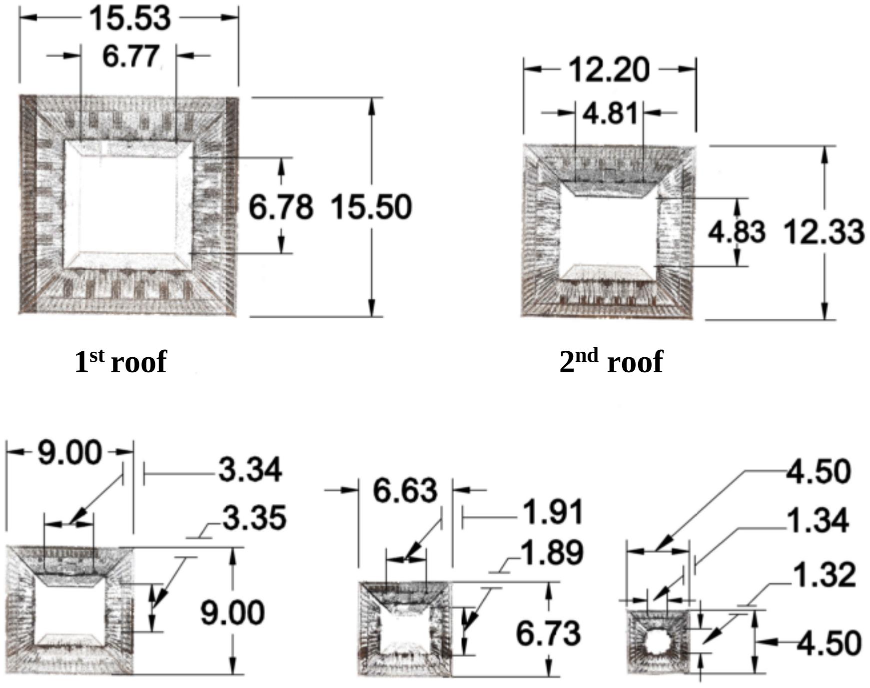

1st roof 2nd roof

3rd roof 4th roof 5th roof

Figure 4.6: Cross-sections dimensions of Nyatapola roof in meters.

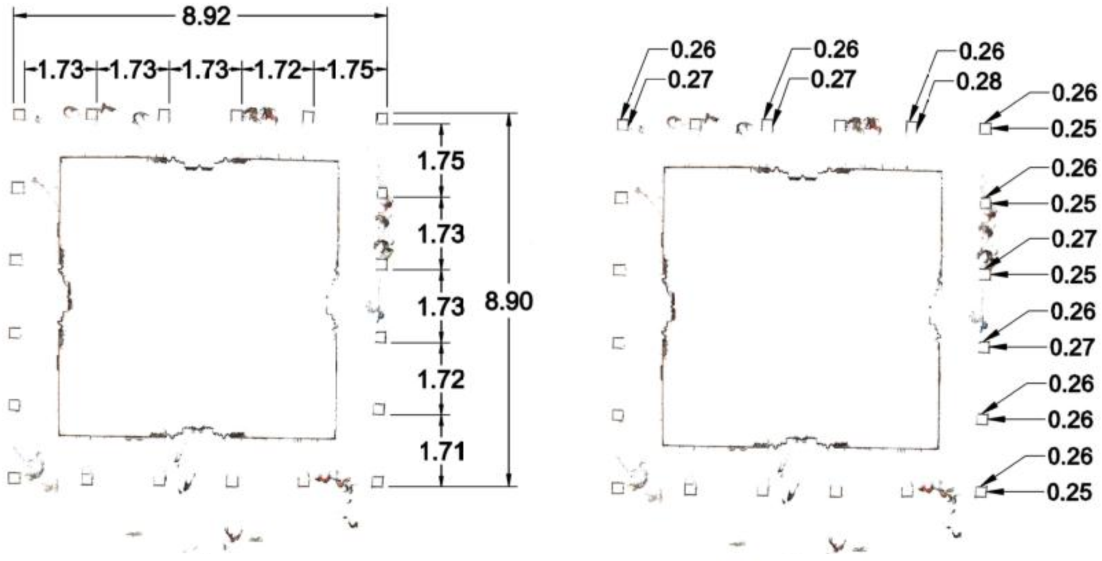

(a) (b)

Figure 4.7: Columns of Nyatapola Temple: (a) columns spacing and (b) columns cross-section dimensions. Note all dimensions are in meters.

4.3 Nyatapola Finite Element Dimensions

After obtaining the actual geometrical measurements of the temple, these dimensions were used to create an initial FEM. Tables 4.1 and 4.2, respectively, illustrated the external and internal masonry core dimensions of the temple for both measured dimensions and FEM dimensions. Due to the non-symmetric nature of the temple, the dimensions closely follow that of the point cloud, but with some minor tweaks that are required for the finite element mesh. The percentage error between the point cloud and the finite element model was calculated using the following equation:

$$\text{Error } \% = \left| \frac{D_{Point\ Cloud} - D_{FEM}}{D_{Point\ Cloud}} \right| \times 100 \tag{4-1}$$

Where $D_{\text{Point Cloud}}$ = dimensions extracted from point cloud and D_{FEM} = dimensions of FEM. The thickness of the temple walls was determined by subtracting the internal dimensions from the external dimensions, as shown in Table 4.3. The cross-section dimensions of the columns are not constant due to the typical construction practices. This is shown in Figure 4.7 and the average cross-sections were used when generating the FEM as presented in Table 4.4. The measured dimensions and the generated FEM dimensions found in Tables 4.1, 4.2, and 4.3 are closely aligned with a maximum percent error less than 1%. Recall this is due to the slight variations for a uniform mesh generation. The measured roof dimensions are presented in Table 4.5, which are used to calculate the mass of the overhanging roofs levels**.** These mass values will be incorporated as lumped mass since they are considered herein as nonstructural components. More details on this are presented section 4.5. For completeness, the level heights and nomenclature used for each floor level are illustrated in Figure 4.8. A typical FEM cross-section floor of Nyatapola temple is demonstrated in Figure 4.9.

Table 4.1: External dimensions of masonry wall elements.

Level	Height (m)	Measured External Masonry Dimensions (m)		FEM External Masonry Dimensions (m)		Percent Error (%)	
		w_x	w_y	w_x	w_y	w_x	w_y
1a	3.12	6.58	6.62	6.60	6.60	0.30	0.30
1b	3.88	9.10	9.10	9.10	9.10	0.00	0.00
2	4.80	6.91	6.89	6.90	6.90	0.10	0.10
3	3.88	4.91	4.93	4.92	4.92	0.20	0.20
4	3.05	3.37	3.38	3.40	3.40	0.90	0.60
5	3.26	1.96	1.95	1.96	1.96	0.00	0.50

Table 4.2: Internal dimensions of masonry wall elements.

Level	Height (m)	Measured Internal Masonry Dimensions (m)		FEM Internal Masonry Dimensions (m)		Percent Error (%)	
		w_x	w_y	w_x	w_y	w_x	w_y
1a	3.12	3.78	3.80	3.80	3.80	0.50	0.00
1b	3.88	3.78	3.80	3.80	3.80	0.50	0.00
2	4.80	4.00	3.98	4.00	4.00	0.00	0.50
3	3.88	2.60	2.60	2.60	2.60	0.00	0.00
4	3.05	1.40	1.23	1.40	1.22	0.00	0.80
5	3.26	0.40	0.62	0.40	0.62	0.00	0.00

Table 4.3: Wall thickness of masonry wall elements.

Level	Height (m)	Measured Masonry Wall Thickness (m)		FEM Masonry Wall Thickness (m)		Percent Error (%)	
		w_x	w_y	w_x	w_y	w_x	w_y
1a	3.12	1.40	1.41	1.40	1.40	0.00	0.70
1b	3.88	2.66	2.65	2.65	2.65	0.40	0.00
2	4.80	1.45	1.45	1.45	1.45	0.00	0.00
3	3.88	1.16	1.17	1.16	1.16	0.00	0.90
4	3.05	0.99	1.08	1.00	1.09	0.10	0.90
5	3.26	0.78	0.67	0.78	0.67	0.00	0.00

Table 4.4: Beam and column frame elements dimensions.

Member	Cross-section Dimensions (m. × m.)	Material
Column	0.26 × 0.26	Timber
Beam	0.1 × 0.26	Timber

Table 4.5: Dimensions of the roof elements.

Roof Level	Vertical Height (m)	Bottom Roof Dimension (m)		Top Roof Dimension (m)	
		w_x	w_y	w_x	w_y
1	2.77	15.45	15.50	6.77	6.78
2	2.49	12.20	12.33	4.81	4.83
3	2.22	9.00	9.00	3.34	3.35
4	1.46	6.68	6.73	1.91	1.89
5	1.22	4.50	4.50	1.34	1.32

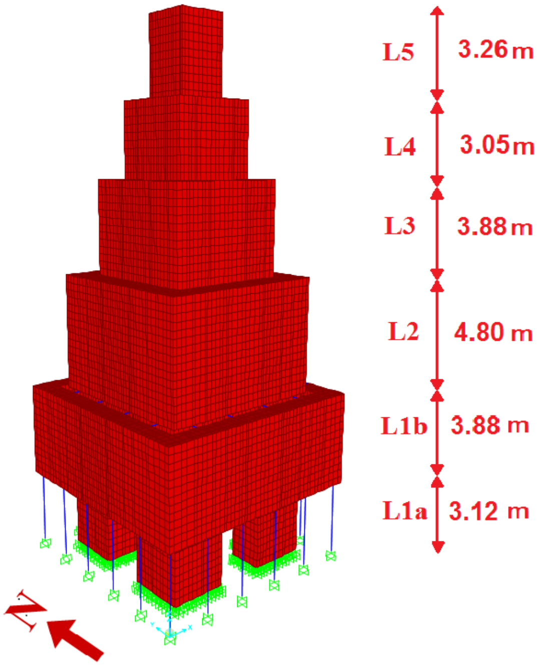

Figure 4.8: Elevation dimensions of Nyatapola FE model with floor level nomenclature (L).

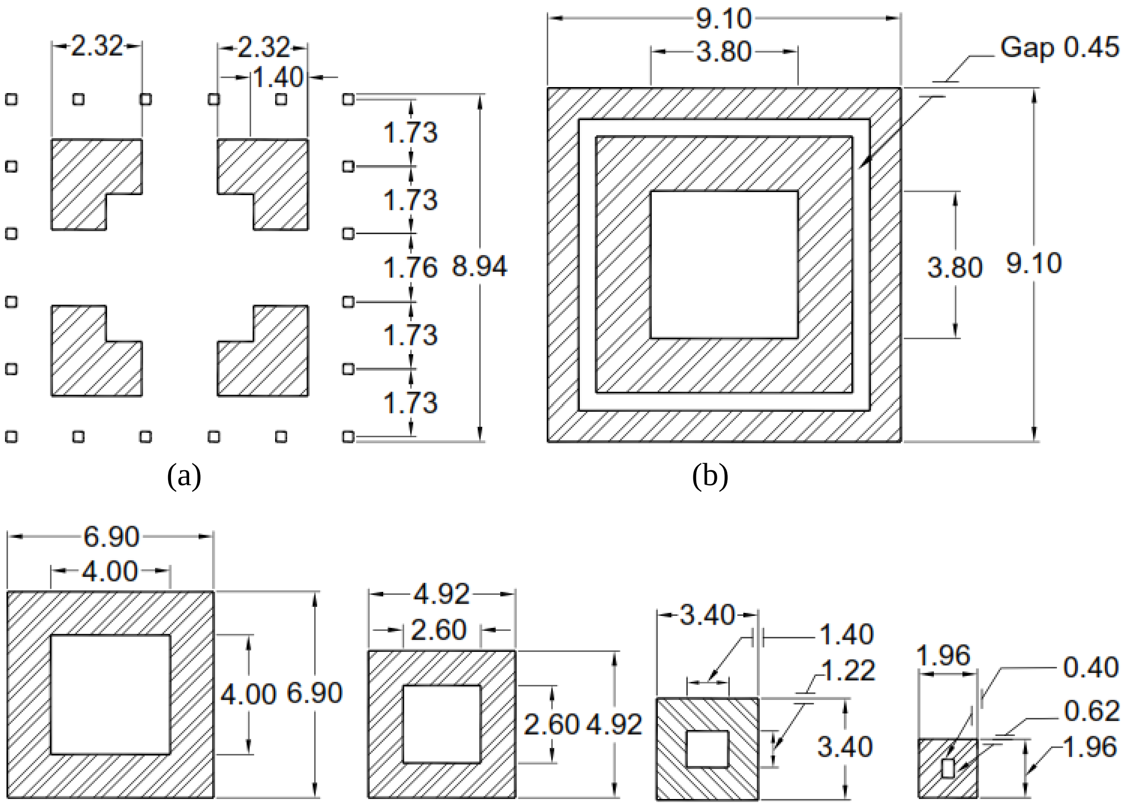

(a) (b)

(c) (d) (e) (f)

Figure 4.9: Typical FEM cross-section floor of Nyatapola temple, all dimensions in (m): (a) first floor at base [L1a], (b) first floor at 3.12 m [L1b], (c) second floor [L2], (d) third floor [L3], (e) fourth floor [L4], and (f) fifth floor [L5].

4.4 Finite Element Modeling

The selected finite element (FE) platform is SAP2000 v19.1. The FE model closely represents the geometry as extracted by the lidar scans. This geometry is critical to account for the non-rectangular nature of the temple that may lead to potential torsion in the response. Once the model is created, validation with the operational modal analysis is a key step for a representative and calibrated structural model. A comprehensive description of the FE modeling approach is first provided, followed by procedure to create solid FE model with known geometry, element discretization schemes, modal/material parameters, boundary conditions, and dead loads. Figure 4.10 shows the flowchart of the FEM process used in this study, which outline the key steps for creating the initial FE model of the temple within general commercial FEM packages. Numerous manual iterations have been done to update parameters for its modal properties (Kodikara et al. 2016). This is performed using an eigenvalue analysis and evaluate the results in an iterative approach such that the fundamental frequency is within 1% between the measured operational modal analysis and corresponding FE fundamental mode.

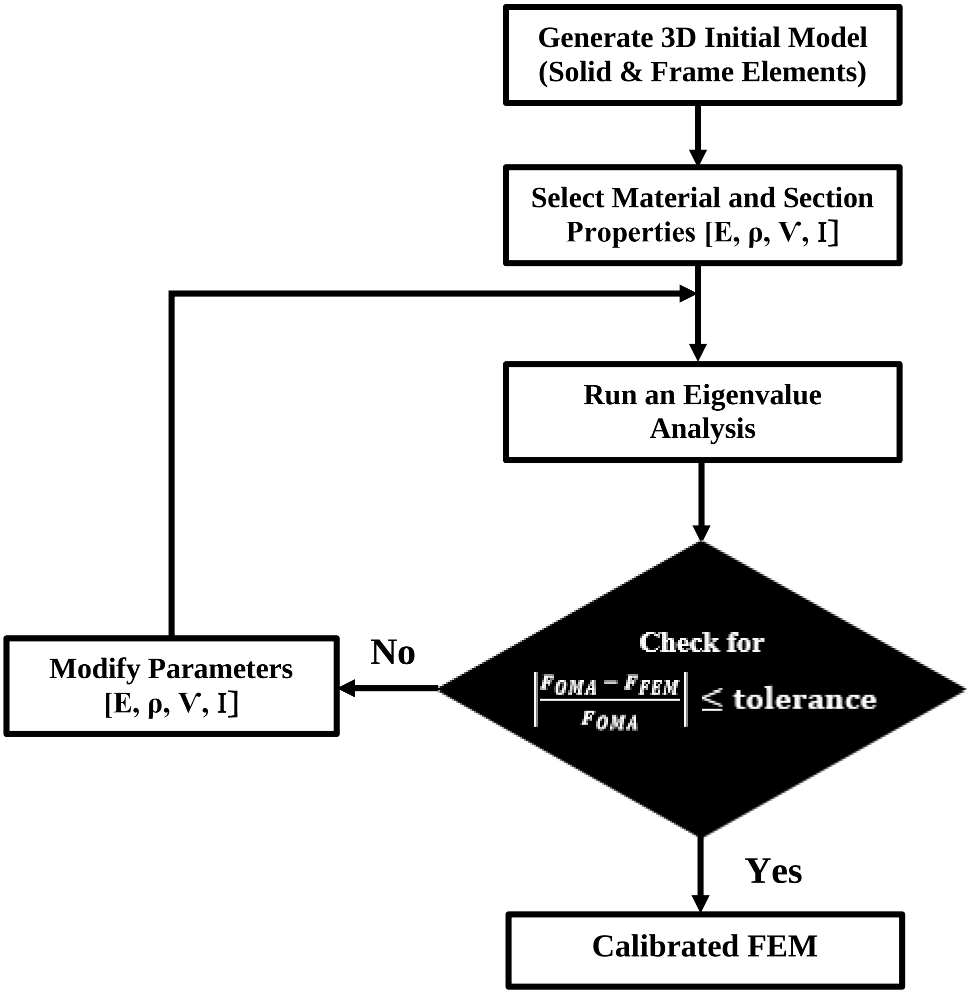

Figure 4.10: General flowchart of FEM processes.

4.4.1 Model Properties

A linear elastic three-dimensional (3D) FEM was implemented using a macro-modeling approach since it is applicable when the structure is composed of solid walls with sufficiently large dimensions. This is due to the uniformly anticipated stresses at macro-scale (Lourenco 2002). The reasons behind using the linear elastic model are being a conservative for force demands as well as the lack of knowledge of material properties in the nonlinear range. The load-bearing walls and the heavy timber beams and columns are considered as main structural elements (stiffness contributions), while the timber struts and roof systems are considered nonstructural elements (only their mass was considered in the analysis). Doors, windows, and other openings were neglected in this analysis. The temple is assumed to be rigidly connected at its base. The structure is divided into elements and nodes, while accounting for the variation in wall thickness and height. The beams and columns are considered as line elements, while the masonry walls are considered as 3D solid elements. The lumped mass is represented using a zero-D element, which applied only to the nodes. Figure 4.11 shows the typical element types and dimensionality used in generating the FE model.

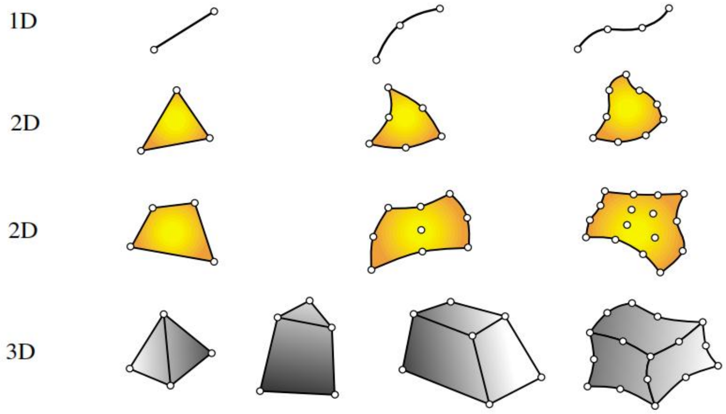

Figure 4.11: Types of finite element geometries which are represented 1, 2, and 3-dimensional space (Boeraeve 2010).

The boundary conditions are applied at the joints to provide rigidity where each brick has eight nodes located at corners and each node has its respective three degrees of freedom. Each floor level is considered as a rigid component due to the heavy roof system that concentered on the floor. This accounts for a rigid-diaphragm assumption. The base over plinth of the temple is considered rigid when neglecting any soil-structure interaction and dynamic response of multi-tier plinth. This is due to the lack of information and the unknown internal structure of the plinth (Shakya et al. 2014). Soil-structure interaction effects may not be negligible, and the response of the soil was large as may be characterized by nonlinear behavior due to yielding of near surface sediments (Rajaure et al. 2017). The 3D FE model of Nyatapola temple consists of 47,708 solid elements, 52 frame elements (32 beams and 20 column), and 58,760 nodes. The maximum and minimum mesh grid for the solid elements varies from 0.23 × 0.317 × 0.298 m (in X, Y, and Z) to 0.1 × 0.1 × 0.298 m, respectively. In addition, the total mass of FEM is 13,716 kN. Figure 4.12 illustrates the model connectivity.

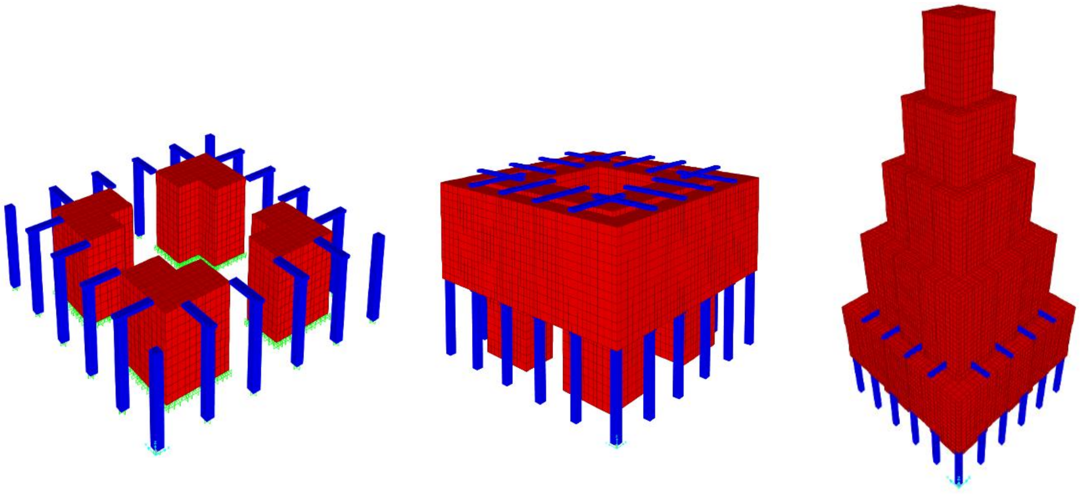

(a) (b) (c)

Figure 4.12: FEM model assembly: (a) level 1a, (b) level 1a and level 1b, and (c) rigid diaphragm constraint.

4.4.2 Model Parameters

Material parameter selection is critical for generating finite element models to represent the complex component interactions in real structural system. These parameters have direct influence on the generated model to establish an agreement between numerical and experimental results. The selected model parameters for this study include: Young's Modulus (E), mass density (ρ), Poisson's ratio (v), and the moment of inertia (I).

The initial FEM was calibrated to represent the pre-earthquake condition in accordance with the ambient vibration studies by Jaishi et al. (2003). To tune the initial model for the pre-earthquake fundamental frequency, the Young's Modulus for the masonry elements was iterated to reach a value of 485 MPa. This value falls within the range of values suggested in the literature (Jaishi et al. 2003; Shakya et al. 2014). The specific weight of the timber is set to 9 kN/m^3, while a value between 18 and 20 kN/m^3 is selected for the masonry walls. The masonry walls are considered variable as a result of the traditional construction process and the collapse and subsequent reconstruction of the upper level of Nyatapola Temple after the 1934 Bihar earthquake (Shakya et al. 2014). Furthermore, the behavior of the masonry walls is influenced by unknown internal factors including interior voids, the variation of the brick and joint dimension, spreading bricks, and mortar bed joints. The quality of craftsmanship also contributes to the variability in the specific weight of the masonry (Parajuli et al. 2010). Other assumed material properties included the values assigned to the Poisson's ratios of 0.25 and 0.12 for masonry and timber materials, respectively, based on engineering judgment as guided by the literature survey.

The linear model updating of post-earthquake FEM was guided by the cracks detected in the point cloud analysis and visual damage assessment. The Young's Modulus value for the masonry elements was reduced according to observed significant cracks at the first floor as well with increasing levels to reach a maximum value of 25% on the upper floor. The dimensions of the structural frame as well as the material properties of masonry elements and timber frame which used in the generating and updating pre and post-earthquake FEM are summarized in Tables 4.6 and 4.7.

Table 4.6: Materials properties of masonry and support frame (Jaishi et al. 2003; Shakya et al. 2014).

Material	Specific Weight (kN/m^3)	Young's modulus (MPa)	Poisson's ratio
Masonry	18 - 20	E = 280 - 485	ν = 0.25
Timber	9	E = 12500	ν = 0.12

Table 4.7: Masonry material properties for pre- and post-earthquake.

Level No.	Specific Weight (kN/m^3)	Young's Modulus Pre-Earthquake FEM (MPa)	Young's Modulus Post-Earthquake FEM (MPa)	Reduction in Young's Modulus (%)
5	18	400	300	25.0
4	18	400	310	22.5
3	18	400	315	21.3
2	18	400	320	20.0
1b	20	485	330	17.5
1a				
North	20	400	280	30.0
East	20	485	475	2.0
West	20	485	465	4.1
South	20	485	485	0.0

4.5 Load Cases

4.5.1 Dead Load

The dead load of the model consists of the self-weight of all primary structural elements, which includes the walls, columns, and beams of the structural frame. These values were calculated within SAP2000 based on the cross-sectional geometry and material density of each element. These specific values are shown in Tables 4.4, 4.6 and 4.7. The total self-weight of Nyatapola temple FEM is 1,038,479 kg (10,184 kN).

4.5.2 Roof Load

The roof load of the model includes the self-weight of nonstructural components including the timber, roof beams, purlins, roof tile, and mud mortar. The roof load is applied as the concentrated load on each node that corresponds to a floor level as a lumped mass**.** The roof's weight calculation was done based on the measured roof dimensions extracted from point cloud data as presented in Table 4.5 and Figure 4.6. The total weight of the roof is 360,164 kg (3,532 kN) as summarized in Table 4.8. Some assumptions were considered for the roof's weight calculations as recommended in previous literature (Jaishi et al. 2003; Nienhuys 2003). The specific weights assumed were 8 kN/m^3 and 20 kN/m^3 for timber and clay, respectively. The thickness of the timber roof, inclined timber, and clay roof tiles assumed were 30 cm, 20 cm, 15 cm, respectively.

Table 4.8: Roof weight calculations.

Roof No.	Weight (kN)
Pinnacle	133
5	139
4	316
3	541
2	970
1	1433
Total weight	3532

4.6 Pre-Earthquake Model

To calibrate the initial FEM for the pre-earthquake condition, the workflow presented in section 4 is followed. Numerous iterations were required to match the fundamental frequency closely of pre-earthquake FEM with pre-earthquake OMA (conducted by Jaishi et al. 2003), based on updating model parameters. As a result, the dynamic properties of natural frequencies and mode shapes were obtained, and MAC values were determined.

The Table 4.9 shows the pre-earthquake frequency results of OMA and FEM for the first six modes as well the percentage of error. The first four mode shapes of pre-earthquake FEM are seen in Figure 4.14. The first, second and fourth modes are bent in the direction of (N-S), (E-W) and (E-W), respectively while the third mode represented is torsional about the Z-axis.

Through a quick investigation of the results, the established model displays a high correlation with the operational model. The maximum percentage of error between OMA frequencies and FEM frequencies for the first four identified natural modes as shown in Table 4.9 and Figure 4.13 is less than 2.5%. The percentage error calculation was done using the following expression:

$$\text{Error}\ \% = \left|\frac{F_{OMA}-F_{OMA}}{F_{OMA}}\right| \times 100 \tag{4-2}$$

Where F_{OMA} = OMA frequency and F_{FEM} = FEM frequency. Mode 3 is not captured in the pre-earthquake system identification, which may be due to the excitation of the temple under non-broadband white noise conditions or an oversight in the identification process. Despite this, this third mode was identified in the post-earthquake OMA process.

The identified percent error is quite low and was accomplished by manual iterations of the FEM calibration.

Table 4.9: Pre-earthquake frequencies of OMA and FEM.

	Pre-earthquake OMA Frequencies		Pre-earthquake FEM Frequencies		Difference freq. %
	Frequency (Hz)	Direction	Frequency (Hz)	Direction	
Mode 1	1.68	Bending (N-S)	1.69	Bending (N-S)	0.89
Mode 2	1.74	Bending (E-W)	1.70	Bending (E-W)	2.42
Mode 3	N/A	–	3.02	Torsion around Z	–
Mode 4	3.87	Bending (E-W)	3.96	Bending (E-W)	2.33
Mode 5	3.89	Bending (N-S)	3.98	Bending (N-S)	2.24
Mode 6	6.36	Bending (E-W) with torsion	6.63	Bending (E-W)	4.25

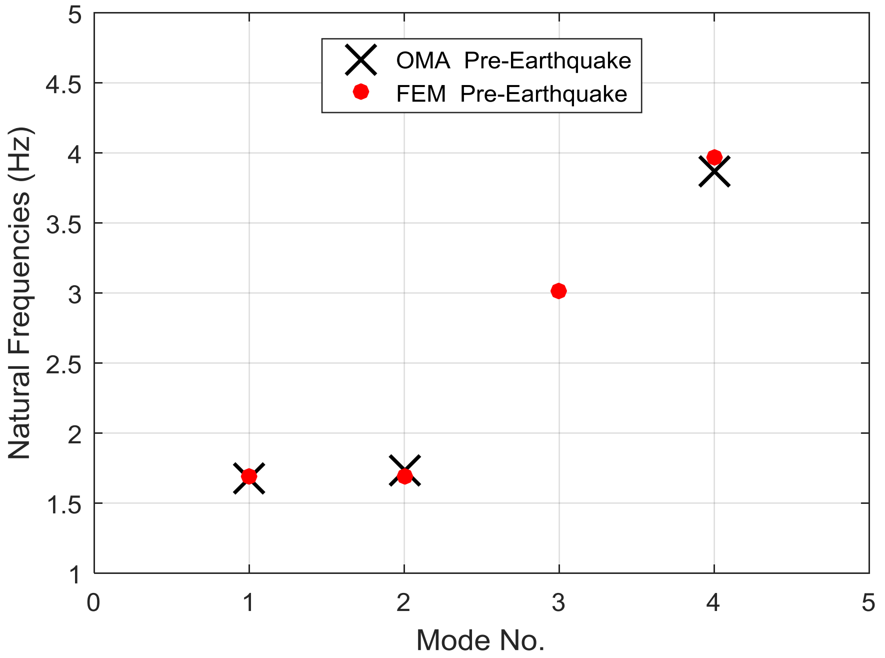

Figure 4.13: Comparison of the first four natural frequencies of OMA and FEM for pre-earthquake. Note mode 3 was not identified in the pre-earthquake system identification.

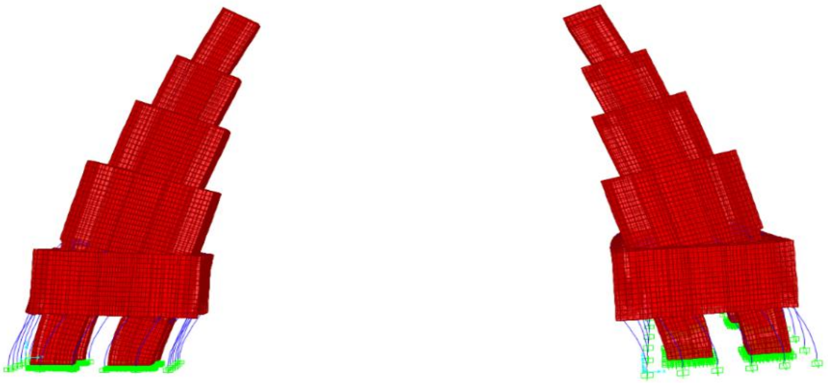

(a) 1st mode
f_{pre}= 1.692 Hz; f_{post}= 1.508 Hz

(b) 2nd mode
f_{pre}= 1.697 Hz; f_{post}= 1.524 Hz

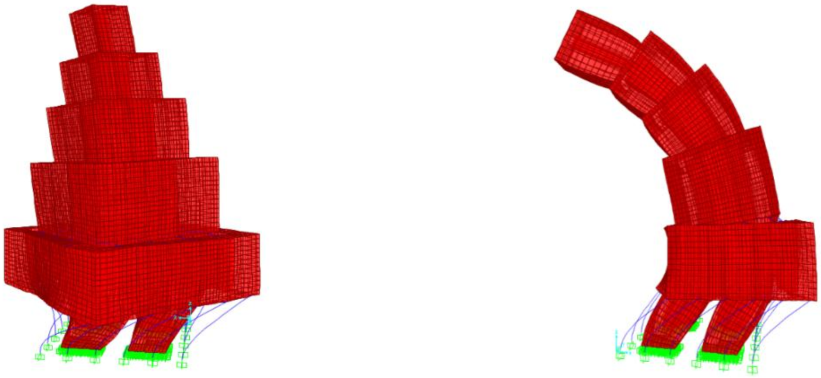

(c) 3rd mode
f_{pre}= 3.020 Hz; f_{post}= 2.720 Hz

(d) 4th mode
f_{pre}= 3.962 Hz; f_{post}= 3.527 Hz

Figure 4.14: Pre and post-earthquake FEM frequencies and mode shapes for the first four modes.

The Modal Assurance Criterion (MAC) is used to determine the similarity of two mode shapes. The degree of correlation of two mode shapes lies between 0 and 1. A value of unity presents that the two mode shapes are consistent. Whereas, a null value indicates no consistency (Pastor et al. 2012). Modal Assurance Criteria was calculated to compare various mode shapes which obtain from FEM by using the following equation:

$$\text{MAC}\,(\emptyset_1, \emptyset_2) = \frac{\left|\emptyset_1{}^{\mathrm{T}}\,\emptyset_2\right|^2}{(\emptyset_1{}^{\mathrm{T}}\,\emptyset_1)(\emptyset_2{}^{\mathrm{T}}\,\emptyset_2)} \tag{4-3}$$

Where $\{\emptyset_{\boldsymbol{n}}\}^{\boldsymbol{T}}$ = complex conjugate and transpose of the nth mode shape. In this study, the computation of MAC values was performed using 58,164 nodes as distributed throughout the temple. Two MAC analysis methods can used to compare the results, namely AutoMAC criterion and crossMAC criterion (Pastor et al. 2012). MAC values for pre-earthquake modes were calculated using AutoMAC criterion analyzes are reported in Table 4.10. The behavior of each mode was independent in comparison to the other modes since the MAC values are near zero. Figure 4.15 represents a 3D bar plot of the MAC values for pre-earthquake FEM. Note a MAC value of unity is achieved during the diagonal since it is comparing identical mode shapes.

Table 4.10: MAC values of pre-earthquake modes.

Mode No.		1	2	3	4
	Frequencies (Hz)	1.692	1.697	3.020	3.977
1	1.692	1.000	0.000	0.000	0.000
2	1.697	0.000	1.000	0.000	0.022
3	3.020	0.000	0.000	1.000	0.000
4	3.977	0.000	0.022	0.000	1.000

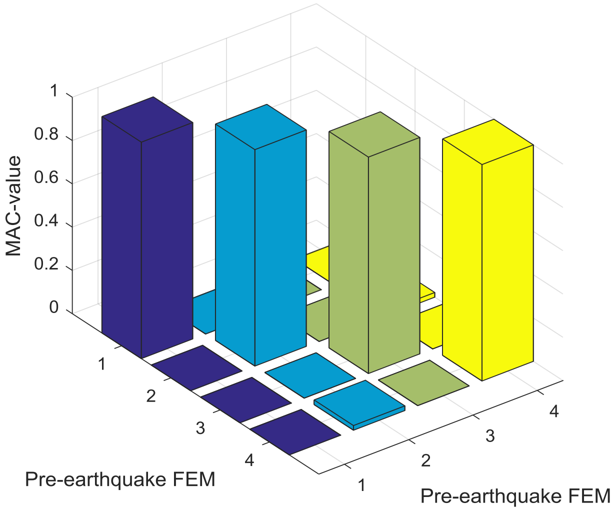

Figure 4.15: 3D plots of MAC values for the first four mode shapes of pre-earthquake.

4.7 Post-Earthquake Model

The post-earthquake FEM model updating was also guided by lidar scans and subsequent data processing, visual damage assessment, and ambient vibration post-earthquake (performed by Wood et al. 2017b). To account for the damaged state of the temple following the 2015 Gorkha and its aftershock sequence, the Young's modulus of post-earthquake was reduced by increasing the height levels of the temple to a maximum value of 25% at fifth level, similar to the work by Aras et al. (2011). This value was greatly reduced at the top level to account for the dislodged state of the bricks and grout loss detected by the GBL analysis of the surface geometry (Wood et al. 2017b). As a result, the post-earthquake dynamic properties in terms of frequencies were identified.

The post-earthquake FEM was calibrated in accordance with the ambient vibration studies by Wood et al. (2017b) to achieve appropriate dynamic properties results. The natural frequencies of FEM and OMA are presented as well as the percentage of error between them in Table 4.11. This frequencies table show that the bending of both first and fifth modes was in north-south direction while the second, fourth and sixth modes bent in the east-west direction. The torsional has clearly appeared in the third mode, which was not identified in the early pre-earthquake system identification of the temple. The first four mode shapes are shown in Figure 4.14. By comparing the dynamic properties results of FEM and OMA for post-earthquake stage in Table 4.11 as well Figure 4.16, the maximum percentage error of the first four natural modes obtained using Equation (4-2) is less than 8.2%, which is less than the general accepted value of 10%. This value of 10% is generally perceived as acceptable for engineering judgment.

The fundamental frequency of the post-earthquake model decreased by 11% compared with the pre-earthquake model illustrating a substantial stiffness reduction due to the observed and quantified structural damage. Akin to the pre-earthquake MAC values, post-earthquake MAC values were done using AutoMAC criterion analysis to produce results of almost zero. These results computed using Equation (4-3) suggests that the modes were independent of each other as listed in Table 4.12 as well Figure 4.17.

Table 4.11: Post-earthquake frequencies of OMA and FEM.

	Post-earthquake OMA Frequencies		Post-earthquake FEM Frequencies		Difference freq. %
	Frequency (Hz)	Direction	Frequency (Hz)	Direction	
Mode 1	1.507	Bending (N-S)	1.508	Bending (N-S)	0.07
Mode 2	1.524	Bending (E-W)	1.524	Bending (E-W)	0.00
Mode 3	2.554	Torsion around Z	2.720	Torsion around Z	6.50
Mode 4	3.262	Torsion around Z	3.527	Bending (E-W)	8.12
Mode 5	N/A	–	3.547	Bending (N-S)	–
Mode 6	N/A	–	5.835	Bending (E-W)	–

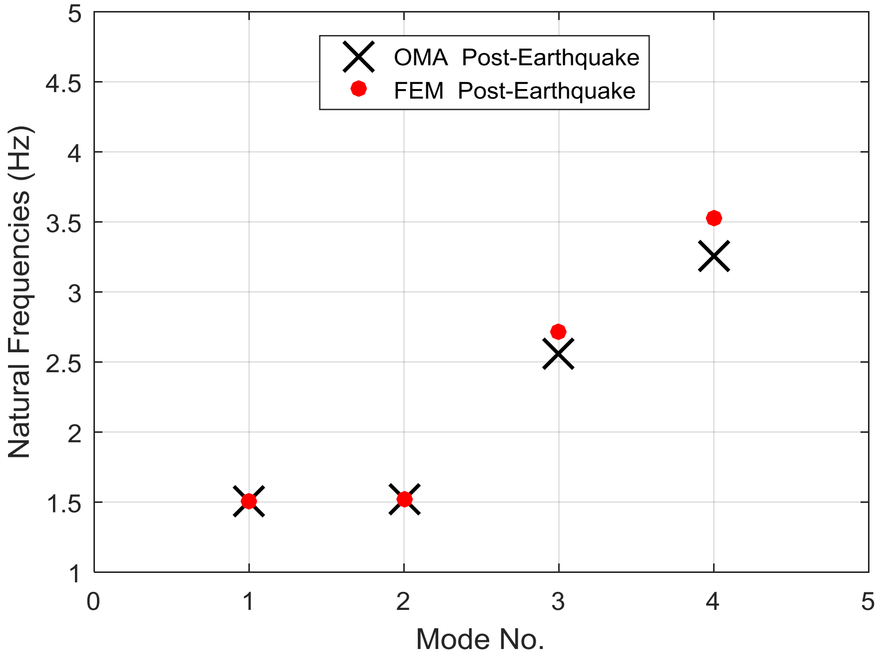

Figure 4.16: Comparison of the first four natural frequencies of OMA and FEM for post-earthquake.

Table 4.12: MAC values of post-earthquake modes.

Mode No.		1	2	3	4
	Frequencies (Hz)	1.508	1.524	3.720	3.527
1	1.508	1.000	0.000	0.000	0.000
2	1.524	0.000	1.000	0.001	0.021
3	3.720	0.000	0.001	1.000	0.001
4	3.527	0.000	0.021	0.001	1.000

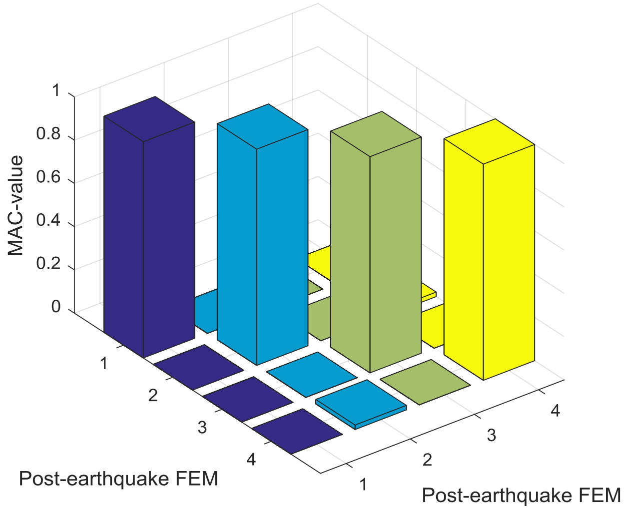

Figure 4.17: 3D plots of MAC values for the first four mode shapes of post-earthquake.

When comparing the pre- and post-earthquake models, a stark difference is noted in the frequencies shown in Table 4.13. A decrease in the fundamental frequency between pre- and post-earthquake state by nearly 11% showed substantial stiffness reduction through cracking in the mud-mortar masonry walls. On the contrary, Figure 4.18 shows a high correlation between pre and post-earthquake FEM for the first four modes. This illustrates that while a stark difference in noted in frequencies, the distribution of mass and stiffness of the finite element model were not pronounced.

Table 4.13: Comparison of frequencies and MAC values of pre-and post-earthquake models for the first four mode shapes.

	Pre-earthquake FEM Frequencies (Hz)	Post-earthquake FEM Frequencies (Hz)	Difference freq. %	MAC
Mode 1	1.69	1.51	10.77	0.9998
Mode 2	1.7	1.52	10.59	0.9995
Mode 3	3.02	2.72	9.94	0.9912
Mode 4	3.96	3.53	10.86	0.9934

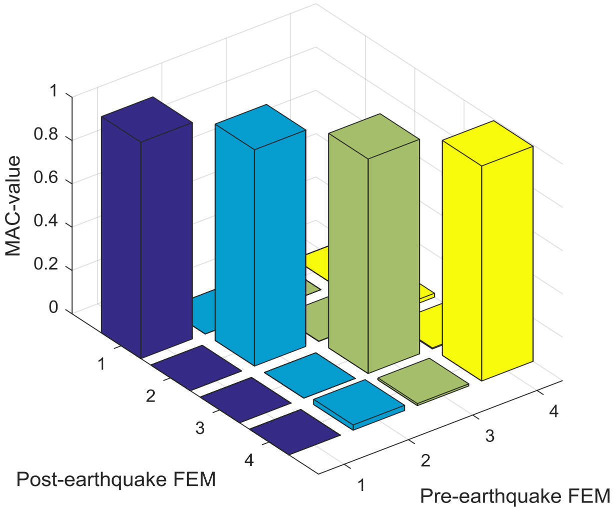

Figure 4.18: 3D plots of MAC values of pre-and post-earthquake for the first four mode shapes.

4.8 Summary

This study numerically modeled the Nyatapola temple using geometric dimensions extracted from lidar data within a 1% error tolerance. Two lidar scanners generated 38 ground-based lidar scans for a sub-centimeter level resolution of the structure (Wood et al. 2017b). The processed point cloud from Wood et al. (2017b) was segmented into horizontal and vertical planes to obtain plan dimensions for different floors (wall dimensions and thicknesses, roof dimensions, etc.) and elevation dimensions, respectively. The extracted dimensions were used to construct 3D FE models in the SAP 2000 platform, incorporating material homogeneity of the structure in pre- and post-earthquake structural conditions. The unreinforced masonry in load-bearing walls was idealized by 8 node solid elements, whereas heavy timber beams and columns were modeled with 2 node frame elements. The timber roof system was simplified as added mass in the model using zero-dimension, single node elements. Fixed base conditions were assumed at the model base, neglecting the interaction of the multi-tiered plinth in actual structure which has not been quantified. Linear-elastic material properties were assumed in the numerical models from literature (Jaishi et al. 2003; Shakya et al. 2014).

The pre-earthquake 3D FE model was calibrated by comparing first six frequencies between analytical model and operational modal analysis (OMA) of ambient vibration data from Jaishi et al. (2003). The refined modulus of elasticity used for brick masonry produced less than 1% error in the fundamental frequency, and at most 2.5% error in frequencies of first four modes. The post-earthquake numerical model, an updated model from the pre-earthquake condition, was developed for further linear time history analysis, using modal updating of modulus of elasticity for various masonry walls. The modulus of elasticity was updated to find a closely representative model in terms of frequencies between the OMA and the model, which was further guided with manual intervention by the point cloud analysis and visual damage assessment. The OMA frequencies were based on ambient vibration data from Wood et al. (2017b). The elastic material properties for timber components were kept consistent between pre- and post-earthquake models, due to no known observed damage.

Finally, modal analysis results (frequencies and mode shapes) were compared from both pre- and post-earthquake numerical models to report the extent of damage in terms of change in dynamic characteristics. Fundamental frequency was quantified as a reduction of 11% in the fundamental mode highlighting a substantial reduction of structural stiffness as an evident damage in the Nyatapola temple.

CHAPTER 5: TIME HISTORY ANALYSES

5.1 Introduction

The time-history analysis provides for linear or nonlinear evaluation of dynamic structural response under time-varying loads. This chapter presents a linear time history analysis of the Nyatapola temple under recorded ground motions from the 2015 Gorkha earthquake, namely its mainshock and the predominate aftershock. The dynamic analysis of the system is necessary to assess forensically the effect of the temple structure's response to earthquake motions. To perform this task, first, the ground motion characteristics are detailed. Next, the ground motions are applied to the temple using linear time history analysis. The results generated include maximum displacement, interstory drift, absolute acceleration, uncorrelated acceleration amplification ratio, and in-structure spectral acceleration response. Furthermore, maximum torsional demand profiles were generated and compared to the lidar results.

5.2 Ground Motion Characteristics

Severe earthquakes have struck the Himalayan region every few decades. Kathmandu Valley, which located in Himalayan region of Nepal, is surrounded by mountains and is filled with soft lake sediments. The strong-motion records from the 2015 Gorkha Nepal earthquake, which were obtained from Caltech (Rajaure et al. 2017), taken from THM observation station demonstrate basin effects. This station is located west of Kathmandu (27.68130ON, 85.37705OE) on a sedimentary site, as shown in Figure 5.1 (Takai et al. 2016).

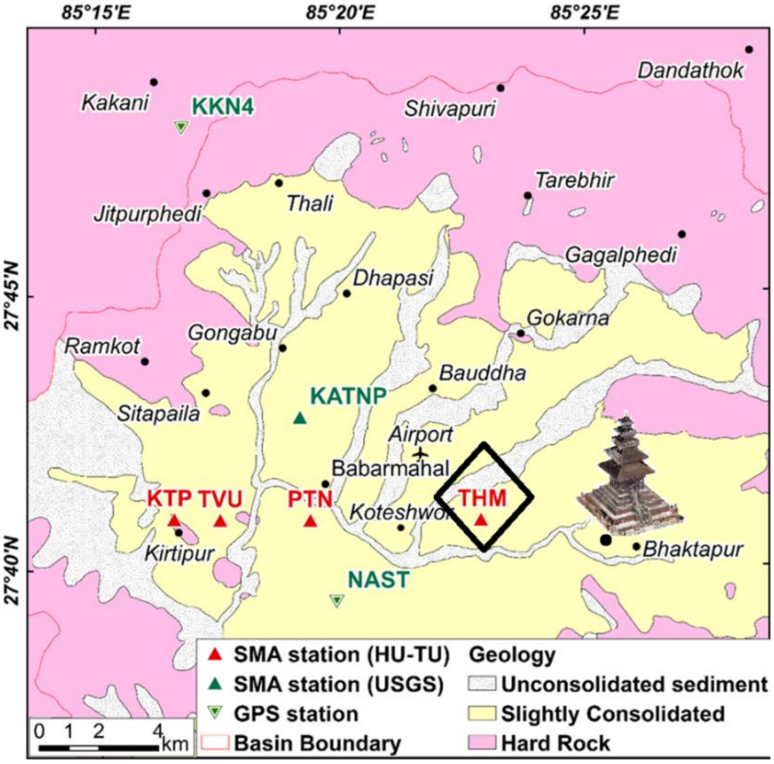

Figure 5.1: Geologic Formations' map in Kathmandu Valley shows the location of Nyatapol temple and the observation site of THM station in a sedimentary site (Takai et al. 2016).

The fault rupture was about 150 km (Wang and Fialko 2015) with a reverse fault mechanism, with a slight right-lateral strike-slip component (Feng et al. 2015; Takai et al. 2016). The mainshock (M_w 7.8) and the most pronounced aftershock (M_w 7.3) ground motions in both north-south and east-west directions are used in this work. Currently, no processed vertical motions are available for use (Rajaure et al. 2017). Although the vertical component is higher than the orthogonal components at THM station, it is slightly different from the dominant acceleration at various stations (Takai et al. 2016). The predominate peak ground acceleration (PGA) values at THM station is 0.15 g for the mainshock in the north-south direction and 0.13 g for the aftershock in the east-west direction. The largest PGA recorded at THM station was due to isolated short-period waves at about 47 s from the origin time. Figures 5.2 – 5.5 each illustrate the ground displacement, velocity, and acceleration records. Figures 5.2 and 5.3 represent the mainshock (M_w 7.8) in north-south and east-west directions, respectively. Figures 5.4 and 5.5 demonstrate the aftershocks (M_w 7.3) in both north-south and east-west directions.

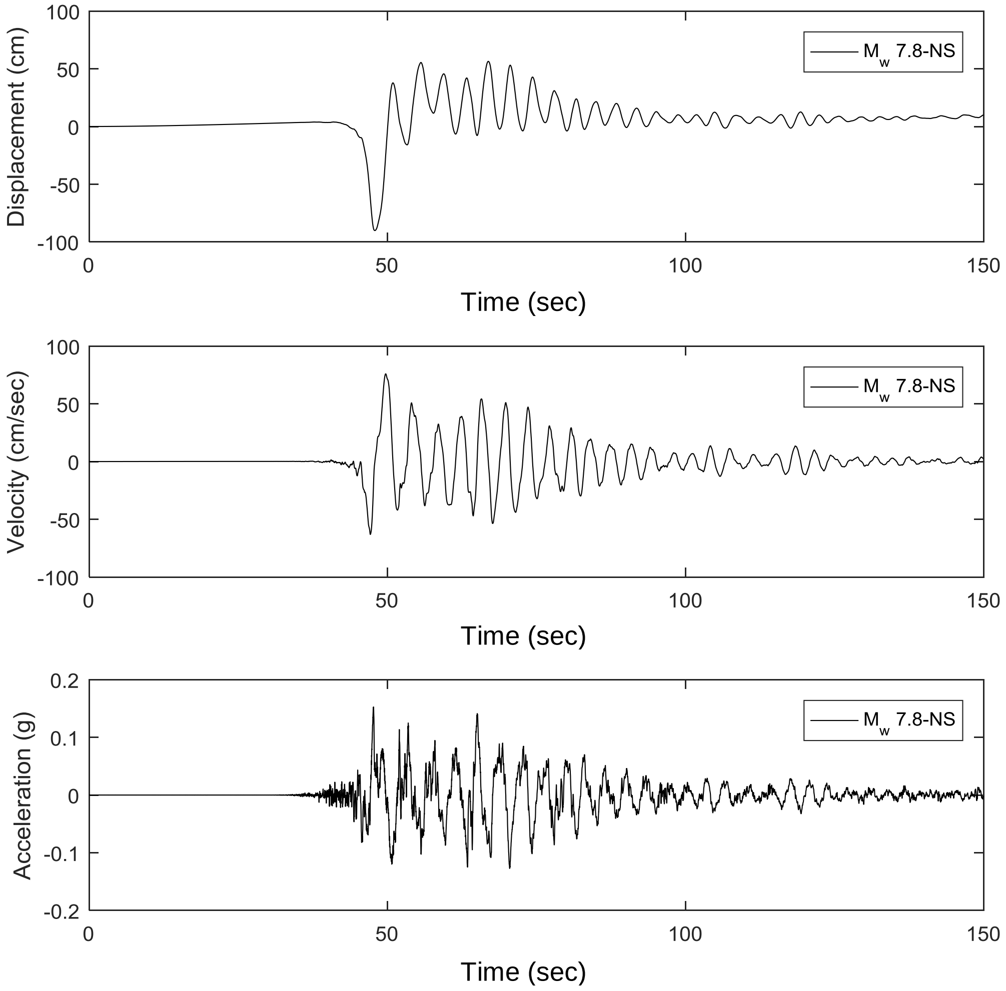

Figure 5.2: Displacement, velocity, and acceleration plots of mainshock Gorkha earthquake (M_w 7.8) in the NS direction recorded at THM station.

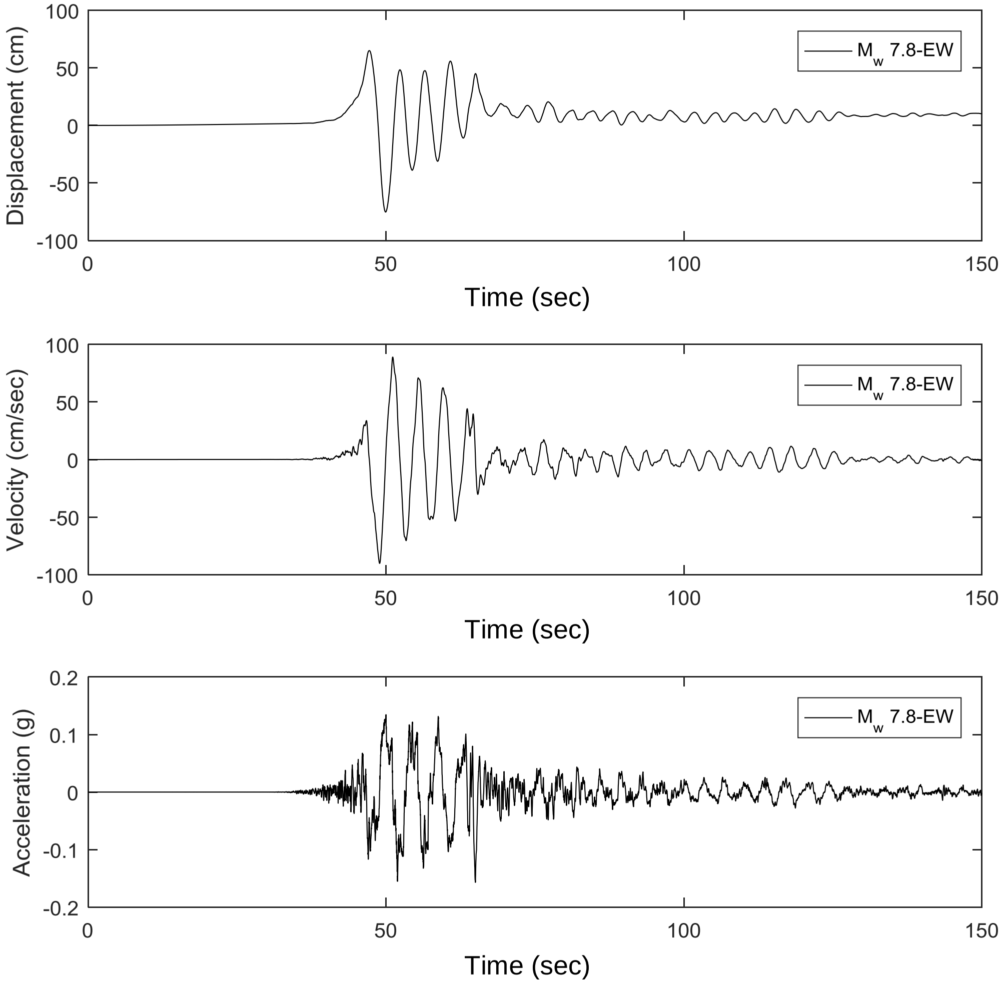

Figure 5.3: Displacement, velocity, and acceleration plots of mainshock Gorkha earthquake (M_w 7.8) in the EW direction recorded at THM station.

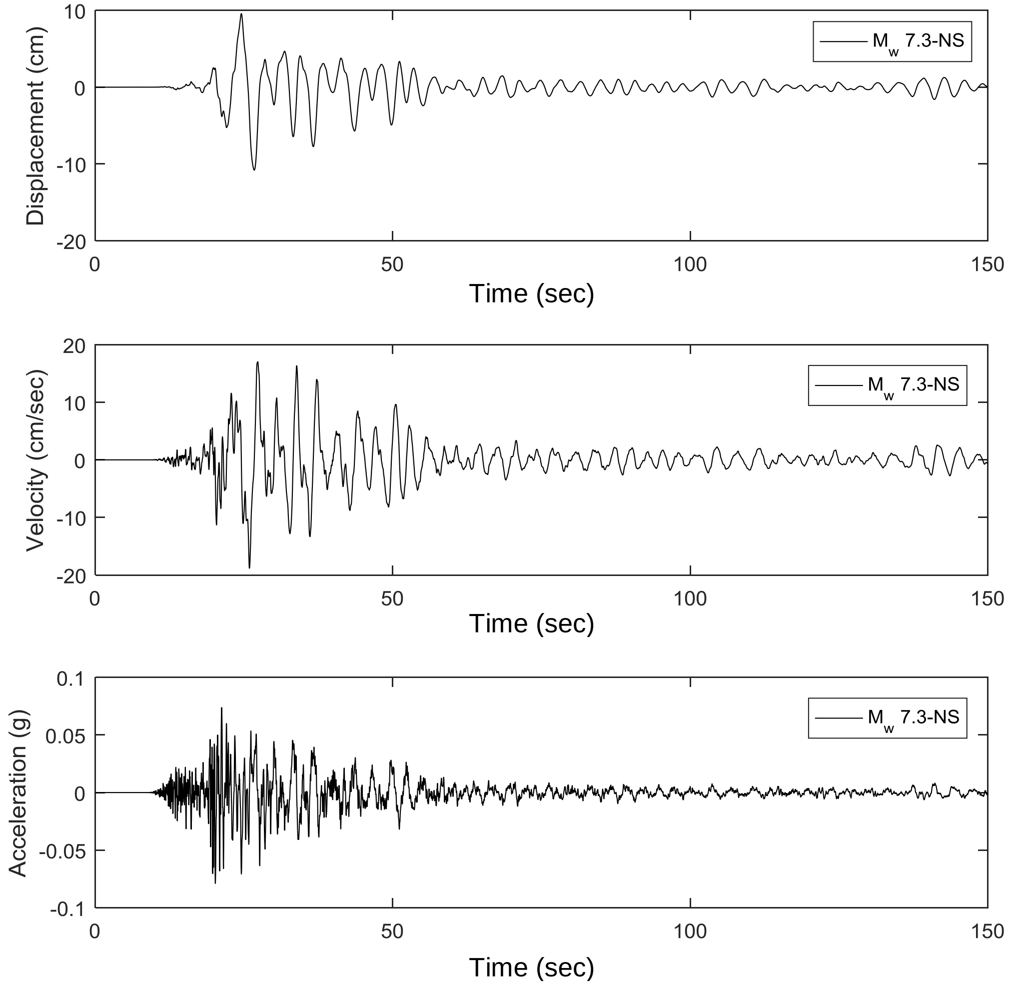

Figure 5.4: Displacement, velocity, and acceleration plots of aftershock Gorkha earthquake (M_w 7.3) in the NS direction recorded at THM station.

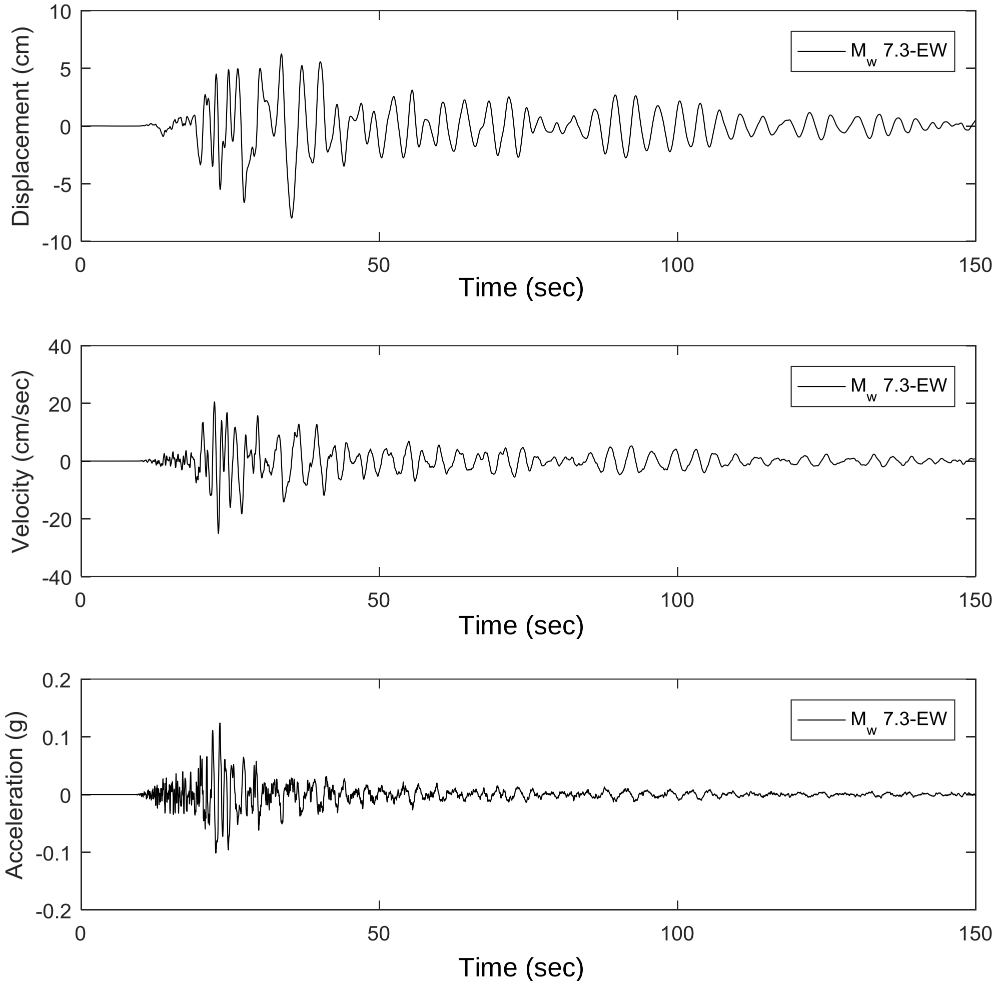

Figure 5.5: Displacement, velocity, and acceleration plots of aftershock Gorkha earthquake (M_w 7.3) in the EW direction recorded at THM station.

The 5% damped elastic spectral acceleration, velocity, and displacement curves for the unscaled are shown in Figures 5.6 – 5.8. The fundamental periods of the pre-and post-earthquake FEM of the Nyatapola are identified by vertical green and blue lines, respectively, as well as the valid frequency content for at least two seconds. In these figures, a predominant increase in spectral acceleration is noted for higher periods (≥ 1 s). These unscaled ground motions are anticipated to contribute to damage for more flexible structures, in comparison to stiffer buildings such as Nyatapola temple, which stood upright in the 2015 Gorkha earthquake. This may be due to smaller response amplifications for its lower fundamental periods (pre- and post-earthquake) and damping induced by the number of cracks induced. The unscaled ground motions are placed at the base of the FEM structure as described in the next section.

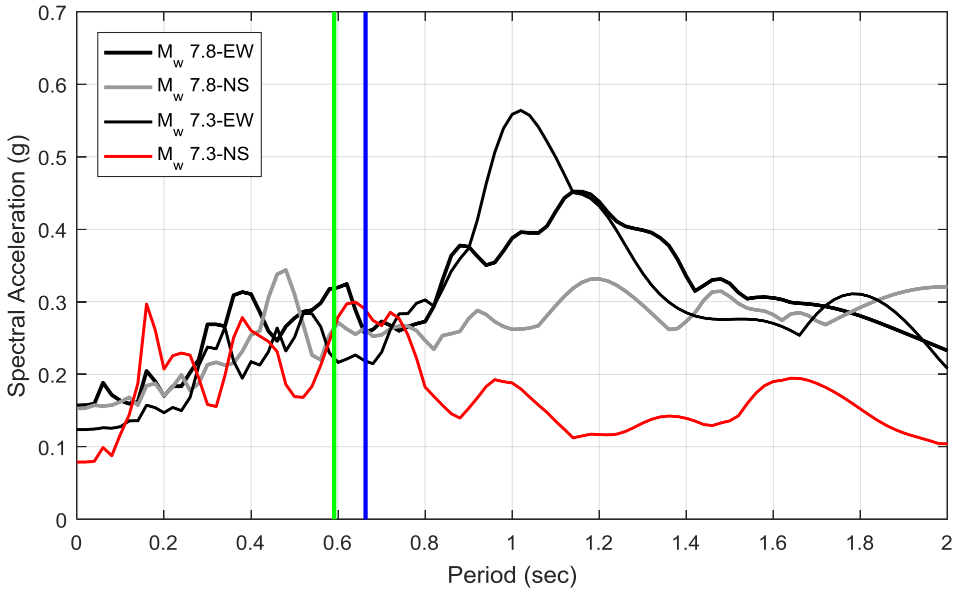

Figure 5.6: Elastic 5% damped spectral acceleration curves of Gorkha earthquake (unscaled). Mainshock (M_w 7.8) and aftershock (M_w 7.3) ground motions are recorded at THM station in both NS and EW directions. The green and blue vertical lines identify the fundamental periods of the pre-and post-earthquake FEM, respectively.

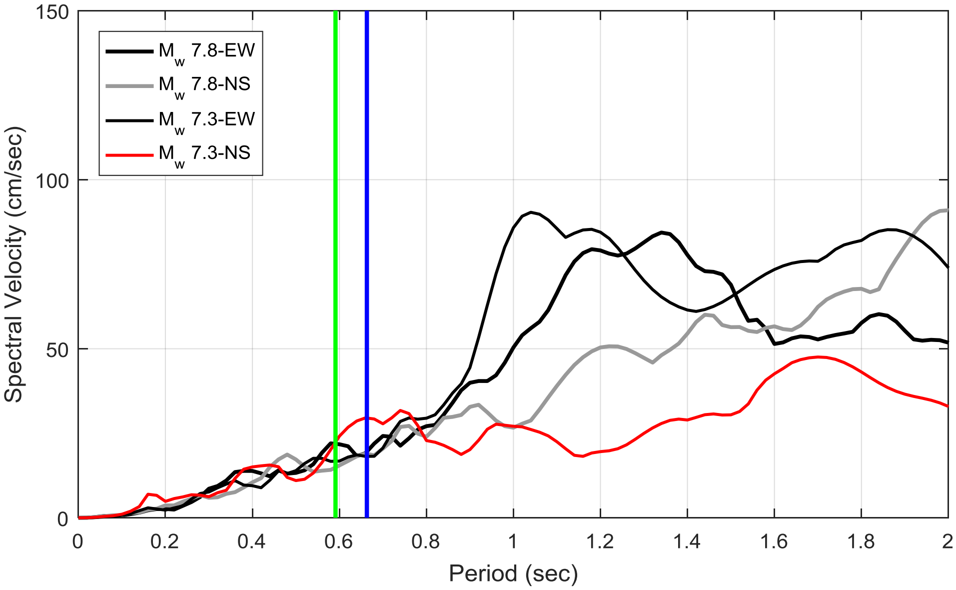

Figure 5.7: Elastic 5% damped spectral velocity curves of Gorkha earthquake (unscaled). Mainshock (M_w 7.8) and aftershock (M_w 7.3) ground motions are recorded at THM station in both NS and EW directions. The green and blue vertical lines identify the fundamental periods of the pre-and post-earthquake FEM, respectively.

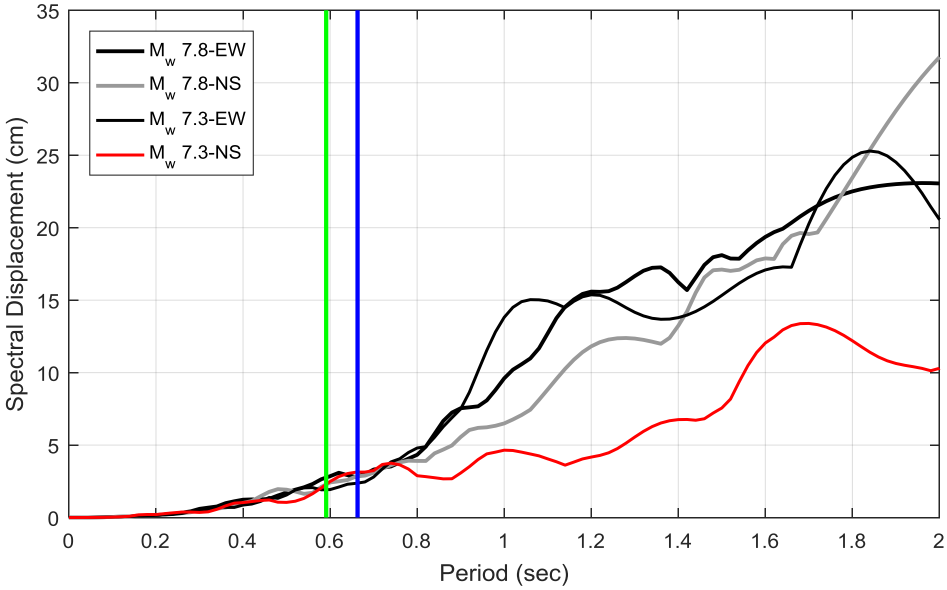

Figure 5.8: Elastic 5% damped spectral displacement curves of Gorkha earthquake (unscaled). Mainshock (M_w 7.8) and aftershock (M_w 7.3) ground motions are recorded at THM station in both NS and EW directions. The green and blue vertical lines identify the fundamental periods of the pre-and post-earthquake FEM, respectively.

5.3 Linear Time History Response

Linear time histories can be considered as a conservative method in comparison to nonlinear approaches and require only moderate complexity and efficient computation (Marjanishvili 2004). In this work, the nonlinear response of the structural components is unknown, so for conservatism only linear responses are considered. The linear time-histories response analyses were conducted in SAP2000. The mainshock (M_w 7.8) acceleration time history record (bidirectional pair) was applied to base of the pre-earthquake model, while the aftershock (M_w 7.3) record pair was applied to the post-earthquake model. No scaling was considered and bidirectional components, associated with the north-south and the east-west directions, were applied simultaneously for each model. Rayleigh damping was set 5% in the 1st and 3rd modes for both pre- and post-earthquake models (Wood and Hutchinson 2012). SAP2000 utilizes modal superposition transient dynamic analysis, where the total structural response is computed by the summation of modes. The response of each mode is computed using step-by-step integration of the equations of motion for the modal response.

5.3.1 Maximum Floor Displacement Distribution

An initial example to quantify the response of the temple is to explore for the maximum floor displacement profiles. The maximum floor displacements are extracted from the floor level displacement time histories. The maximum displacement distribution is evaluated as the absolute valued maximum value of the relative displacement at each corner of each floor, as obtained from each record.

The maximum floor displacement, illustrated in Figure 5.9, increases with height as anticipated. The maximum N-S (north-south) displacement of 6.7 cm occurred during the aftershock record at the upper floor (roof). This is larger than the maximum N-S displacement of 5 cm due under the mainshock. The maximum E-W (east west) floor displacement is presented in Figure 5.10. Contrary to the orthogonal direction the maximum E-W displacement of 5.4 cm was observed at the roof due to the mainshock record. A smaller value of 5.1 cm was observed for the aftershock. The maximum floor displacements shown in Figure 5.11 envelopes for the entire system at each record, with an overall maximum of 6.7 cm at upper floor due to aftershock record. These displacement profiles increase with height and follow a linear trend (shear-like mode) at the lower floors and parabolic (bending-like mode) at the upper floors.

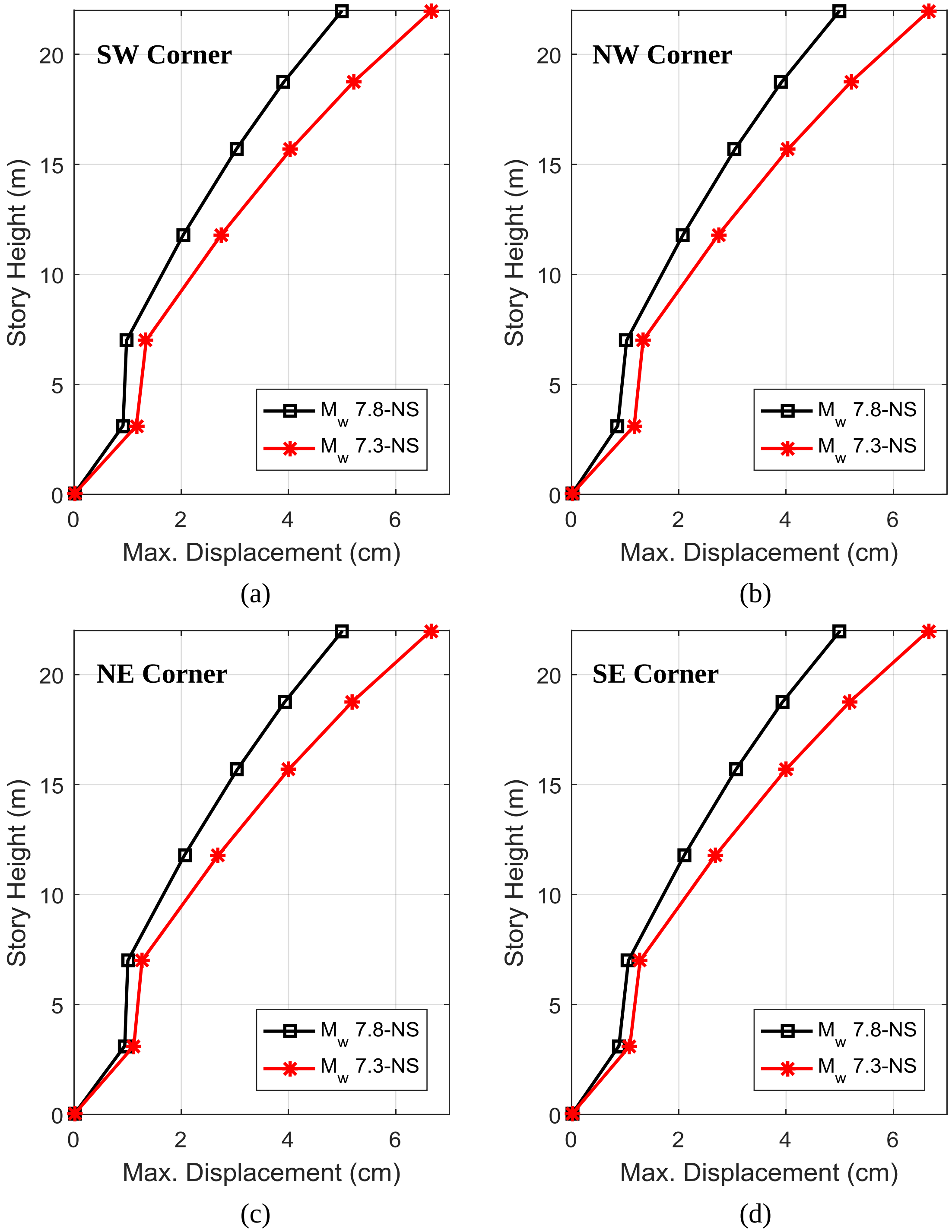

(a)

(b)

(c)

(d)

Figure 5.9: Maximum floor displacement envelope curves for the Nyatapola temple in the NS direction: (a) south-west corner, (b) north-west corner, (c) north-east corner, and (d) south-east corner.

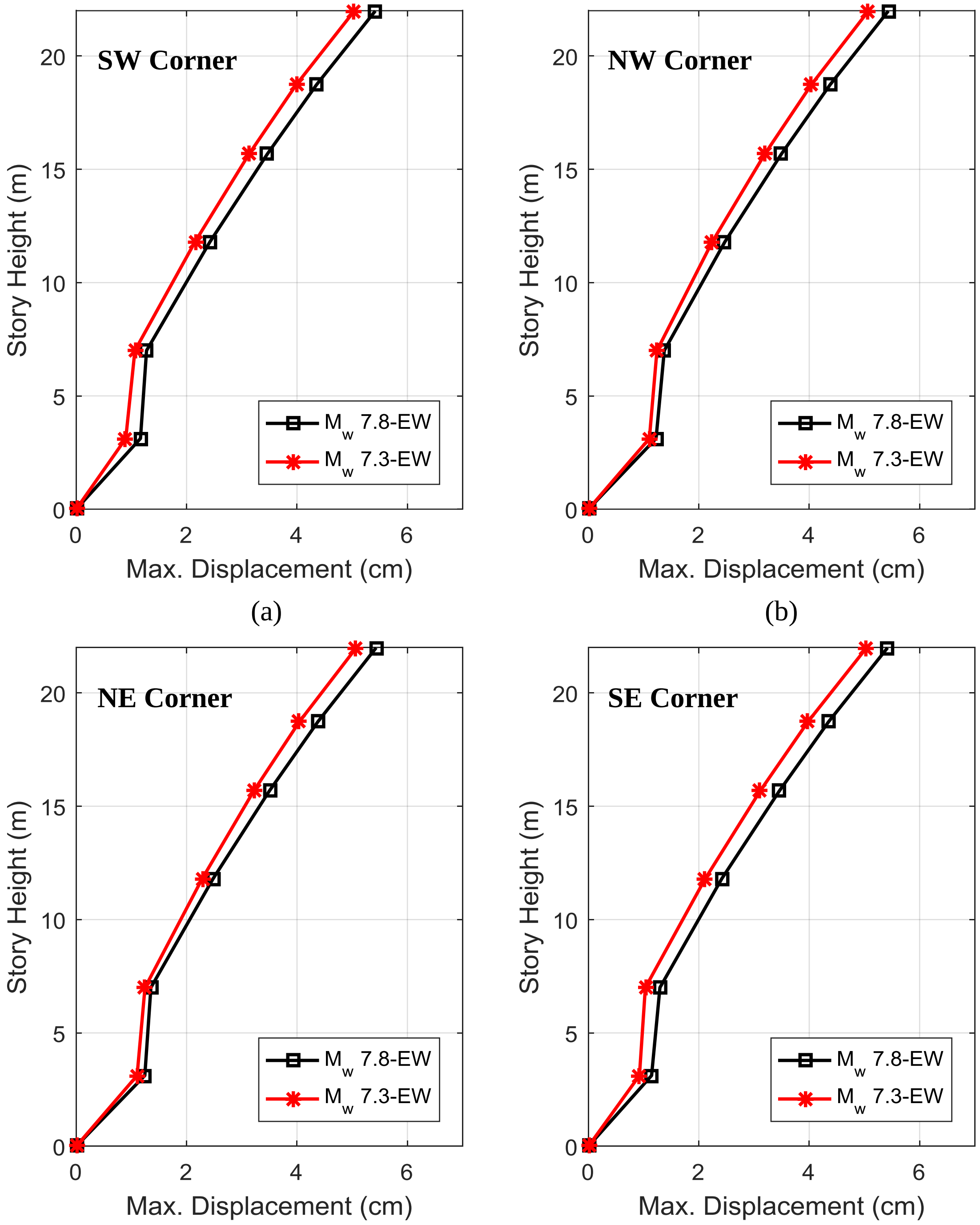

(a)

(b)

(c)

(d)

Figure 5.10: Maximum floor displacement envelope curves for the Nyatapola temple in the E-W direction: (a) south-west corner, (b) north-west corner, (c) north-east corner, and (d) south-east corner.

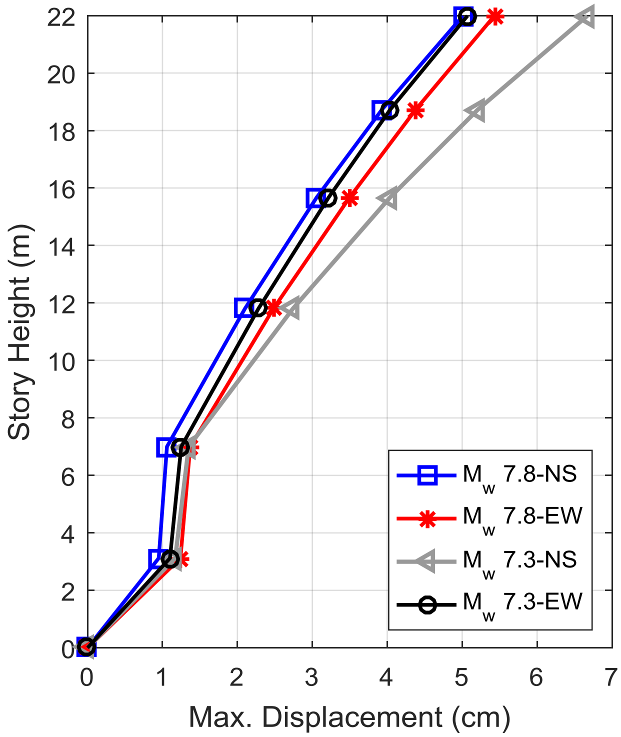

Figure 5.11: Maximum floor displacement envelope curves for the Nyatapola temple.

5.3.2 Maximum Interstory Drift Distribution

The second response considered is interstory drift. The interstory drift relation can be evaluated as:

$$\gamma^{\text{IS}} = \frac{|\Delta_\text{i}| - |\Delta_{\text{i}-1}|}{\text{h}_\text{i} - h_{i-1}} \tag{5-1}$$

Where γ_{is} = interstory drift at floor i, Δ_i = displacement at floor i, and h_i = height of floor i. Figure 5.12 illustrates the absolute maximum interstory drift curve. The maximum interstory drift increases with height except for the first floor (L1b), where sharply decrease is observed of nearly 90%. The maximum interstory demands of 0.45%

occurred in the aftershock (M_w 7.3) in the north-south direction at the upper floor. The percent difference of the maximum interstory drift at the roof between the mainshock (M_w 7.8) and aftershock (M_w 7.3) was 26% and 0.6% in the north-south and east-west directions, respectively. Additional details for the interstory drift of each corner can be found in Appendix A.

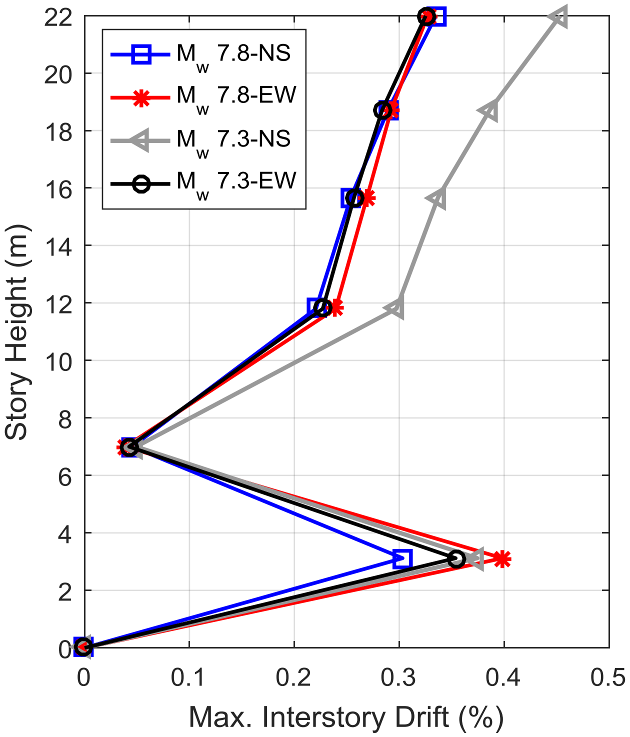

Figure 5.12: Maximum interstory drift curves in (%) for the Nyatapola temple.

5.3.3 Maximum Floor Acceleration Distribution

The third response quantify examined is the maximum floor acceleration profiles. Studying the behavior of the acceleration time histories at each floor is an essential outcome in time history analysis where it provides information about how the structure filters and amplifies the input ground motion on each floor of the temple. In addition, it demonstrates the force that components/walls/etc. need to resist. The maximum absolute acceleration envelops at each floor was obtained from the acceleration time history responses. Figure 5.13 demonstrates the distribution of the maximum absolute acceleration profile at each floor where it generally increases with height. The maximum absolute acceleration experienced by Nyatapola reached a maximum of 0.6 g at the uppermost level in the aftershock simulation in the north-south direction. The percent difference of the maximum absolute acceleration at roof between the mainshock (M_w 7.8) and aftershock (M_w 7.3) was 35% and 17% in the north-south and east-west directions, respectively. It is notable that the distribution of maximum acceleration follows a linear trend (shear-like mode) for all records except for the aftershock record in the north-south direction where follows a parabolic trend (bending-like mode). The linear/shear-like response indicates the potential dependency of the first mode, while the parabolic trend is representative of higher mode contributions. Additional details for the absolute acceleration profiles of each corner can be found in Appendix B.

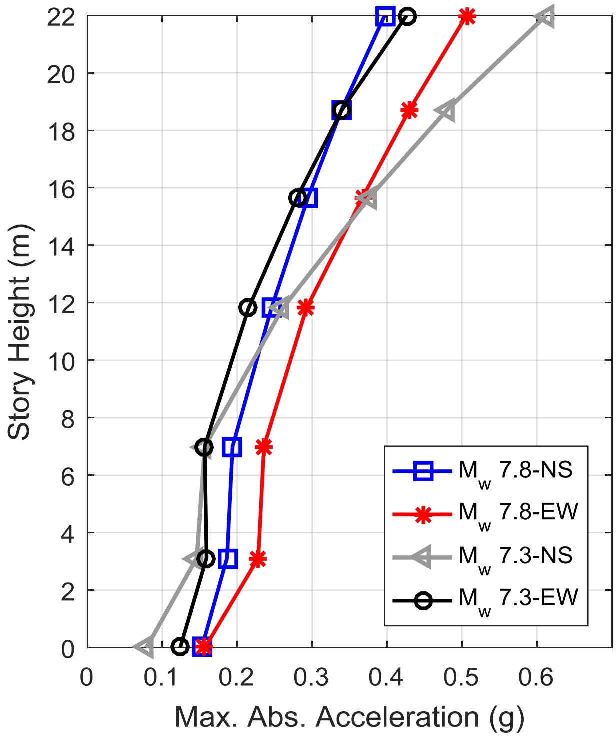

Figure 5.13: Maximum absolute acceleration envelope curves for the Nyatapola temple.

5.3.4 Uncorrelated Acceleration Amplification Ratio

The fourth response quantify examined is the uncorrelated acceleration amplification ratio. This defines as a relation between the absolute maximum floor acceleration to the maximum input acceleration (PGA). Equation (5-2) is used to compute the uncorrelated acceleration amplification ratio Ω (a unitless parameter).

$$\Omega_i = \frac{max(|\ddot{u}_i|)}{PGA} \tag{5-2}$$

Where $\ddot{u}_i$ = the acceleration response of floor i and PGA = the peak ground acceleration. In the investigation of the meaning of uncorrelated in this context, that the maximum floor acceleration may not necessarily occur simultaneously with the peak ground acceleration (Wood and Hutchinson 2012). These increasing trend of distribution clarify the significant influence of higher modes. Figure 5.14 illustrates the distribution of the uncorrelated acceleration amplification ratio at each floor. This increasing of distribution trends clarify the significant influence of higher modes where was most notable under the effect of the aftershock in the north-south direction which reached a significant amplification value of 7.7 at the uppermost level. The percent difference of the maximum uncorrelated acceleration amplification ratio at roof between the mainshock (M_w 7.8) and aftershock (M_w 7.3) was 67% and 7% in the north-south and east-west directions, respectively. Additional details about the uncorrelated acceleration amplification ratio profiles of each corner can be found in Appendix C.

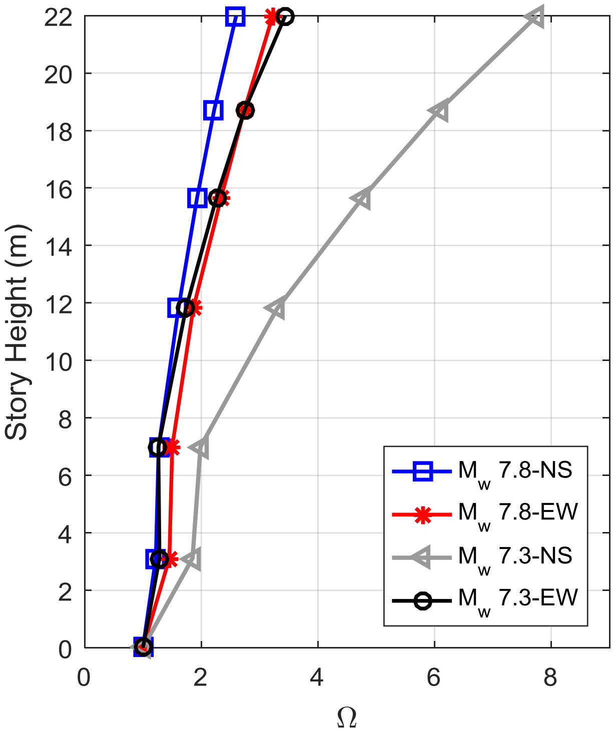

Figure 5.14: Uncorrelated acceleration amplification ratio, Ω, for the Nyatapola temple.

5.3.5 In-Structure Spectral Acceleration Response

In-structure spectral acceleration response permits an examination of the frequencies that contribute to the response of the internal structural. This sheds lights into the filtering of the structure due to its base excitation and its distribution over height. Figures 5.15 – 5.17 illustrates an example of the 5% damped spectral acceleration response at the southwestern corner of the pre- and post-earthquake models in each of the first floor (L1b), third floor (L3), and fifth floor (L5), respectively.

An in-structure spectrum is computed from the displacement time histories of the corresponding floor levels. In the frequency domain the response of the first-floor spectral acceleration at the selected corner of the temple tends to predict higher peak acceleration demand at higher frequencies (third mode) due to the aftershock in the east-west direction while tends to predict higher peak acceleration at the lower frequency (fundamental frequency) due to the applied mainshock record as shown in Figure 5.15. Figure 5.16 illustrates the third-floor in-structure spectral acceleration which tends to quantify higher peak acceleration demand at lower frequency (fundamental mode). The maximum peak acceleration of (1.93 g) due to mainshock was sharply decreased by 48% compared with the maximum peak acceleration of (1 g) subjected to aftershock in the east-west direction. Similar to the third-floor, the fifth-floor tends to quantify higher peak acceleration demands at higher periods except for the response under the aftershock in the east-west direction, where the higher modes have a larger quantity in the response spectral acceleration as demonstrated in Figure 5.17. The maximum acceleration contributing to fifth-floor response at the lower modes is decreased by 33% from (3.3 g) to (2.2 g) when comparing the effect of mainshock to the aftershock in the north-south direction.

It can be concluded that in-structure acceleration demands of the temple are more critical in the higher floors, where peak spectral accelerations reached 3 g, while in the lower level it did not exceed than 1 g. On the other hand, the aftershock record in the E-W direction has a more notable effect on the higher modes when compared with mainshock record. In contrary, the mainshock record has a clear impact on the lower frequency.

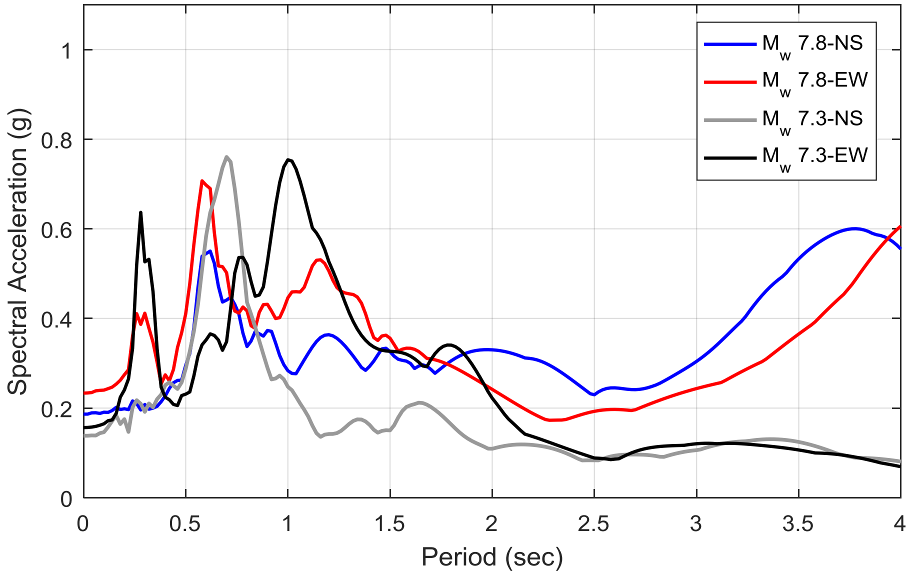

Figure 5.15: Elastic 5% Damped Spectral acceleration example for the SW corner of the first floor (L1b).

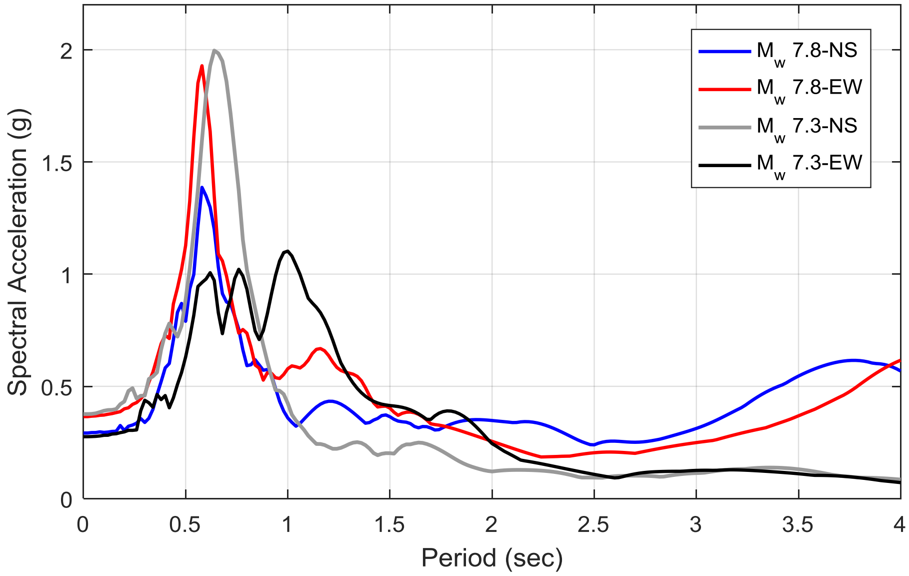

Figure 5.16: Elastic 5% Damped Spectral acceleration example for the SW corner of the third floor (L3).

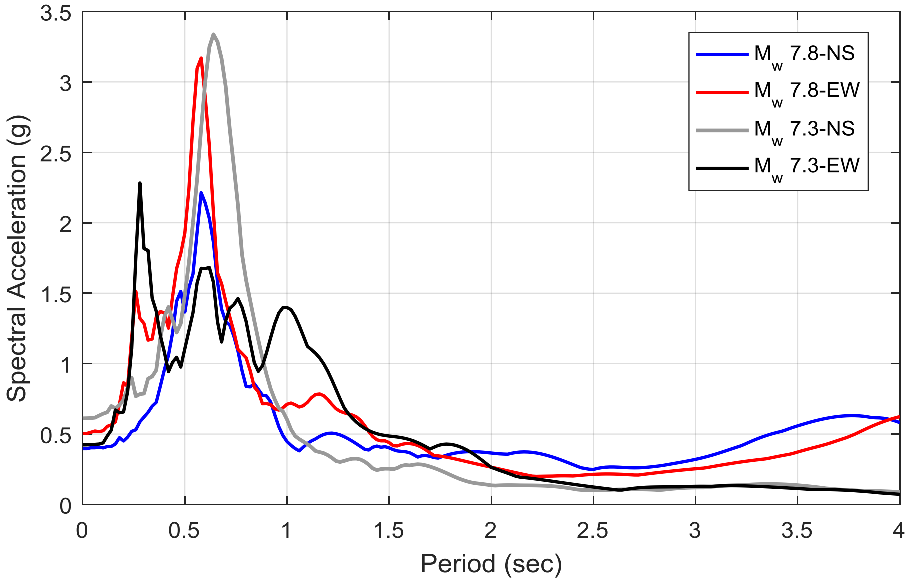

Figure 5.17: Elastic 5% Damped Spectral acceleration example for the SW corner of the fifth floor (L5).

5.3.6 Torsional Demand Profiles

The results of the displacement from time history analysis were synthesized to generate the torsional demand profiles. Figures 5.18 and 5.19 show, respectively, the torsional permanent drift profiles and corner rotations of the Nyatapola temple which were found by subjecting the pre-earthquake FEM to the mainshock (M_w 7.8). The maximum rotational angles experienced by Nyatapola reached a maximum of 0.0058° at the first floor. Displacements and the rotational angles values for pre-earthquake FEM are presented in Tables 5.1 and 5.2, respectively.

Torsional permanent drift profiles and corner rotations for post-earthquake FEM which influenced by the aftershock (M_w 7.3) records are summarized in Figures 5.20 and 5.21, respectively. The rotational angles vary with the temple's height where the maximum of 0.17° occurred at first floor (L1b) of the temple. More information about the maximum displacements and the values of the rotations' angles at each floor of the post-earthquake FEM are illustrated in Tables 5.3 and 5.4, respectively.

By analyzing the results, the temple experienced inconsistent large lateral drifts as a result of torsion, which is more pronounced at first floor. In both pre- and post-earthquake FEM, the rotational angles of the southwestern and northwestern corners are identical to the southeastern and northeastern corners, respectively. The torsional drift in post-earthquake model subjected to aftershock event is more noticeable (maximum rotation of 0.17° at first floor) compared to pre-earthquake model with mainshock loading. This torsional behavior can be a function of the ground motion, where sufficient energy activates and alters the percentage of participating modal masses. The torsion was evident in the first floor and likely caused the poor connection between the wall layers, especially the middle core layer that filled with rubble stone, brick fragment, and mud.

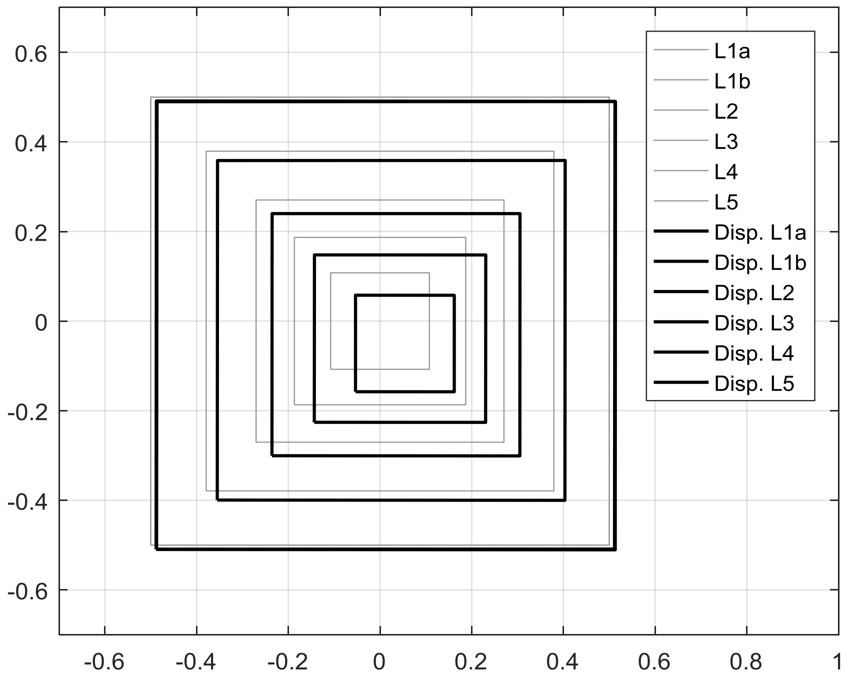

Figure 5.18: Torsional permanent drift profiles of Nyatapola temple subjected to Gorkha mainshock (M_w 7.8) recorded at THM station.

Table 5.1: Maximum displacements in (cm) of the pre-earthquake FEM subjected to the mainshock (M_w 7.8) records.

Floor No.	Directions	SW Corner	NW Corner	NE Corner	SE Corner
L1a	EW	1.16	1.23	1.24	1.14
	NS	-0.91	-0.86	-0.95	-0.88
L1b	EW	1.27	1.37	1.35	1.30
	NS	-0.98	-1.03	-1.00	-1.06
L2	EW	2.42	2.47	2.48	2.42
	NS	-2.04	-2.08	-2.06	-2.10
L3	EW	3.46	3.50	3.50	3.46
	NS	-3.02	-3.04	-3.04	-3.06
L4	EW	4.35	4.38	4.38	4.35
	NS	-3.91	-3.91	-3.92	-3.93
L5	EW	5.42	5.43	5.43	5.42
	NS	-5.00	-5.00	-5.01	-5.01

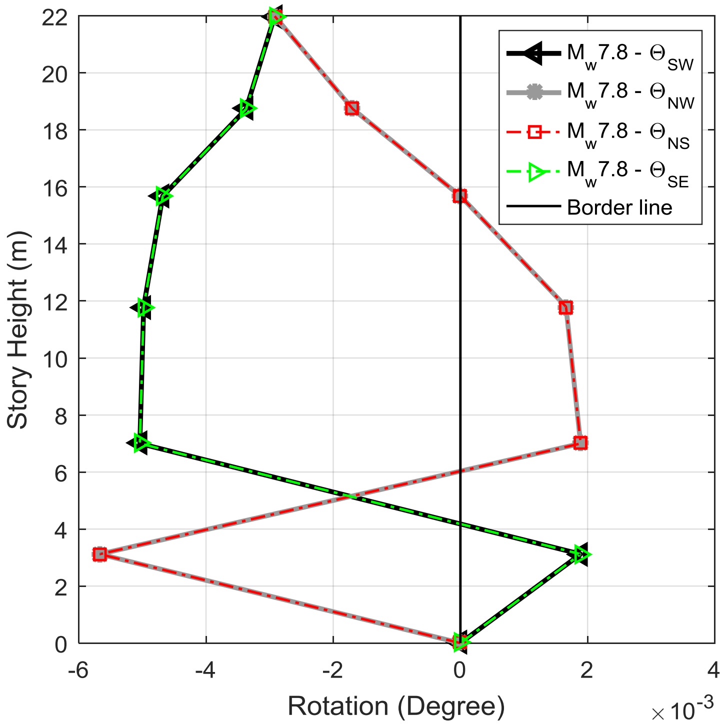

Figure 5.19: Rotations' angles of Nyatapola temple in (degree) subjected to Gorkha mainshock (M$_w$ 7.8) recorded at THM station.

Table 5.2: Rotations' angles in (degree) of the pre-earthquake FEM subjected to the mainshock (M$_w$ 7.8) records.

Floor No.	θ_{SW}	θ_{NW}	θ_{NE}	θ_{SE}
L1a	1.89E-03	-5.67E-03	-5.67E-03	1.89E-03
L1b	-5.04E-03	1.89E-03	1.89E-03	-5.04E-03
L2	-4.98E-03	1.66E-03	1.66E-03	-4.98E-03
L3	-4.68E-03	0.00E+00	0.00E+00	-4.68E-03
L4	-3.37E-03	-1.69E-03	-1.69E-03	-3.37E-03
L5	-2.92E-03	-2.92E-03	-2.92E-03	-2.92E-03

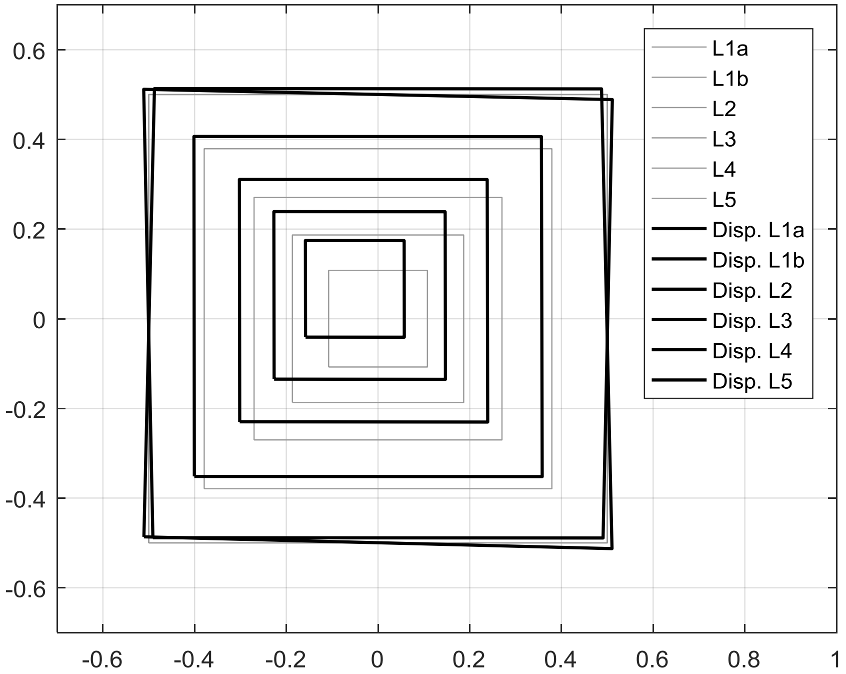

Figure 5.20: Torsional permanent drift profiles of Nyatapola temple subjected to Gorkha aftershock (M_w 7.3) recorded at THM station.

Table 5.3: Maximum displacements in (cm) of the post-earthquake FEM subjected to the aftershock (M_w 7.3) records.

Floor No.	Directions	SW Corner	NW Corner	NE Corner	SE Corner
L1a	EW	0.90	-1.10	1.10	-0.92
	NS	1.16	1.17	-1.12	1.09
L1b	EW	-1.06	1.24	-1.25	1.03
	NS	1.35	1.33	1.27	-1.28
L2	EW	-2.15	-2.24	-2.28	-2.11
	NS	2.74	2.74	2.70	2.69
L3	EW	-3.13	-3.20	-3.22	-3.11
	NS	4.04	4.03	4.00	3.99
L4	EW	-3.98	-4.04	-4.04	-3.98
	NS	5.21	5.20	5.18	5.17
L5	EW	-5.04	-5.07	-5.07	-5.04
	NS	6.67	6.67	6.65	6.65

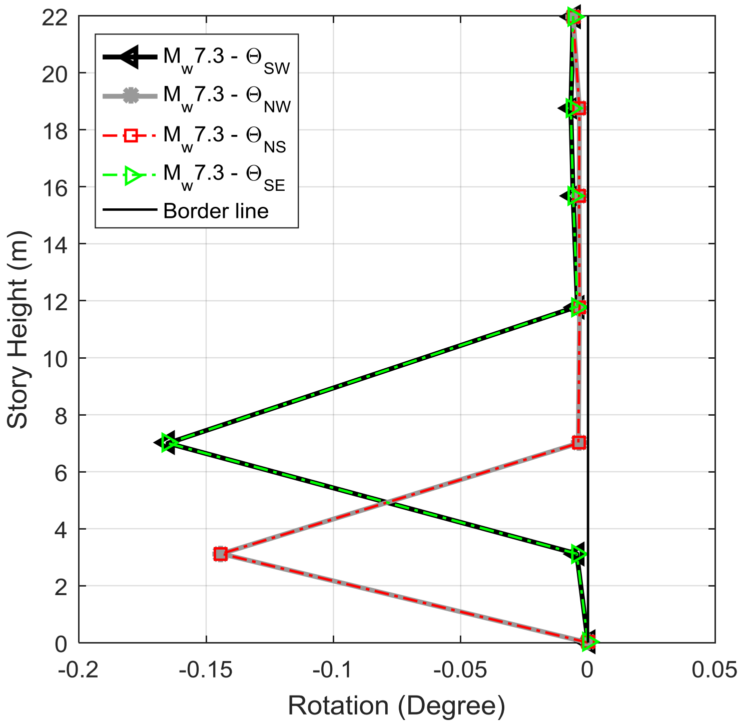

Figure 5.21: Rotations' angles of Nyatapola temple in (degree) subjected to aftershock (M_w 7.3) recorded at THM station.

Table 5.4: Rotations' angles in (degree) of the post-earthquake FEM subjected to the aftershock (M_w 7.3) records.

Floor No.	θ_{SW}	θ_{NW}	θ_{NE}	θ_{SE}
L1a	-4.42E-03	-1.44E-01	-1.44E-01	-4.42E-03
L1b	-1.65E-01	-3.79E-03	-3.79E-03	-1.65E-01
L2	-4.15E-03	-3.32E-03	-3.32E-03	-4.15E-03
L3	-5.85E-03	-3.51E-03	-3.51E-03	-5.85E-03
L4	-6.74E-03	-3.37E-03	-3.37E-03	-6.74E-03
L5	-5.85E-03	-5.85E-03	-5.85E-03	-5.85E-03

The FE-based torsional drift results can also be compared with estimated values extracted from point cloud data following the 2015 Gorkha earthquake (Wood et al. 2017b), as shown in Figure 5.22. The first-floor numerical results match very well (0.15º clockwise) with the point cloud estimates, whereas significant disparity was seen for floors 2 to 5. This difference may be attributed to assuming a perfectly aligned, rectangular structure assumption by Wood et al. (2017b), which is unlikely to be the case due to the construction practices.

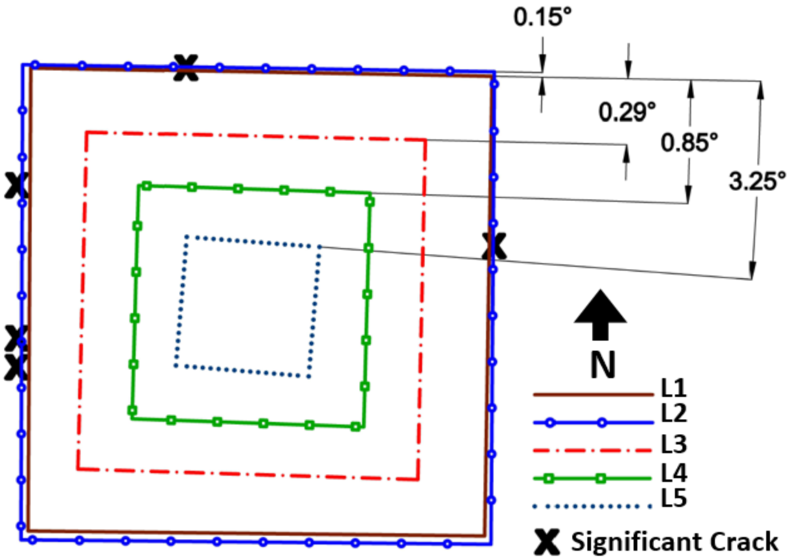

Figure 5.22: Torsional permanent drift profiles estimated using lidar (Wood et al. 2017b).

5.4 Damping Case Study

Despite Rayleigh damping being very common in structural dynamic analysis programs, sometimes it is not available in all software. One example is applied element method platforms, where only mass proportional damping (MPD) is available. To compare this developed FE model to an applied element method model in future work, the effect of the mass proportional damping is compared to Rayleigh damping to provide a comprehensive insight into the temple's sensitivity to damping. In this short case study, only the damping was altered and, in this case, the MPD was set to 6% of critical in the first mode (fundamental frequency) and a similar linear dynamic time history study was undertaken for the post-earthquake model under the aftershock excitation. Figures 5.23 – 5.26 illustrate a comparison between two damping methods for various response quantities.

By analyzing the results, as shown in Figure 5.23, the effect of the mass proportional damping on the maximum floor displacement profile led to reducing the relative maximum displacement by approximately 6.9% in the north-south direction at upper level (roof), while increasing it by about 7.7% in the east-west direction at the same level. The general distribution maximum displacement trend is similar, since the displacement response is predominately controlled by the first mode response. The maximum interstory drift profiles calculated based on Equation (5-1) for post-earthquake FEM are illustrated in Figure 5.24, with only minimal differences between the damping cases with a maximum difference of approximately 6.9%.

A comparison of the maximum absolute acceleration between damping cases is shown in Figure 5.25. The effect of the mass proportional damping on the maximum absolute acceleration led to reducing the maximum acceleration by approximately 6.9% in the north-south direction at the upper floor, while increasing it by 40.7% in the east-west direction at the same floor. Figure 5.26 illustrates the distribution of the uncorrelated acceleration amplification ratio at each floor calculated using Equation (5-2) by applying aftershock (M_w 7.3) records. The impact of the mass proportional damping on the maximum absolute acceleration was reduced the maximum acceleration by approximately 6.4% in the north-south direction at the upper floor while it increased by 44.1% in the east-west direction at the same floor, very similar to the maximum acceleration values.

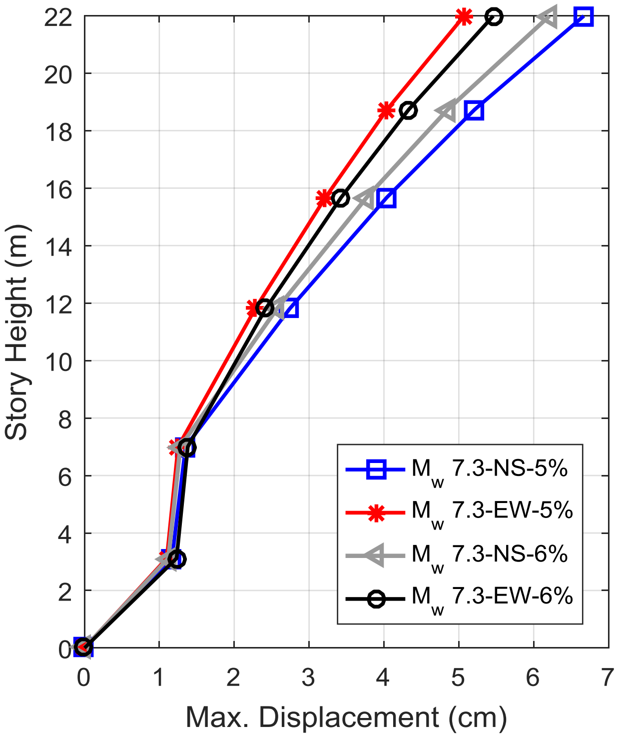

Figure 5.23: Maximum floor displacement envelope curves for Nyatapola temple using two damping techniques: Rayleigh damping set as 5% for 1st and 3rd modes and MPD as set 6% for 1st mode.

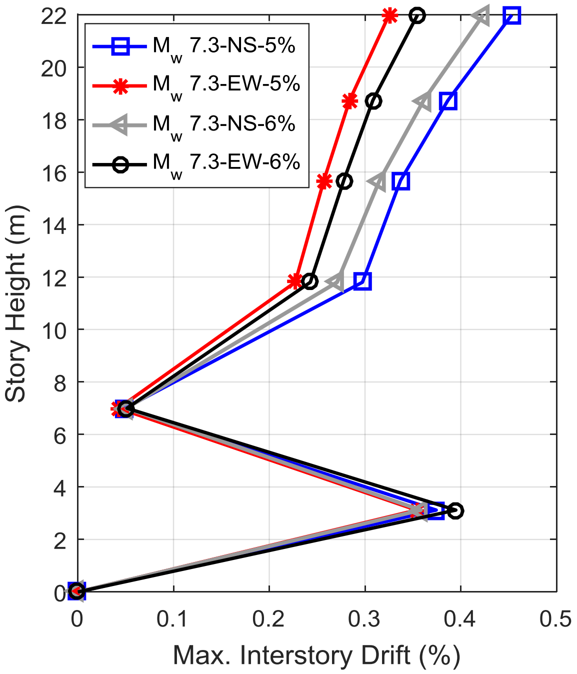

Figure 5.24: Maximum interstory drift curves for Nyatapola temple using two damping techniques: Rayleigh damping set as 5% for 1st and 3rd modes and MPD as set 6% for 1st mode.

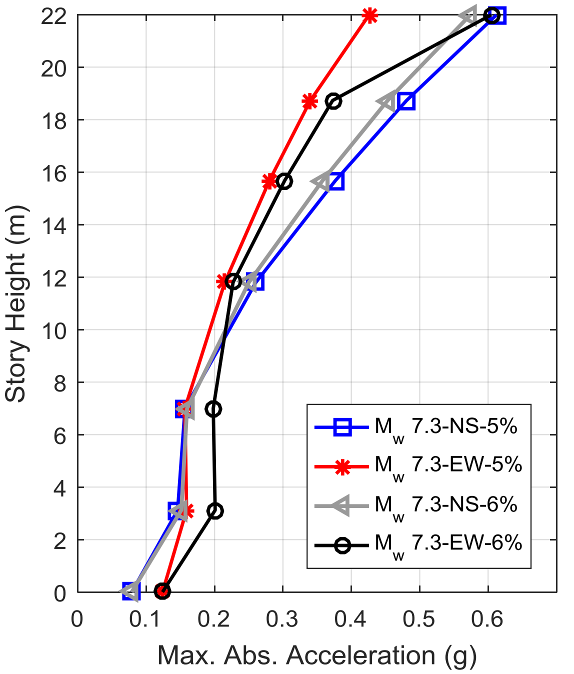

Figure 5.25: Maximum absolute acceleration envelope curves for Nyatapola temple using two damping techniques: Rayleigh damping set as 5% for 1st and 3rd modes and MPD as set 6% for 1st mode.

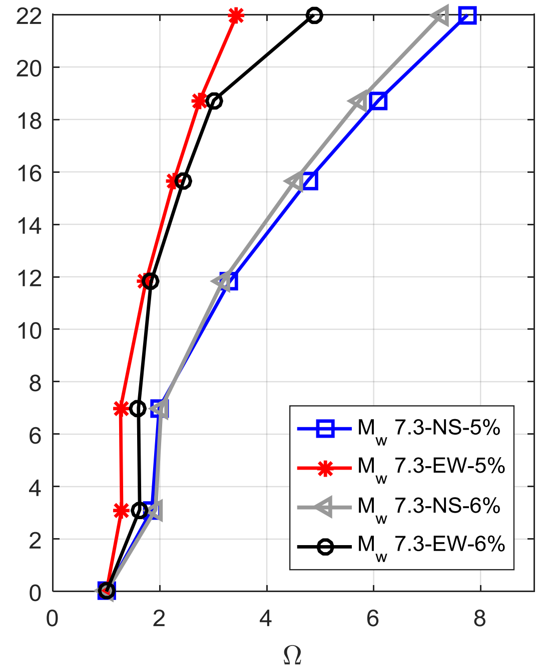

Figure 5.26: Uncorrelated acceleration amplification ratio for Nyatapola temple using two damping techniques: Rayleigh damping set as 5% for 1st and 3rd modes and MPD as set 6% for 1st mode.

To explore the frequency distribution and in-structure filtering, 5% damped spectral acceleration is computed of the displacement floor responses for the southwestern corner of the post-earthquake model for levels L1b, L3, L5. These are illustrated in Figures 5.27 – 5.29. The response of the first-floor spectral acceleration demand at the selected corner of the temple is shown in Figure 5.27. MPD resulted in reduced peak acceleration demands in the north-south direction, however significant increases were observed in the east-west direction at the higher frequency, due to the underdamped frequencies associated with MPD in comparison to Rayleigh damping. The maximum peak acceleration of (0.64 g) using Rayleigh damping was sharply increased by 43% compared with the maximum peak acceleration of (1.13 g) using MPD. A similar trend is shown for the third floor and fifth floors in Figures 5.28 and 5.29.

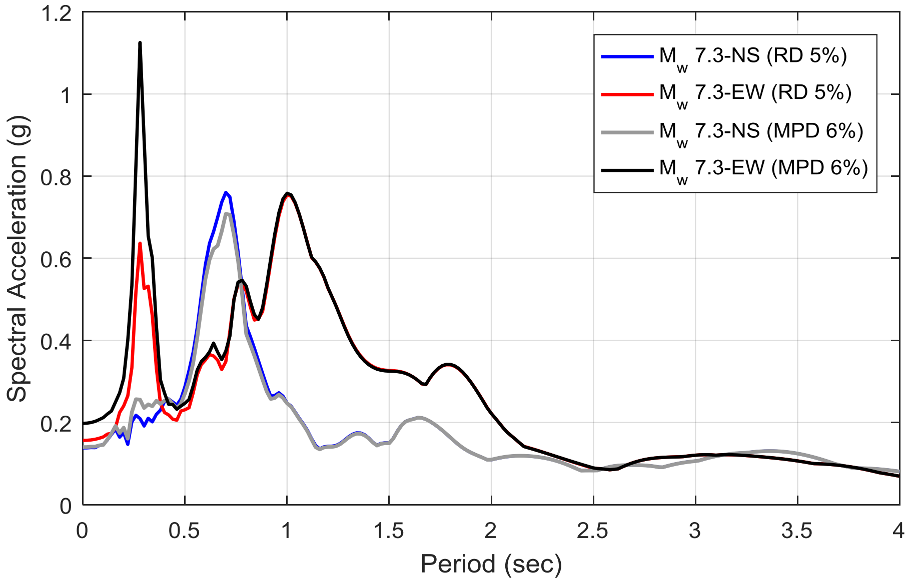

Figure 5.27: Elastic 5% Damped Spectral acceleration example for the SW corner of the first floor (L1b) for Nyatapola temple using two damping techniques: Rayleigh damping set as 5% for 1st and 3rd modes and MPD as set 6% for 1st mode.

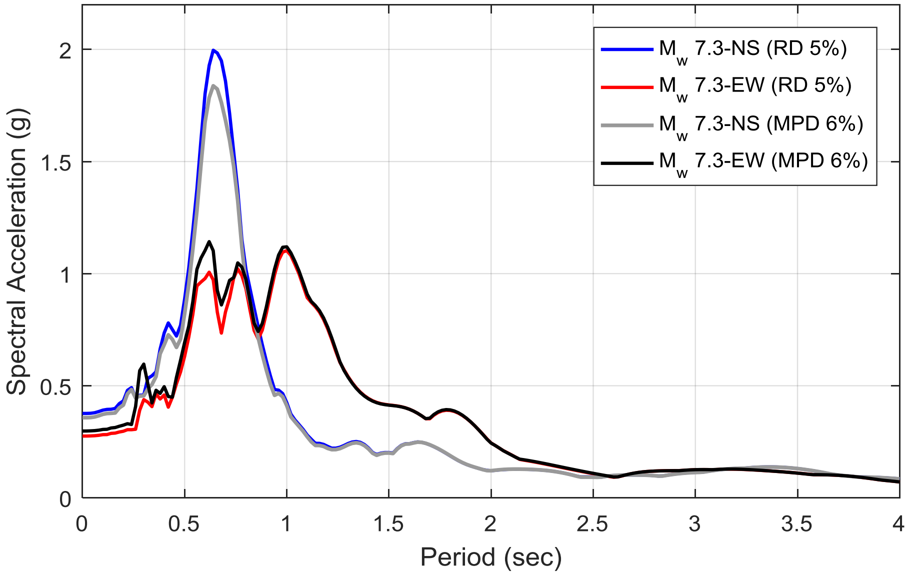

Figure 5.28: Elastic 5% Damped Spectral acceleration example for the SW corner of the third floor (L3) for Nyatapola temple using two damping techniques: Rayleigh damping set as 5% for 1st and 3rd modes and MPD as set 6% for 1st mode.

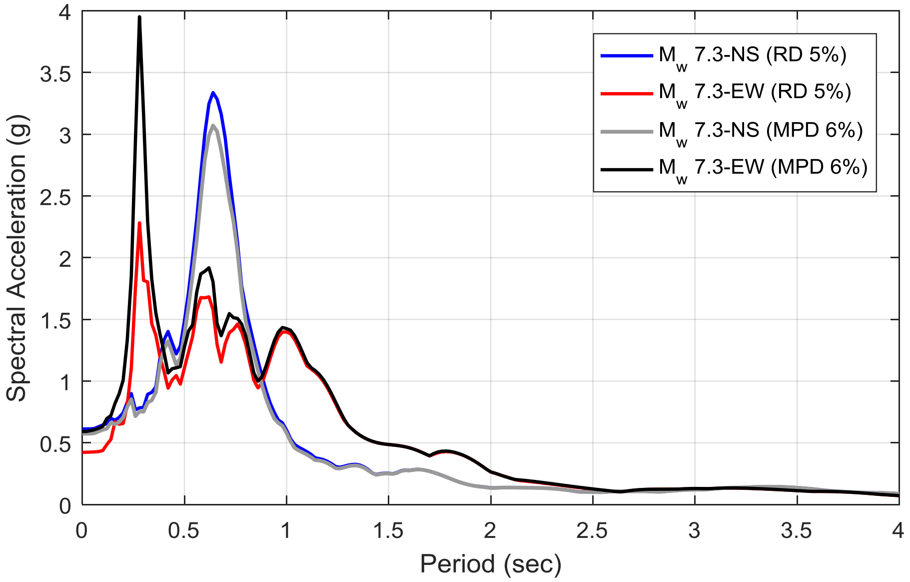

Figure 5.29: Elastic 5% Damped Spectral acceleration example for the SW corner of the fifth floor (L5) for Nyatapola temple using two damping techniques: Rayleigh damping set as 5% for 1st and 3rd modes and MPD as set 6% for 1st mode.

5.5 Summary

Linear time history analyses of the Nyatapola Temple are conducted systematically, where unscaled Gorkha ground motion records were applied to both the pre-earthquake (mainshock) and post-earthquake (aftershock) FE model. Acceleration time histories are applied in bidirectional pairs where Rayleigh damping was set at 5% damped of critical in the 1st and 3rd modes. Time histories results were summarized in terms of maximum floor displacement, maximum interstory drift, maximum floor acceleration, maximum uncorrelated acceleration amplification ratio, and torsional demand profiles. Additionally, the frequency response of the structures was quantified in terms of in-structure spectral acceleration spectra. Maximum values of these quantities are shown in Figure 5.30.

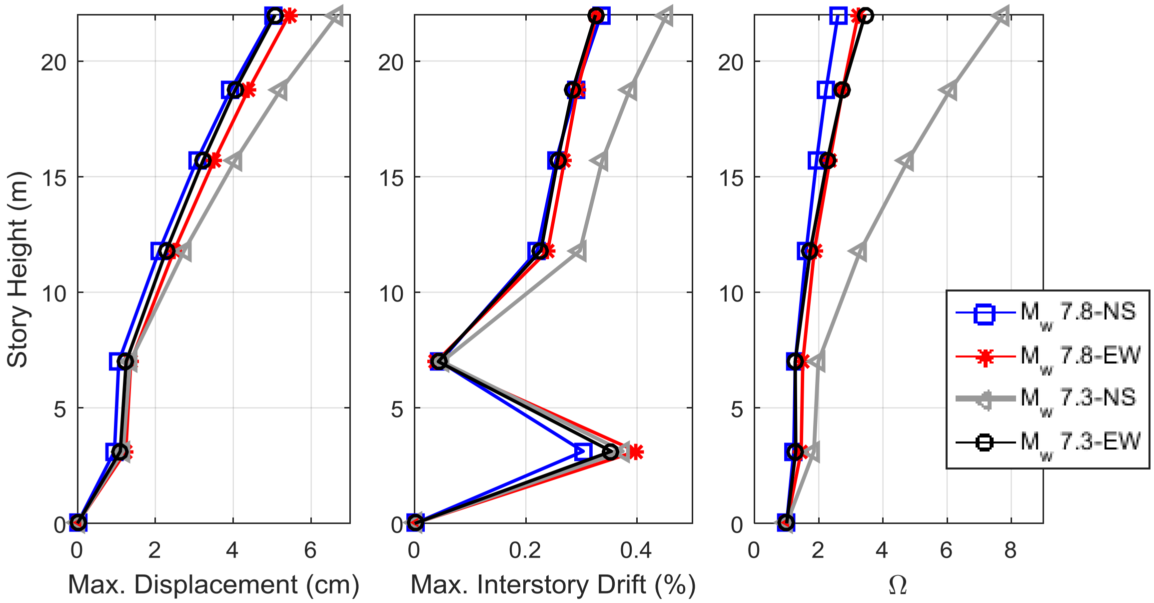

(a) (b) (c)

Figure 5.30: Maximum values for the linear time history response of Nyatapola under mainshock and aftershock Gorkha earthquakes: (a) maximum floor displacement, (b) maximum interstory drift, and (c) uncorrelated acceleration amplification ratio.

Key conclusions from this study include:

- The maximum displacement, maximum interstory drift, maximum absolute acceleration, and maximum uncorrelated acceleration amplification ratio occurred in the NS direction of the aftershock record represented by 6.7 cm, 0.45%, 0.6g, and 7.7, respectively.
- The mainshock (M_w 7.8) and aftershock (M_w 7.3) records caused the maximum displacement of temple in south-east and north-west directions, respectively.

- The distribution of maximum acceleration follows a linear trend (shear-like mode) for all records except the NS direction of the aftershock records which follows a parabolic trend (bending-like mode).
- Torsional drift demand was largest due to the aftershock event, with a maximum rotation of 0.15° at first floor, which is very similar to the permanent drift quantified within the point cloud data results.

CHAPTER 6: CONCLUSIONS AND RECOMMENDATIONS

6.1 Research Findings

The 2015 Gorkha Earthquake resulted in widespread damage to many districts and thousands of houses throughout Nepal. Given the construction style and building inventory of Nepal, numerous cultural heritage sites suffered irreplaceable damage as well as large economic losses to the Nepali economy. The Nyatapola temple was one of the few pagodas that remained standing, but experienced extensive cracks with widths up to 30 mm at the first-floor. To preserve the cultural heritage and minimize risk and losses of the structures, engineering knowledge was gathered on the response of Pagoda style temples for potential retrofit schemes, as aligned with the UNESCO mission UNESCO to reduce the losses caused by earthquakes to heritage sites around the world.

The key structural elements of pagoda temples include thick dual wythe masonry walls with mud mortar, multiple overhanging roof system, heavy timber members, and multi-tiered plinth foundation. The causes of the seismic vulnerability were due to the basic construction materials being unable to resist earthquake and lateral forces. The substantial level of damage observed is evident through cracking in the mud-mortar masonry walls, both in the mud mortar and masonry elements.

A 3D finite element (FE) linear model was used to capture the dynamic properties of the temple structure within a commercial FE packages, SAP2000 v19.1. The geometric dimensions of Nyatapola temple were guided by the lidar data within a 1% error tolerance to best represent the in-situ geometry. The various structural components were modeled as a combination of solid block elements for mud masonry walls and frame elements for the timber beams and columns. The load-bearing walls are considered as structural elements, while timber struts and roof systems are considered nonstructural elements. The timber roof system was simplified by using additive mass within single node elements (zero-dimension). The base over the plinth is considered rigid, neglecting any dynamic interaction. After linear-elastic material properties were selected based on the relevant literature, an eigenvalue analysis was performed to illustrate the model's dynamic properties. Pre- and post-earthquake FE models the Nyatapola temple showed precise calibration with ambient vibration data, where the percentage error for the fundamental frequency is less than 1%.

The results displayed a pre-earthquake fundamental frequency of 1.68 Hz is higher than other Nepali temples, indicating its unusual stiff behavior. When comparing the pre-earthquake state to the post-earthquake state, a frequency decrease of 11% was observed in the fundamental mode, indicating significant reduction of structural stiffness. This is a significant change in frequency, indicating the significant forces that occurred during the shaking of the mainshock and its aftershock sequence.

Linear time history analyses of the Nyatapola Temple were conducted systematically, resulting in maximum floor displacement, maximum interstory drift, maximum floor acceleration, maximum uncorrelated acceleration amplification ratio, and torsional demand profiles from applying unscaled Gorkha ground motion records (two orthogonal horizontal components) to both the pre-earthquake (mainshock) and post-earthquake (aftershock) FE model. The vertical motions were not considered, due to lack of available motions and this work focused on the acceleration-controlled out-of-plan (OOP) response while Nyatapola temple stayed upright. Acceleration time histories are applied in bidirectional pairs where Rayleigh damping was set at 5% damped of critical in the 1st and 3rd modes. The frequency response of the structures was quantified in terms of in-structure spectral acceleration. Key conclusions from this study are summarized by:

- The maximum displacement and absolute acceleration experienced by Nyatapola reached to 6.7 cm and 0.6 g respectively, at the upper floor of the temple under the aftershock (Mw 7.3) in the north-south direction.
- The distribution of maximum floor displacement increases with height, which does not follow a linear trend, but rather is linear at the lower floors (shear-like mode) and parabolic (bending-like mode) at the upper floors.
- The distribution of maximum acceleration follows a linear trend (shear-like mode) for all records except the NS direction of the aftershock records which follows a parabolic trend (bending-like mode).
- Linear time history responses were observed to be more severe for aftershocks than mainshock due to Gorkha earthquake.
- Matching the residual drift in the point cloud data, the aftershock torsional drift demand was the largest with a maximum rotation of 0.15° at first floor.
- Typical construction and architecture of Pagoda style temples influence their dynamic behavior, leading to increased seismic vulnerability. Better torsional retrofitting measures may reduce damage on these heritage structures.

Although this thesis has examined post-damage dynamic characteristics and behavior of the historical URM Nyatapola temple, as with any study, this research is not without limitations. Restrictions of this study can be summarized with three major points:

- Structural configuration: Unavailable sufficient architectural design due to long-term construction. In addition, not all of the required measurements were able to be extracted from due to occlusion in the point cloud.
- Model discretization: Inability of the FE model to represent the complex behavior of the earthen URM structure, particularly at larger displacements.
- Ground-motion components: The vertical motions were not considered in this study. Vertical ground motions may not be negligible for out-of-plane loads on the earthen URM walls.

6.2 Recommendations for Future Work

Recommendations for future work in this area include:

- Perform nonlinear time history analysis for material nonlinearities in the system in order to acquire more representative results.
- Apply vertical ground motion to a similar model, which may increase the seismic demands observed in the analytical results.
- Extend the study for other Pagoda style temples in the region to understand and identify general trends to reduce the seismic vulnerability to other cultural heritage sites.

REFERENCES

Aras, F., Krstevska, L., Altay, G., and Tashkov, L. (2011). “Experimental and numerical modal analyses of a historical masonry palace.” Construction and Building Materials, 25(1), 81-91.

Atamturktur, S., Prabhu, S., and Roche, G. (2014). "Predictive modeling of large scale historic masonry monuments: uncertainty quantification and model validation." Proc., 9th International Conference on Structural Dynamics, EURODYN 2014, Porto, Portugal.

Beckh, M. (2006). “Traditional construction techniques of the Newars at the Itum Baha monastry in Kathmandu.” Paper presented at the Second International Congress on Construction History, Exeter.

Boeraeve, P. (2010). Introduction to the Finite Element Method (FEM). Institut Gramme: Liege, Belgium, 2-68.

Bonapace, C., and Sestini, V. (2003). Traditional materials and construction technologies used in the Kathmandu valley. United Nations Educational, Scientific and Cultural Organization, 7 Place de Fontenoy, 75352 Paris 07 SP, France.

Brando, G., Rapone, D., Spacone, E., Barbosa, A., Olsen, M., Gillins, D., Soti, R., Varum, H., Arêde, A., Vila-Pouca. N, Furtado, A., Oliveira, J., Rodrigues, H., Stavridis, A., Bose, S., Faggella, M., Gigliotti, R., and Wood, R. L. (2015). "Reconnaissance report on the 2015 Gorkha earthquake effects in Nepal." Proceedings, XVI Congegno ANIDIS, At L'Aquila, Italy.

Chandra, N. (2016). "A UNESCO WORLD HERITAGE SITE in NEPAL." <https://www.linkedin.com/pulse/nyatapola-temple-nepal-traveltour-chandra-niraula->.

Chaulagain, H., Gautam, D., and Rodrigues, H. (2018). "Revisiting major historical earthquakes in Nepal: Overview of 1833, 1934, 1980, 1988, 2011, and 2015 Seismic Events." Elsevier, 1–17.

Dhital, M. R. (2015). Geology of the Nepal Himalaya: regional perspective of the classic collided Orogen. Springer International Publishing Switzerland.

Faculty of Science (2015). "The recent Nepal earthquakes – Big, but not unexpected." University of Helsinki, Finland.<http://www.helsinki.fi/facultyofscience/research/news/2015/nepalearthquakes.html> (Nov. 5, 2017).

Faro (2014): Faro laser scanner Focus^{3D} X 130: features, benefits and technical specifications. FARO Technologies, Lake Mary, FL, USA.

Feng, G., Li, Z., Shan, X., Zhang, L., Zhang, G., and Zhu, J. (2015). "Geodetic model of the 2015 April 25 Mw 7.8 Gorkha Nepal earthquake and Mw 7.3 aftershock estimated from InSAR and GPS data." Geophysical journal international (GJI), 203(2), 896-900.

Galetzka, J., Melgar, D., Genrich, J. F., Geng, J., Owen, S., Lindsey, E. O., and Upreti, B. N. (2015). "Slip pulse and resonance of the Kathmandu basin during the 2015 Gorkha earthquake, Nepal." Science, 349(6252), 1091-1095.

"Geoservices Maritime Pvt Ltd." (2013). <http://www.geoservicesmaritime.com/lidar-engineering-.html> (May 5, 2017).

Jaishi, B., Ren W., Zong, Z., and Maskey, P. N. (2003). "Dynamic and seismic performance of old multi-tiered temples in Nepal." Eng. Struct. 25 (14), 1827-1839.

Kanel, K. R., and Dahal, G. R. (2008). “Community forestry policy and its economic implications: an experience from Nepal.” International Journal of Social Forestry, 1(1), 50-60, ISSN 1979-2611.

Kodikara, K. A. T. L., Chan, T. H.T., Nguyen, T., and Thambiratnam, D. P. (2016). "Model updating of real structures with ambient vibration data." Journal of Civil Structural Health Monitoring, 6(3), 329–341.

Lei, X., Si-Qing, Q., Bai-Cun, Y., Xiao-Wa, W., Ke, Z., and Hong-Ran, C. (2017). "Earthquake tendency of the Himalayan seismic belt". arXiv:1708.07262.

Lourenco, P. B. (2002). "Computations on historic masonry structures." Progress in Structural Engineering and Materials, 4(3), 301-319.

Marjanishvili, S. M. (2004). “Progressive analysis procedure for progressive collapse.” Journal of Performance of Constructed Facilities, 18(2), 79-85.

Medecins Sans Frontiers. (2015). “Nepal.” <http://www.msf.org/en/where-we-work/Nepal>.

Menon, A., Shukla, S., Samson, S., Aravaind, N., Romão, V., and Paupério, E. (2017). "Field observations on the performance of heritage structures in the Nepal 2015 earthquake." 16th World Conference on Earthquake Engineering, (16WCEE 2017), Santiago Chile, N° 2465.

MoHA and DPNet (2009). Nepal Disaster Report 2009: The hazardscape and vulnerability, ministry of home affairs and Nepal disaster preparedness network-Nepal. Jagadamba Press, Kathmandu, Nepal ISBN: 9937-2-1301-1.

Nepal Current News (2015). “Earthquake Ruin Nepal.” <http://nepalcurrentnews.blogspot.com/> (Sept. 1, 2017).

Nepal Disaster Risk Reduction Portal (2016). Final situation report of earthquake 2015. <http://drrportal.gov.np/> (May 20, 2017).

Nienhuys, S. (2003). “Options for reconstruction and retrofitting of historic Pagoda temples.” reconstruction of temples in Kathmandu, HUYS ADVIES.

Oliveira, C. S., Çaktı, E., Stengel, D., & Branco, M. (2012). "Minaret behavior under earthquake loading: the case of historical Istanbul." Earthquake Engineering and Structural Dynamics, 41(1), 19-39.

Parajuli, R. H., Kiyono, J., Taniguchi, H., Toki, K., and Furukawa, A., (2010). “Parametric study and dynamic analysis of a historical masonry building of Kathmandu.” Disaster Mitigation of Cultural Heritage and Historic Cities, 4, 149-156.

Pastor, M., Binda, M., and Harčarik, T. (2012). "Modal assurance criterion." Procedia Engineering, 48, 543-548.

Paudyal, H. and Panthi, A. (2010). “Seismic vulnerability in the Himalayan region.” Himalayan Physics, 1(1), 14-17.

Paudyal, Y. R., Yatabe, R., Bhandary, N. P., & Dahal, R. K. (2013). "Basement topography of the Kathmandu Basin using microtremor observation." Journal of Asian Earth Sciences, 62, 627-637.

Peeters, B., Van den Branden, B., Laquiere, A., and De Roeck, G. (2000). "Output-only modal analysis: development of a GUI for Matlab." Shock and Vibration Digest, 32(1), 60.

Rai, D. C., Singhal, V., Raj, S. B., and Sagar, S.L. (2016). “Reconnaissance of the effects of the M7. 8 Gorkha (Nepal) earthquake of April 25, 2015.” Geomatics, Natural Hazards and Risk, 7(1), 1-17.

Rajaure, S., Asimaki, D., Thompson, E.M., Hough, S., Martin, S., Ampuero, J. P., Dhital, M. R., Inbal, A., Takai, N., Shigefuji, M., Bijukchhen, S., Ichiyanagi, M., Sasatani, T., and Paudel, L. (2017). "Characterizing the Kathmandu Valley sediment response through strong motion recordings of the 2015 Gorkha earthquake sequence." Tectonophysics, 714–715, 146-157.

Riegl (2014): Riegl VZ-400 datasheet, Riegl Laser Measuring Systems GmbH, Austria.

SAP2000, V19.1. Computers and Structures, Inc. [US]. <https://www.csiamerica.com/>.

Shakya, M., Varum, H., Vicente, R., and Costa, A. (2012). "Structural vulnerability of Nepalese Pagoda temples." 15th World Conference on Earthquake Engineering, Lisbon, Portugal, 1–10.

Shakya, M., Varum, H., Vicente, R., and Costa, A. (2014). “Seismic sensitivity analysis of the common structural components of Nepalese Pagoda temples.” Bull Earthquake Eng. 12(4), 1679-1703.

Song, M., Yousefianmoghadam, S., Mohammadi, M. E., Moaveni, B., Stavridis, A., and Wood, R. L. (2017). "An application of finite element model updating for damage assessment of a two-story reinforced concrete building and comparison with lidar." Structural Health Monitoring, doi:10.1177/1475921717737970.

Takai, N., Shigefuji, M., Rajaure, S., Bijukchhen, S., Ichiyanagi, M., Dhital, M. R., and Sasatani, T. (2016). "Strong ground motion in the Kathmandu Valley during the 2015 Gorkha, Nepal, earthquake." Earth, Planets and Space, 68(1), 10.

Ventura, C. E., Brincker, R., Dascotte, E., and Andersen, P. (2001). "FEM updating of the heritage court building structure." Proc., International Modal Analysis Conference (IMAC-XIX), 2011, 1, 324-330.

Ventura, C. E., Lord, J. F., Turek, M., Brincker, R., Andersen, P., and Dascotte, E. (2005). "FEM updating of tall buildings using ambient vibration data." Proc., the sixth European conference on structural dynamics (EURODYN), 4-7.

Wang, K., and Fialko, Y. (2015). Slip model of the 2015 Mw 7.8 Gorkha (Nepal) earthquake from inversions of ALOS-2 and GPS data. Geophysical Research Letters, 42(18), 7452-7458.

Wood, R. L. and Hutchinson, T. C. (2012). "Effects of ground motion scaling on nonlinear higher mode building response." Earthquakes and Structures, 3(6), 869-887.

Wood, R. L., Mohammadi, M. E., Barbosa, A. R., Kawan, C. K., Shakya, M., and Olsen, M. J. (2017a). “Structural damage assessment of a five tiered Pagoda style temple in Nepal.” 16th World Conference on Earthquake Engineering, (16WCEE 2017), Santiago, Chile, N° 2915.

Wood, R. L., Mohammadi, M. E., Barbosa, A. R., Abdulrahman, L., Soti, R., Kawan, C. K., Shakya, M., and Olsen, M. J. (2017b)."Damage Assessment and Modeling of the Five-Tiered Pagoda-Style Nyatapola Temple." Earthquake Spectra.

Yu, H., Mohammed, M. A., Mohammadi, M. E., Moaveni, B., Barbosa, A. R., Stavridis, A., and Wood, R. L. (2017). "Structural identification of an 18-story RC building in Nepal using post-earthquake ambient vibration and lidar data." Frontiers in Built Environment, 3, 11.

Appendix A: Maximum Interstory Drift Distribution

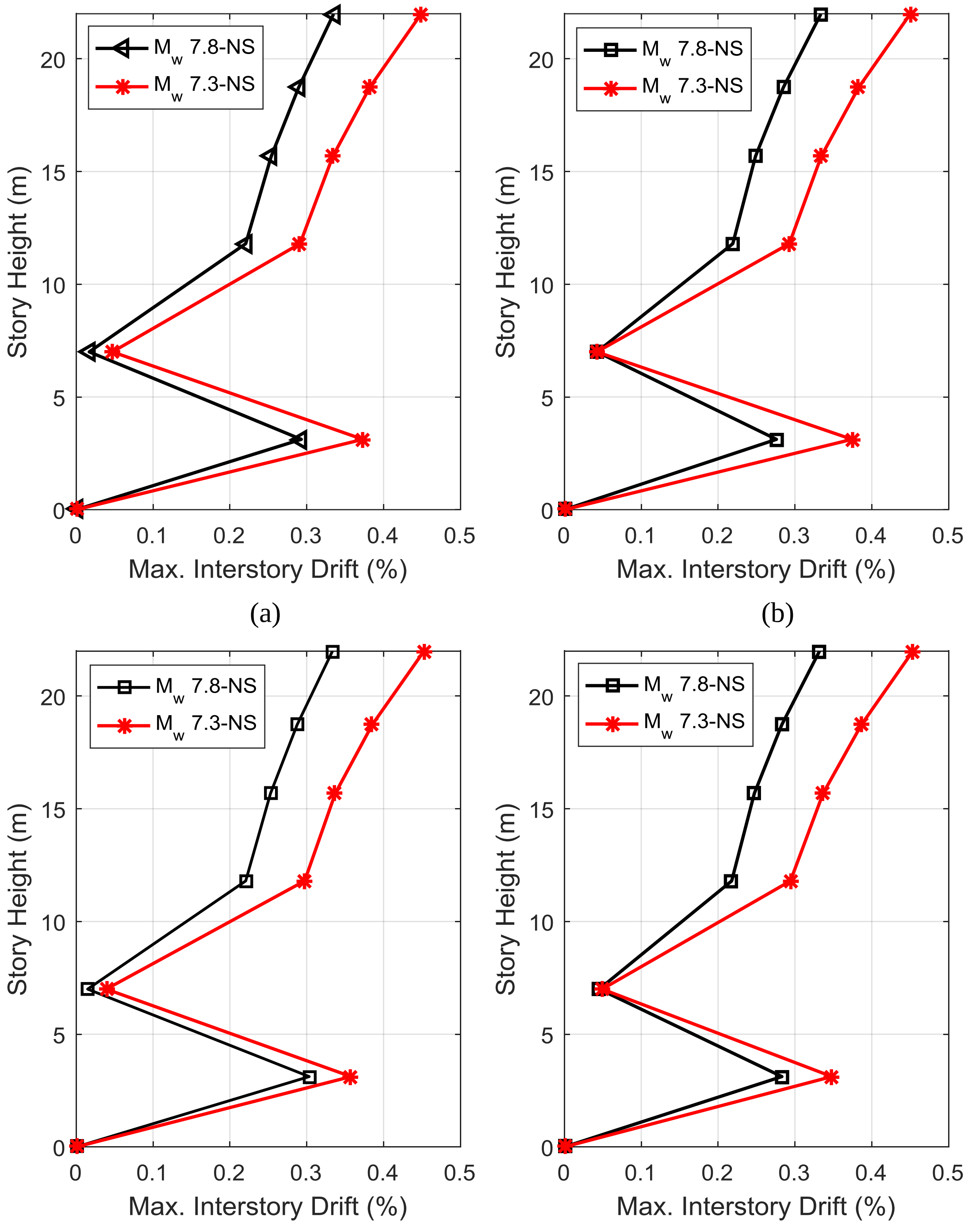

(a) (b)

(c) (d)

Figure A 1: Maximum interstory drift curves in (%) for the Nyatapola temple in the NS direction: (a) south-west corner, (b) north-west corner, (c) north-east corner, and (d) south-east corner.

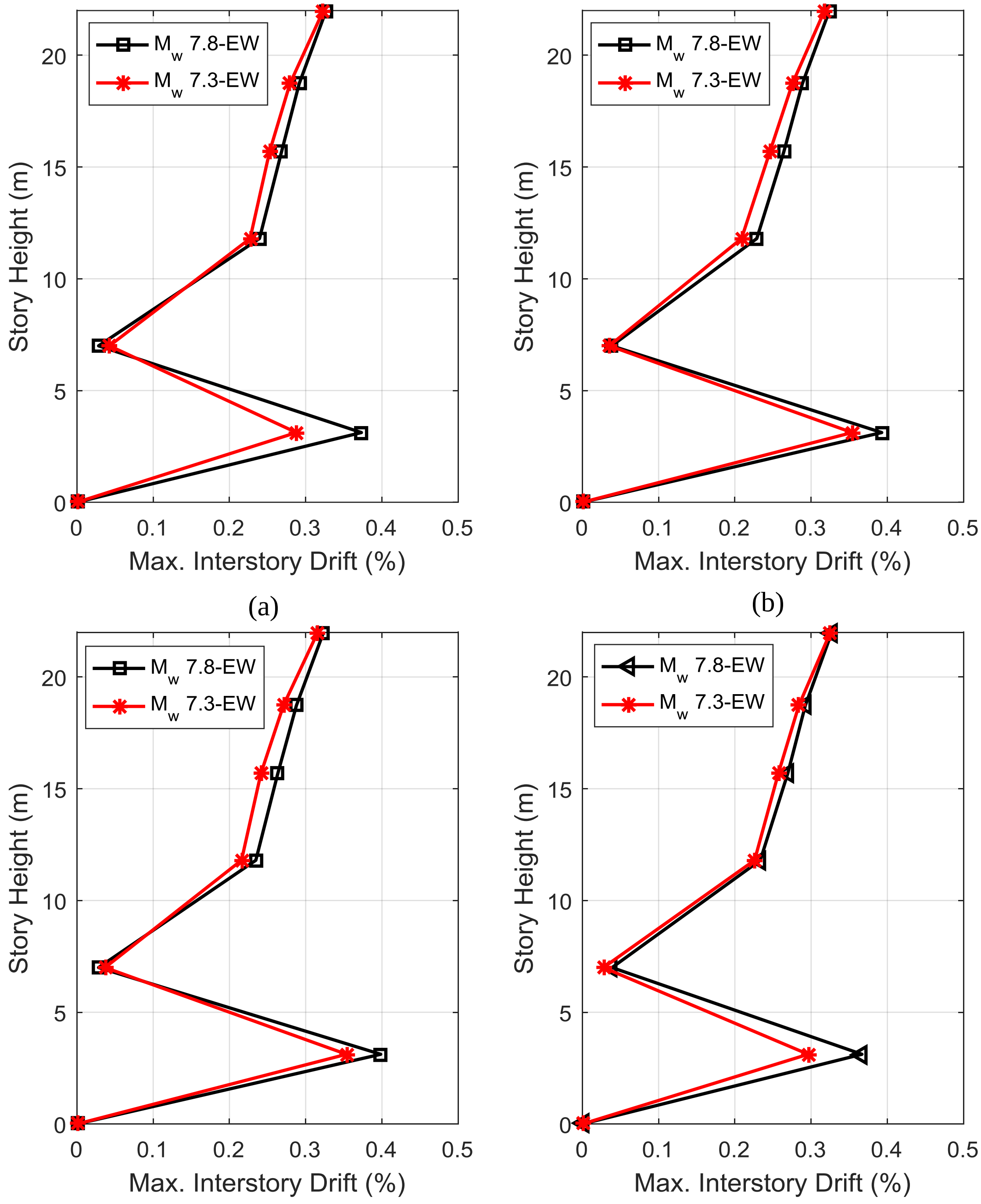

(a)

(b)

(c)

(d)

Figure A 2: Maximum interstory drift curves in (%) for the Nyatapola temple in the EW direction: (a) south-west corner, (b) north-west corner, (c) north-east corner, and (d) south-east corner.

Appendix B: Maximum Floor Acceleration Distribution

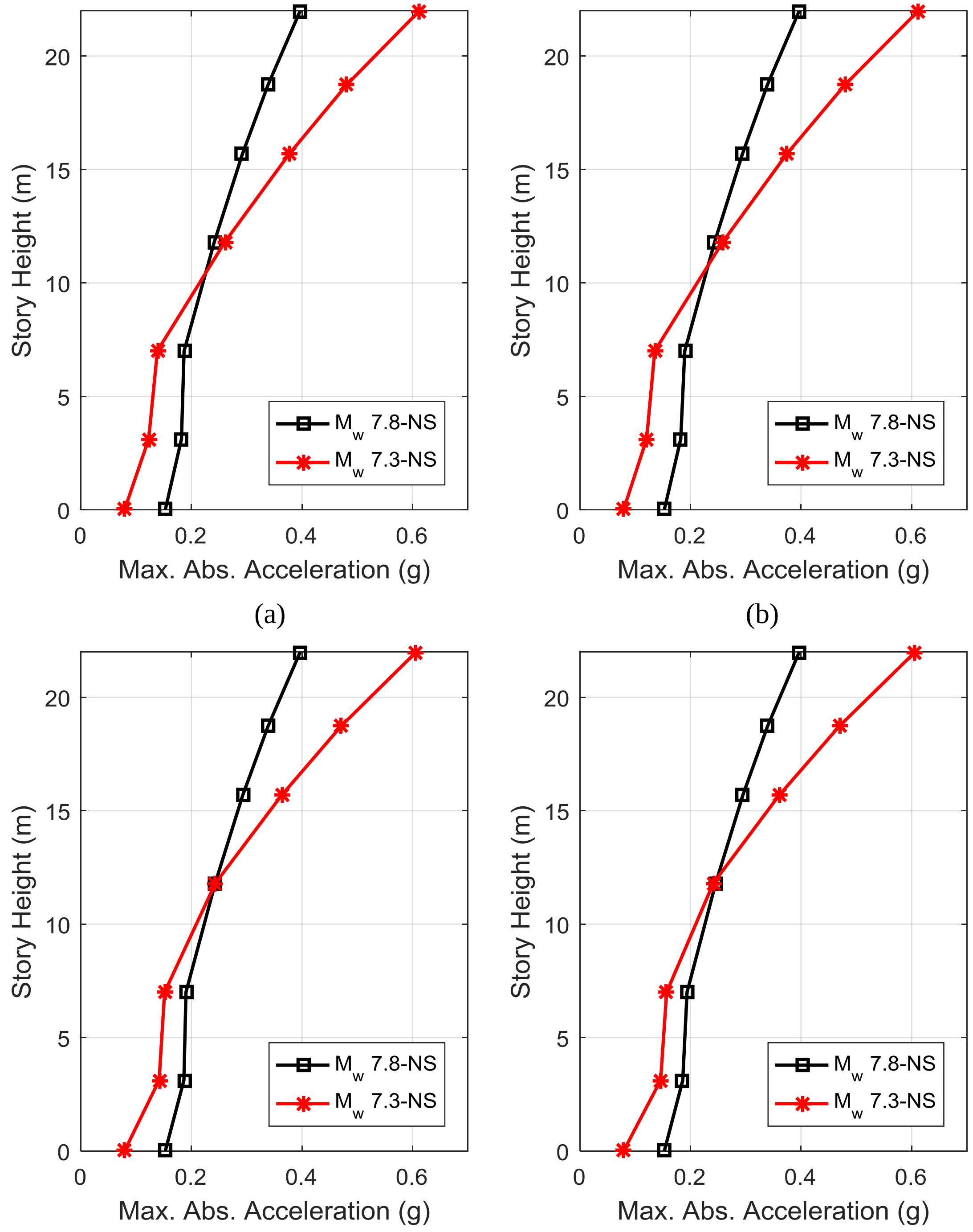

(a) (b)

(c) (d)

Figure B 1: Maximum absolute acceleration envelope curves for the Nyatapola temple in the NS direction: (a) south-west corner, (b) north-west corner, (c) north-east corner, and (d) south-east corner.

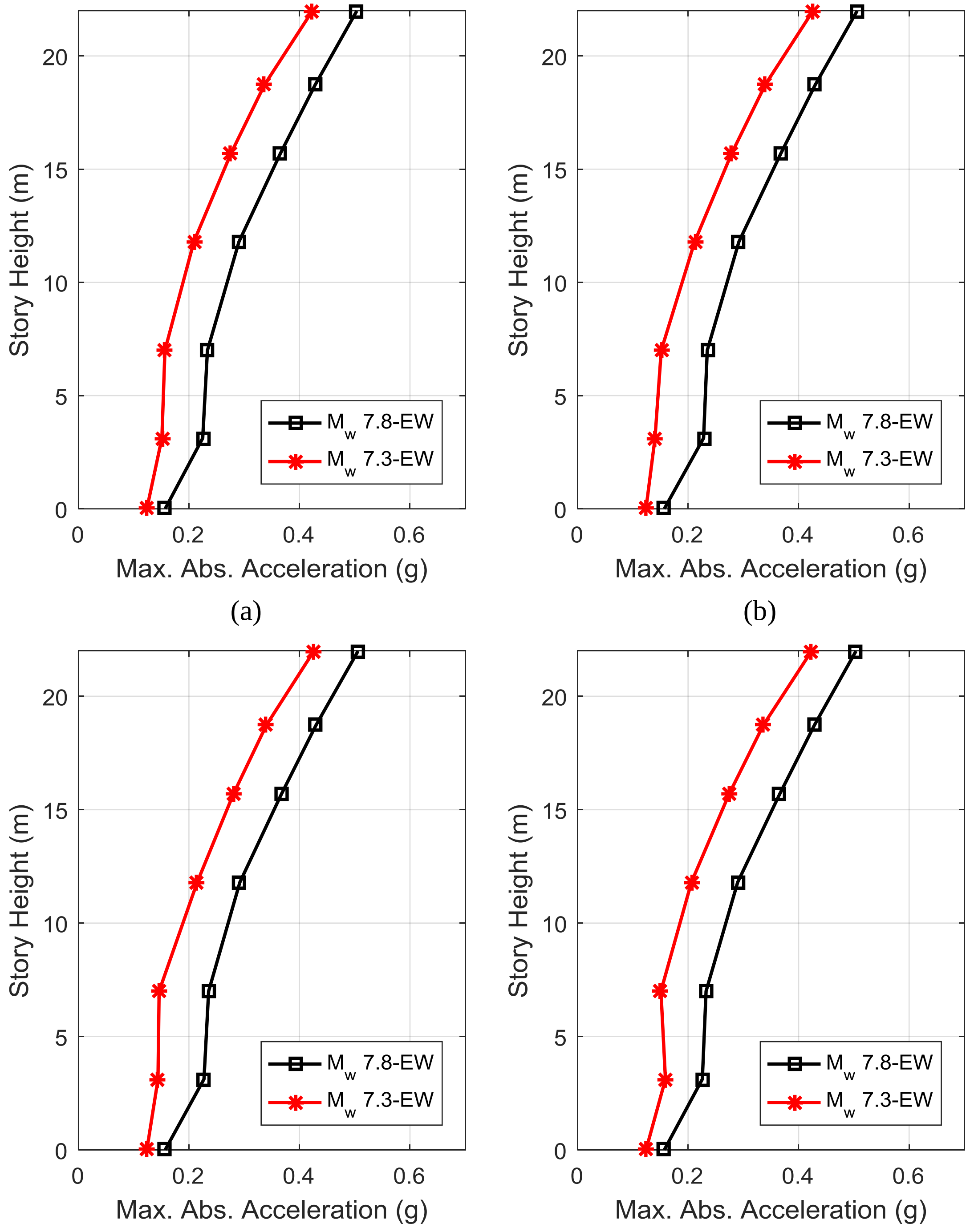

(a) (b)

(c) (d)

Figure B 2: Maximum absolute acceleration envelope curves for the Nyatapola temple in the EW direction: (a) south-west corner, (b) north-west corner, (c) north-east corner, and (d) south-east corner.

Appendix C: Uncorrelated Acceleration Amplification Ratio

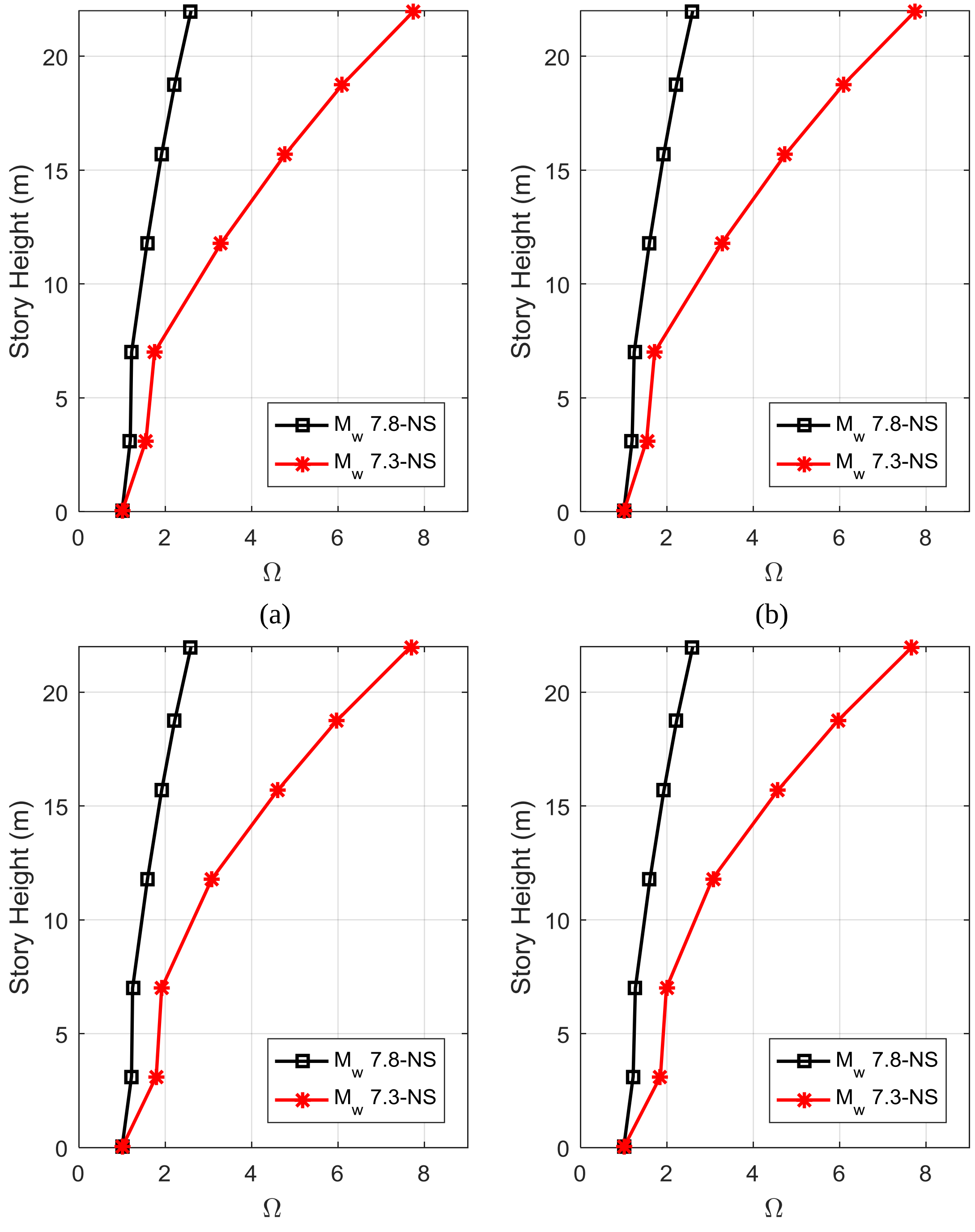

(a) (b) (c) (d)

Figure C 1: Uncorrelated acceleration amplification ratio, Ω, for the Nyatapola temple in the NS direction: (a) south-west corner, (b) north-west corner, (c) north-east corner, and (d) south-east corner.

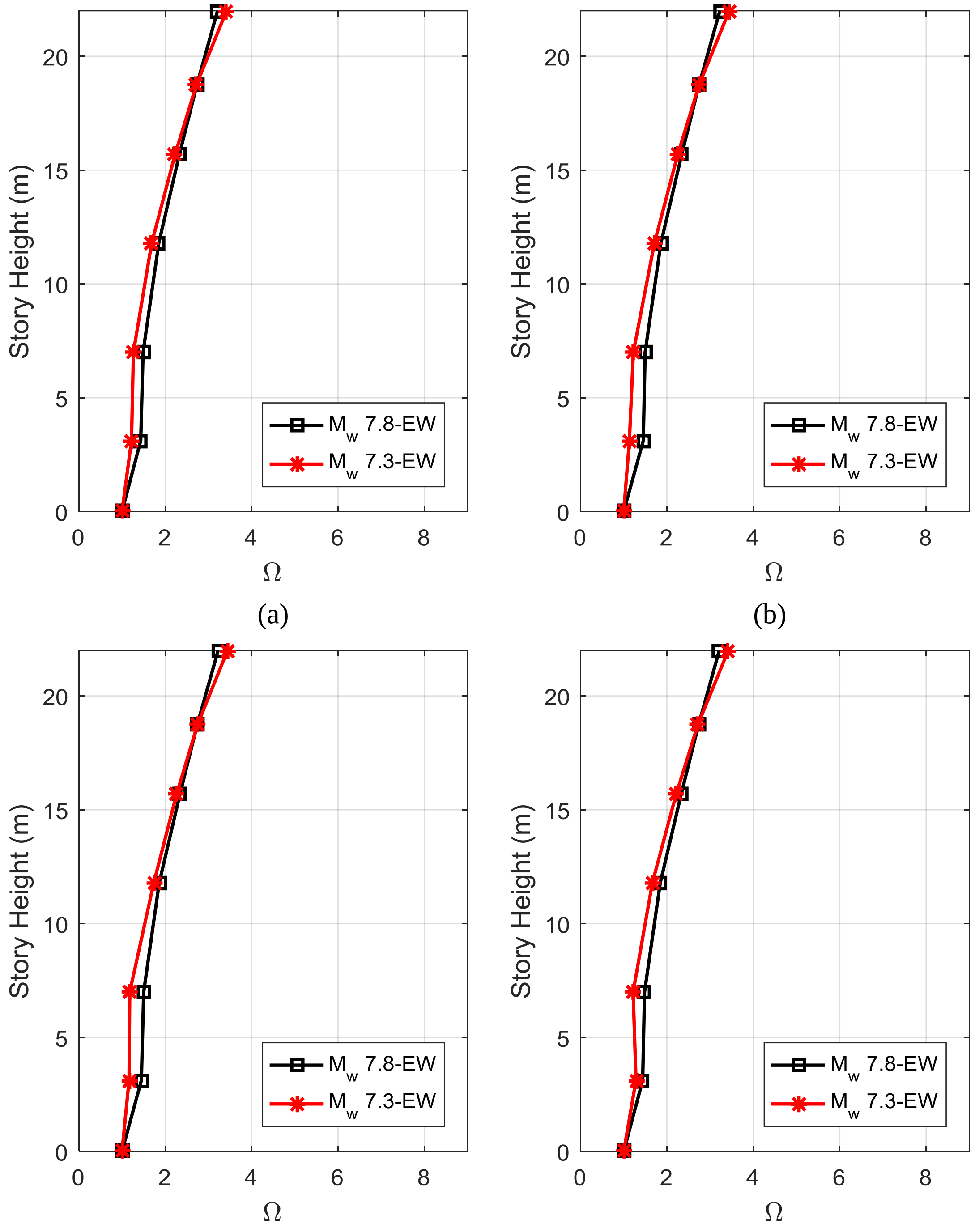

(a) (b) (c) (d)

Figure C 2: Uncorrelated acceleration amplification ratio, Ω, for the Nyatapola temple in the EW direction: (a) south-west corner, (b) north-west corner, (c) north-east corner, and (d) south-east corner.